Measurements of azimuthal correlation between jets and charged particles at LHC-ALICE experiment

Dousatsu SAKATA

February 2013

Measurements of azimuthal correlation between jets and charged particles at LHC-ALICE experiment

Dousatsu SAKATA
Doctoral Program in Physics

Submitted to the Graduate School of
Pure and Applied Sciences
in Partial Fulfillment of the Requirements
for the Degree of Doctor of Philosophy in
Science

at the
University of Tsukuba

Abstract

In the nature around us, quarks and gluons are confined in hadrons due to "confinement of quarks". However, the coupling strength of the QCD between quarks and gluons is to be asymptotically weaker with the increasing their energy. At high temperature the quarks and gluons move freely beyond the boundary of hadrons. Such high energy state is called Quark-Gluon Plasma(QGP). To create such state on the earth, the ultra relativistic heavy ion collision is unique tool.

It has been observed several signatures of the QGP formation at the Relativistic Heavy Ion Collider(RHIC). Suppression of high momentum particles is one of the signatures. High momentum particles are known to be produced in characteristic phenomena, jet , where high momentum particle are produced in cluster. The jet is produced when parton in each projectile is scattered with large momentum, followed by fragmentation into many hadrons.

It is considered that the cause of the suppression of high momentum particle is due to the characteristic energy loss of the parton in the QGP. On the other hands, many low momentum particles are formed at characteristic energy loss and the additional instead large angles from original low momentum particles is often called modification of jet. In theoretical approach, the energy loss and the shape modification of the jet is strongly relate to properties of hot/dense matter particularly gluon density and initial temperature of the QGP. Therefore study of jet modification is a good tool to investigate the properties of the QGP. Experimentally it is very important to measure the energy loss together with the energy re-distribution at large angles.

At the RHIC, it is difficult to collect enough data because of its low rate. The production cross-section of jet is strongly related to the collision energy. The Large Hadron Collider(LHC) starts nuclear-nuclear collisions with highest energy from 2010. LHC provides good opportunity to study the jet physics in heavy ion collisions to investigate parton interaction between jets and the QGP with higher statistics. Former study of the jet physics in heavy ion collisions has been done at the LHC by CMS. They have suggested the existence of re-distributed particles at large angles. In their study, the information of the spread angle is minimum and they can not see detail of jet modification.

In this paper, a new analysis method is proposed in order to see the modified energy(or momentum) with the spread angle. Proposed new method handles the momentum weighted azimuthal distribution of the associate particles with respect to the leading jet and direct comparison of pp and Pb-Pb collisions have been done. In this thesis, the centrality dependence and the leading jet momentum dependence are shown to extract jet modification effects, which shed light on the knowledge of the pass length dependence of jet modification.

We observe that the low momentum particles are re-distributed at large angles in the away-side of the jet with respect to the leading jet. This feature is consistent with CMS results. Furthermore we see the re-distributed momentum in the near-side. The missing momentum and the re-distributed momentum is found to be almost balanced. We see jet modification is larger with the highest jet momentum, and the effect is also larger in the central compared with peripheral collisions.

This is the spelling corrected edition of the original thesis.

Contents

List of Tables

List of Figures

Acknowledgment

Chapter 1

Introduction

According to prediction by the calculation of lattice QCD(Quark ChromoDynamics), phase transition of hadron to parton deconfinment occur at high temperature and/or density. Such high energy state of deconfined matter is called Quark-Gluon Plasma(QGP).

Research on relativistic and ultra-relativistic nuclear collision has started in early 70's at Bevatron/Bevalac. Then many experiments were carried out to research nuclear equation of states and fundamental theories of the strong interaction until now. Especially, Relativistic Heavy Ion Collider(RHIC) confirmed that the QCD phase transition exists, however, the equation of state still remains unknown.

On the other hand, in ultra relativistic nucleon collisions, scattered parton generated in initial parton-parton collision fragments to a large number of particles maintaining their direction. The particle clusters generated by scattered parton are called jet. Such jet process exist in relativistic nucleon-nucleon collisions and a number of experiments at RHIC got results to indicate that partons passing hot and dense QCD matter are reduced its energy. For example, the yield of high-momentum particles is significantly reduced in central collisions compared to peripheral ones. It is considered that this effect (called jet modification or jet quenching) is strongly related to QGP properties - temperature, gluon density and so on. So jets in high energy nucleon collisions can be probed to investigate hot/dense QCD matter. And jets are useful to validate QCD theory.

However at RHIC energy it is difficult to evaluate under limited jets statistics and separate particles coming from jets from particles from the other because jets are buried in a huge number of particles which are generated from thermal bulk.

At Large Hadron Collider(LHC), it was started nuclear colliding experiments with the highest energy in the world from 2010. In collisions at LHC energy huge number of particles are generated from jets via fragmentation (Fig.1.9). Thereby it can be reconstructed a large number of jets in nuclear collisions. We starts jet measurements to investigate jet modification with huge background in nuclear collisions.

In this chapter, we present theoretical background in jet physics in nuclear collisions and recent results for jet modification as introduction to understand physics motivation of this thesis. In latter chapter, we will describe in detail the experimental setup(chapter 2) and the physics framework used within the thesis(chapter 3) just after introduction.

The main topics of the thesis will be described in chapter 4, we compared momentum distri-

bution of associate particles with respect to trigger jet axis in Pb−Pb collisions with pp collisions to draw out information of particle re-distribution effects due to jet modification in QGP matter.

1.1 Quantum ChromoDynamics (QCD) [1]

The QCD describe fundamental force in strong interaction between quarks and gluons with three color symmetry SU(3). Quarks can carry electric charge and isolated color charge(red, blue and green). Gluons carry the strong force as gauge boson. QCD is a theory of a non-abelian gauge theory, then the theory permit gluons to interact by themselves.

1.1.1 Coupling Constant of Strong Force

The classical Lagrangian density for a quark with mass m given by

$$\mathcal{L}_{cl} = \sum_f^{N_f} \bar{q}_f(i\gamma^\mu D_\mu - m_f)q_f - \frac{1}{4}F_{\mu\nu}^a F_a^{\mu\nu}. \tag{1.1}$$

The quark (gluon) field q_f belong to the SU(3) triplet (octet). Therefor, f runs 1 to 3, while a runs 1 to 8. The covariant derivative, D_μ is

$$D_\mu \equiv \partial_\mu + ig\frac{\lambda^a}{2}A_\mu^a, \tag{1.2}$$

where λ^a is the eight Gell-Mann matrices.The strength tensor of gluon field $F_{\mu\nu}^a$ is defended as

$$F_{\mu\nu}^a = \partial_\mu A_\nu^a - \partial_\nu A_\mu^a + gf_{abc}A_\mu^b A_\nu^c, \tag{1.3}$$

where A_ν^a is the gluon fields, and f_{abs} is the structure constants of the SU(3) group. g is defined using coupling constant α_s as,

$$g \equiv \sqrt{4\pi\alpha_s}. \tag{1.4}$$

β function can be calculated in perturbation theory if g is small enough. And the function can be expanded in series of g.

$$Q\frac{\partial g}{\partial Q} = \beta, \beta(g) = -\beta_0 g^3 - \beta_1^5 + \cdots, \tag{1.5}$$

$$\beta_0 = \frac{1}{(4\pi)^2}(11 - \frac{2}{3}N_f), \beta_1 = \frac{1}{(4\pi)^4}(102 - \frac{38}{3}N_f), \tag{1.6}$$

Running coupling constant can be described as function of momentum transfer Q,

$$\alpha_s(Q) = \frac{1}{4\pi\beta_0 \ln(Q^2/\Lambda_{\text{QCD}}^2)}\left(1 - \frac{\beta_1}{\beta_0^2}\frac{\ln\left(\ln(Q^2/\Lambda_{\text{QCD}}^2)\right)}{\ln(Q^2/\Lambda_{\text{QCD}}^2)} + \cdots\right) \tag{1.7}$$

Λ_{QCD} is called QCD scale parameter, to be determined from experiments.

1.1.2 Asymptotic Freedom and Confinement of Quarks

According to Eq.1.7, coupling constant of strong force α_s should be smaller at large momentum transfer Q (or smaller distance). This property in large momentum transfer region is called "asymptotic freedom". The effect decreasing coupling constant with the increasing energy comes from anti-screening of color charge. It can be to calculate in perturbative calculations by DGLAP[3][4][5] of cross sections in deep inelastic processes.

As shown in Fig.1.1, measured coupling constants are in good agreement with the calculations by perturbative QCD. On the other hands, in smaller Q region (or larger distance), α_s gets
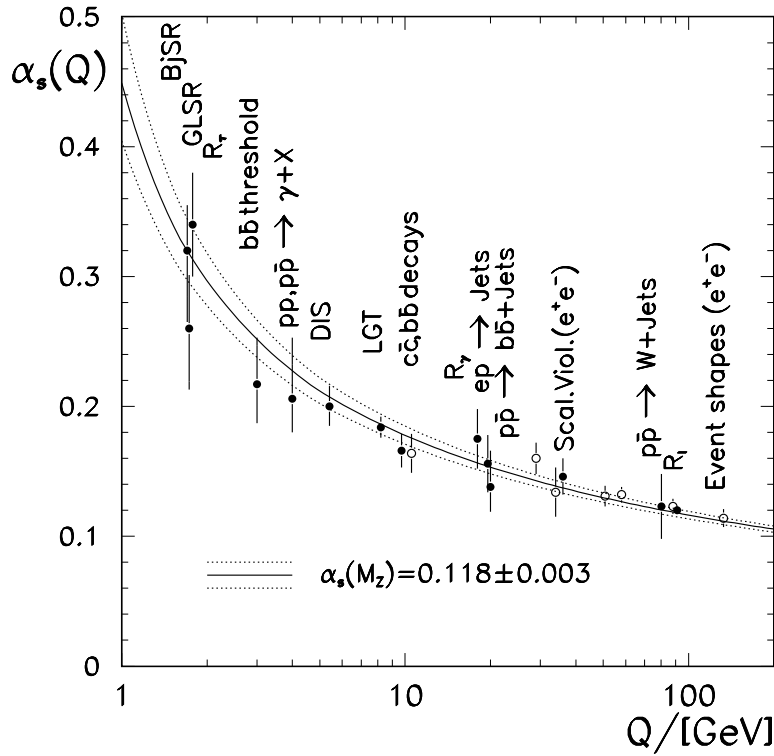
Figure 1.1: The running coupling constants as function of momentum transfers Q measured by various experiments and theoretical prediction by QCD [2]

increase rapidly.We call the property "confinement of quarks". Even if we try to draw quark away from hadron, strong force generate energy to produce a new $q\bar{q}$ pair from the vacuum. Therefor we can not let quark be alone in vacuum.

1.2 Quark Gluon Plasma (QGP)[6]

Let us think what will happen with the confined matter when constituents quarks of matter has small coupling constant at large Q-value as shown in Fig.1.1. To create such state, we can assume two methods, one is to heat up the matter, and the other is putting under the extremely

high density condition. I f we create high energy state using these methods, because of hadrons starts to overlap each other and, the quarks and gluons of hadron move beyond the boundary . This state is like "parton soup". We call the state Quark-Gluon Plasma(QGP).

The current knowledge of phase diagram is shown in Fig.1.2. In nature,matters are composed by proton and neutron at nominal temperature and baryon density. However if we apply heat and/or pressure matters turn into QGP state. Experimentally(see next section), we can create hot QGP with high energy collisions, and dense QGP with lower energy collisions.
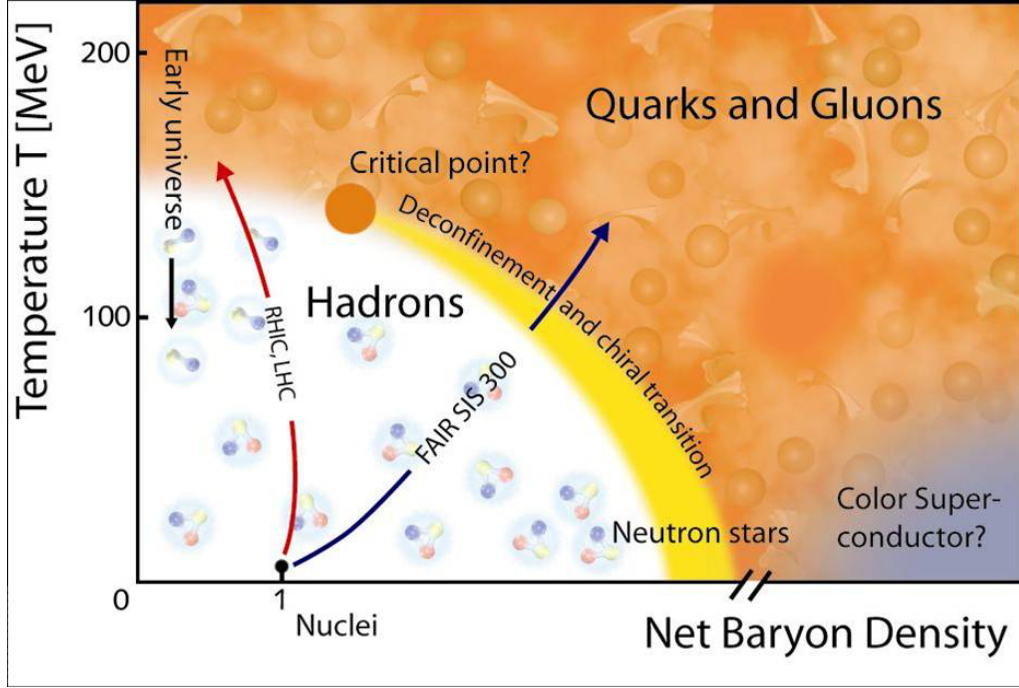
Figure 1.2: The phase diagram of QCD matter as function of temperature T and net baryon density

The energy density ϵ of an equilibrated ideal gas is given by Eq.1.8 as function of number degree of freedom n_{dof} and temperature T.$n_{\mathrm{dof}} = 16$ when the state has only gluon, 37 the state is with two flavors and 47.5 with three flavors,

$$\epsilon = n_{\mathrm{dof}} \frac{\pi^2}{30} T^4. \tag{1.8}$$

Fig.1.3 shows energy density divided by T^4 as function of temperature calculated by Lattice QCD at non-zero chemical potential and the resonance gas model.According to current calculation the energy density increase rapidly at critical temperature $T_c \sim 175 \mathrm{MeV}$.

1.3 High Energy Nuclear Collision

As seen in the previous section, to generate deconfined matter so called quark-gluon plasma, we need to produce high temperature or high density in the collision. As of now, relativistic heavy ion collisions are unique tool to creates such high energy states. The high energy heavy ion
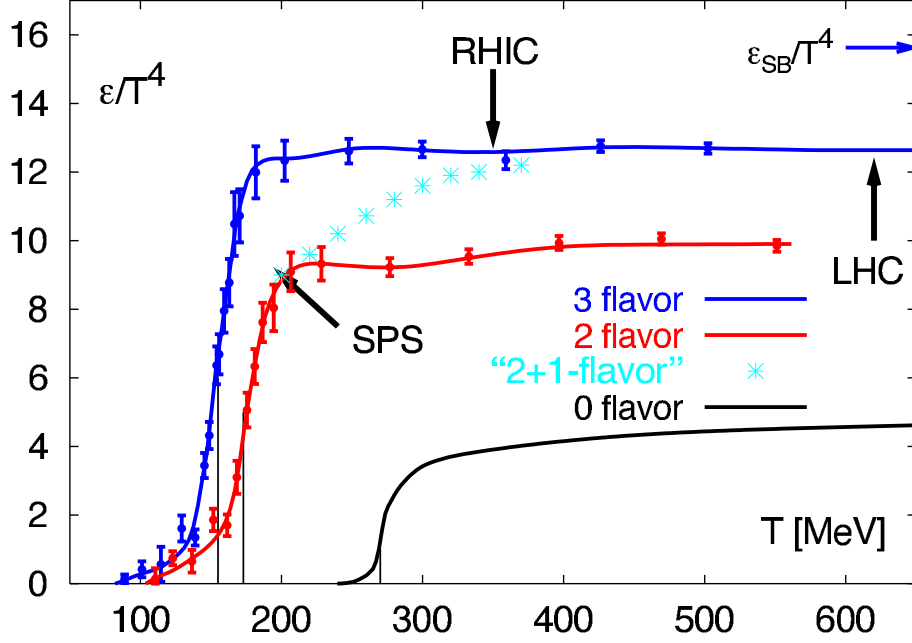
Figure 1.3: The normalized energy density as function of temperature T at $\mu_B = 0$ for each flavor estimation[7].The arrows on right side indicate the value ϵ/T^4Stefan-Boltzmann limit

collisions can create high energy in so small volume by bombarding nucleons over a short time experimentally. In this chapter, it is described about picture of QGP which is created by heavy ion collisions, in particular collision geometry, time evolution and particle production.

Table 1.1: Expected QGP Properties in Heavy Ion Collision

	SPS	RHIC	LHC
Nucleus	Pb+Pb	Au+Au	Pb+Pb
$\sqrt{s_{NN}}(GeV/c)$	17.4	200	5500
$dN_{ch}/d\eta$	500	850	$1500 - 4000$
τ_{QGP}^0 (fm/c)	1	0.2	0.1
T/T$_c$	1.1	1.9	3-4
$\varepsilon(GeV/fm^3)$	3	5	15-60
τ_{QGP} (fm/c)	< 2	2-4	> 10
τ_f (fm/c)	~ 10	$20 - 30$	$30 - 40$
V$_f$(fm^3)	$\sim 10^3$	$\sim 10^4$	$\sim 10^5$

The expected QGP parameters created in heavy ion collision is shown in Table.1.1. We observed QGP signals previous researches. First evidence of new state of matter was observed at Super Proton Synchrotron(SPS) using fixed target since 1980's. Several hadronic observable

shows strong non-linearity dependence with respect to the number of nucleons which participate in collisions. At RHIC, it was used collider instead of beam with fixed target. Then many kind of signals were observed which indicate existence of phase transition in quark matter. However the equation of state still remains unknown. To access property of matter need to perform at more high collision energy. The reason is some of observables were limited by statistics. Alternatively we could not have clear signal like as jet at RHIC energy. Since 2010,we started experiment with energy 10 times higher than RHIC energy. It can provide huge number of signals from QGP with long life time. Therefor it will allow significant qualitative improvement for measurements to draw out properties of QGP.

1.3.1 Collision Geometry
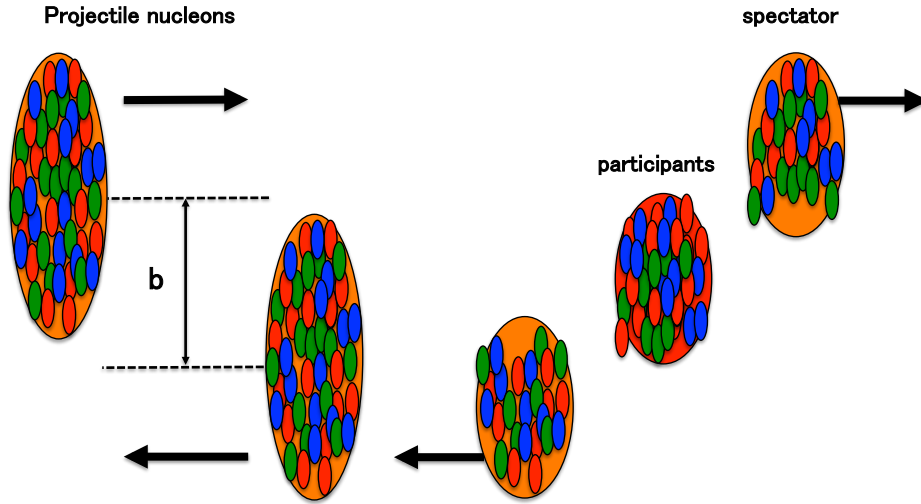
Figure 1.4: The over view of collision geometry in heavy ion collision

Collision geometry of nucleus-nucleus collision can be characterized by number of nucleons in projectile nucleus(A), collision energy at rest from($\sqrt{s}$) and distance between center of two nucleons impact parameter(b). Differential cross section with inelastic total cross section of nucleon σ_{NN}^{in} is described as following function

$$\frac{d^2\sigma_{AA}^{in}}{d^2b}(b,\sqrt{s_{NN}}) = 1 - (1 - \frac{1}{A^2}T_{AB}(b)\sigma_{NN}^{in}(\sqrt{s_{NN}}))^{A^2}, \tag{1.9}$$

In the case same nuclei collide each other, overlap function $T_{AB}(b)$ should be described as

$$T_{AB}(b) = \int ds^2 T_A(s)T_A(s-b) \tag{1.10}$$

where $T_A(s)$ is thickness of nuclei where are penetrated the other nuclei defended as function of nucleon density $\rho_A(r)$(normalized nucleon density ρ_{nm}) and radius in transverse plane s

$$T_A(s) = \int dz\rho_A(z,s), \rho_A(r) = \frac{\rho_{nm}}{1 + \exp((r - R_A)/a)} \tag{1.11}$$

In relativistic heavy ion collisions, the part of involved nucleons in collision are described by the participant spectator model. The nucleons brought into collisions are called participant and the other part in target and projectile nuclei are called spectator. The picture can be going to remain viable, heavy ion collision have all of assumption by the Glauber Model[8] which are listed following.

- these nucleons will carry sufficient momentum that they will be essentially undeflected as the nuclei pass through each other

- de Broglie wave length as long as nucleon size or less, then nuclei collision can be described as superposition of nucleon-nucleon collisions

- the nucleons move independently in the nucleus and that the size of the nucleus is large compared to the extent of the nucleon-nucleon force

In the Glauber model, we can calculate number of participant nucleons N_{part}, and number of nucleon-nucleon collisions N_{binary} as follows,

$$N_{\mathrm{part}}(b) = \int d^2 s T_A(s)(1 - \exp(-\sigma_{NN}^{in} T_A(s))$$

$$+ \int d^2 s T_A(s-b)(1 - \exp(-\sigma_{NN}^{in} T_A(s)), \qquad (1.12)$$

$$N_{\mathrm{binary}}(b) = \int d^2 s \sigma_{NN}^{in} T_A(s) T_B(s-b). \qquad (1.13)$$

1.3.2   Time Evolution

Fig.1.5 shows the history of the longitudinal evolution for the produced matter by an ultra relativistic heavy ion collision in the Bjorken picture.

Collision and Thermalize Stage $[0 < \tau < \tau_0]$

The process of huge entropy production in relativistic heavy ion collision can be described as two process. First model is mini-jet production as incoherent model. In central collision, partons are generated from semi-hard process. Such partons are difficult to separate with partons which generated from soft production. And they also interact with each other. the process could contribute to from an equilibrated parton plasma.

The other model is color string braking model as coherent model.A large number of strings and ropes between two projectile nuclear. Then many quark pairs and gluon pairs are generated in color electric field in participant region. In short time scale, equilibrated parton plasma are produced by partons in exited fields.

QCD Phase Transition and Hydrodynamical Evolution Stage $[\tau_0 < \tau < \tau_f]$

After the local thermal equilibrium is reached at τ_0, the system expand to longitudinal direction and transverse direction. Especially, we have seen experimental results which suggest transverse
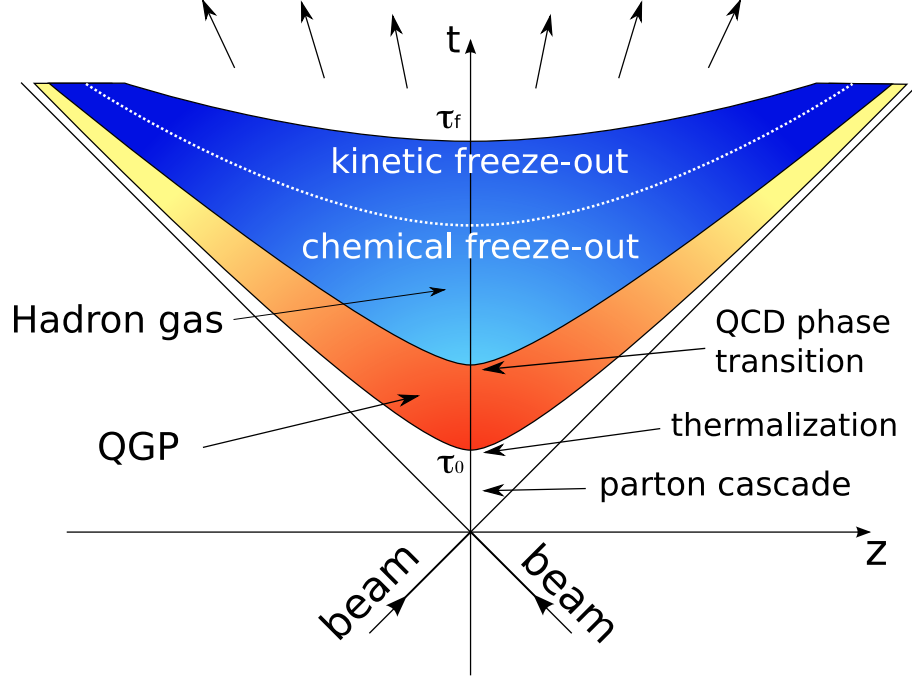
Figure 1.5: The overview of space-time evolution of heavy ion collision

expansion can be described as perfect fluid at RHIC. If the thermal matter expand on approximated hydrodynamics by a perfect fluid, the evolution picture can be parameterized by the local energy density ε and the local pressure P. The energy-momentum tensor and the baryon number current of the perfect fluid with fluid four velocity u^μ is given by

$$T^{\mu\nu} = (\varepsilon + P)u^\mu u^\nu - g^{\mu\nu}P \tag{1.14}$$

$$j_B^\mu = n_B u^\mu \tag{1.15}$$

Freeze out Stage $[\tau_f < \tau]$

After the transition QGP will be getting cold due to expansion of the system. Then the quark-gluon matter will be going to be hadron gas again on hyper-surface. We call the point chemical freeze out where the number of hadron species is frozen. Then created hadrons start colliding each other to thermalize. After the kinematics of hadrons are fixed, the point is called thermal freeze out.

1.4 Soft and Hard Particle Production

In relativistic heavy ion collisions,particle production can fall roughly into two categories, soft particle production and hard particle production.Experimentally, hard particles are detected as

particle cluster so called "jet". In this section, it will be given account of partons model which are introduced into collisions and particle production by collision.

1.4.1   Parton Distribution Function(PDF)

As has been well establish by the deep inelastic lepton-hadron collision scattering experiments,the nucleon is composed of valence quarks, sea quarks and gluons. As shown Fig.1.6, momentum fraction of wee partons(sea quarks and gluons) dominate with respect to the fraction of valence quark. However, number of gluons should be finite in finite space.And actually, number of gluons saturate when typical transverse size $1/Q$ eventually overlap each other.Such classical coherent field configuration by saturated gluons are called the color glass condensate(CGC)[9].
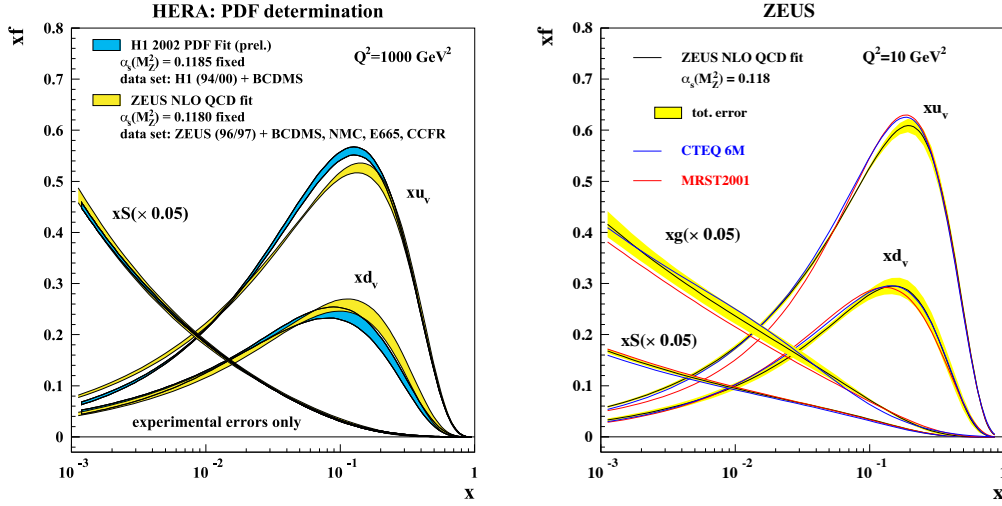
Figure 1.6: Left: Comparison of the PDFs extracted by H1 and ZEUS. Right: Comparison of the PDFs from the ZEUS fit to global fits by MRST2001 and CTEQ6M [10]

1.4.2   Soft Particle Production

A lot of color strings formed between two nuclei when passing through each other at relativistic energy. And quark pairs and gluon pairs are generated in strong color electric field in the region. Number of pair production per unit space-time and unit volume is given by following,

$$\omega(\sigma) = -\frac{\sigma}{4\pi^2} \int_0^\infty dp_T^2 \ln[1 \mp \exp(-\pi p_T^2/\sigma)], \tag{1.16}$$

where the upper part of the expression describe creation rate of a pair for massless spin 1/2 fermion.And the bottom part describe for spin 1 gauge boson. σ is strength of external filed which is given by $\sigma = eE$ for QED, $\sigma \sim gE_c$ for QCD naively with color electric field E_c. Then number of created quark pairs and gluon pairs can be defined using the number of degree of

freedom in color and flavor as follows.

$$\omega_q(\sigma \sim gE_c) \sim N_f \frac{(gE_c)^2}{24\pi}, \omega_g(\sigma \sim gE_c) \sim N_c \frac{(gE_c)^2}{48\pi} \tag{1.17}$$

Therefore generated ratio of quarks and gluons can be described as $\omega_g/\omega_q \sim N_c/N_f$

After freeze-out, momentum distribution of particle i is given by following as hyper-surface integral of thermal distribution.

$$E \frac{d^3N}{d^3p} x = \frac{d^3N}{m_T dm_T dy d\phi_p} = \int_{\sum_f} f(x,p) p^\mu d\sum_\mu \tag{1.18}$$

where p^μ is for momentum vector and $\sum_\mu$ is normal vector to the hyper surface. And local thermal distribution is given by following.

$$f(x,p) = \frac{1}{(2\pi)^3} \frac{1}{\exp(p_\mu u^\mu(x) - \mu(x)/T(x)) \mp 1} \tag{1.19}$$

Then we can calculate particle number density for particle h as integral over particle momentum as follow.

$$< n_h >= d_h \int \frac{d^3p}{(2\pi)^3} \frac{1}{\exp((E_h - \mu_h)/T) \pm 1} \tag{1.20}$$

where d_h is spin degeneracy and E_h is total energy. In heavy ion collisions, particles generated by the process don't distribute uniform in azimuthal direction with respect to the event plane. We need to take care anisotropy distribution of particles described by next section.

1.4.3 Soft Particle Emission in Transverse Plane
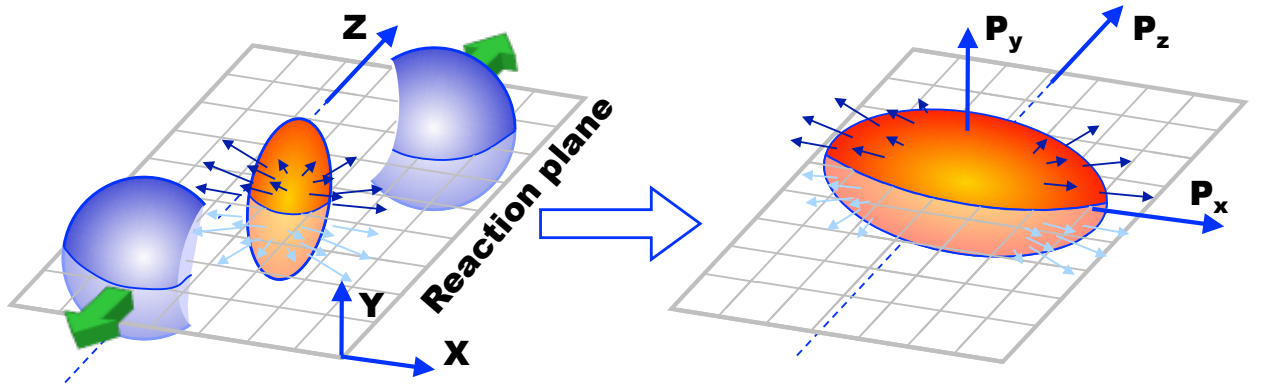
Figure 1.7: Left:A sketch of non-central nucleus-nucleus collisions coordinate space.
Right:Particle expansion of final state after the collision in momentum space

In non-central collision, overlap shape is anisotropic and it looks like almond or rugby ball. This geometrical anisotropy create energy and pressure anisotropy in hot/dense matter while end up with anisotropy of particle production in momentum space. When the mean free path l is smaller than system size R ($l << R$) where by hydrodynamical approach can be applicable. The particle emission pattern is subject to influence by energy/pressure anisotropy.

The particle azimuthal distribution with respect to reaction plane ψ_n in transverse plane can be given by following,

$$E\frac{d^3N}{d^3p} = \frac{d^2N}{2\pi p_T dp_T dy}(1 + \sum_{n=1}^{\infty} 2v_n \cos[n(\phi - \psi_n)]). \tag{1.21}$$

$$\psi_n = \frac{1}{n}(\tan^{-1}\frac{\sum_i w_i \sin n\phi_i}{\sum_i w_i \cos n\phi_i}) \tag{1.22}$$

The strength of the first-order of series on Eq.1.21 is called directed flow. The effect is small in mid-rapidity. The second-order is called elliptic-flow and third-order called triangular flow. The latter two flow influence to azimuthal particle distribution in mid-rapidity and these flow can be described as perfect fluid on hydrodynamics model. And measurements of flow is important in order to understand initial condition of collision and state of hot/dense matter.

1.4.4   Jet Production

In this section,let's consider simple two body scattering with large momentum transfer. As shown Fig.1.8, two parton from protons participates in inelastic collision.
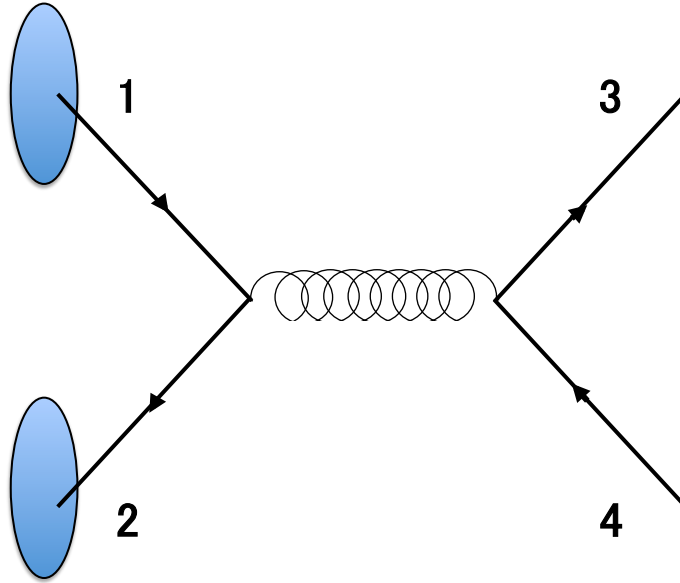
Figure 1.8: A sketch of two body scattering of partons from each nucleus
via gluon with high momentum transfer

The cross section of deep inelastic parton collision in proton-proton collision can be given with PDF and short distance cross-section of two body scattering by,

$$\frac{d^2\sigma_{jet}}{dx_1 dx_2}(pp \rightarrow 3+4) = \sum_{i,j=q,\bar{q},g} f_i(x_1, p_T^2)f_i(x_2, p_T^2)\hat{\sigma}^{ij\rightarrow kl}, \tag{1.23}$$

where i, j, k, l is various parton species$(q, \bar{q}, g)$. In this case, momentum transfer can be chosen as $Q \sim p_T$ in a natural choice. To replace parameters of Eq.1.23 with observable, we use following functions,

$$x_1 = \frac{p_T}{\sqrt{s}}(e^{y_3} + e^{y_4}), x_2 = \frac{p_T}{\sqrt{s}}(e^{-y_3} + e^{-y_4}) \tag{1.24}$$

$$\hat{s} = (p_1 + p_2)^2 = x_1 x_2 s = 2p_T^2[1 + \cosh(y_3 - y_4)] \tag{1.25}$$

$$\hat{t} = (p_1 - p_3)^2 = -p_T^2(1 + e^{-y_3+y_4}) \tag{1.26}$$

$$\hat{u} = (p_2 - p_3)^2 = -(\hat{s} + \hat{t}) \tag{1.27}$$

$$\text{Jacobian} \equiv \frac{\partial(x_1, x_2, \hat{t})}{\partial(y_3, y_4, p_T)} = \frac{2p_T\hat{s}}{s} = 2p_T x_1 x_2 \tag{1.28}$$

where the symbol "^" is used denote Mandelstam variables of two body scattering process.We can rewrite Eq.1.23 as follows,

$$\frac{d^3\sigma^{jet}}{dy_3 dy_4 dp_T^2} = \sum_{i,j} x_1 f_i(x_1, p_T^2)x_2 f_j(x_2, p_T^2)\frac{d\hat{\sigma}^{ij\rightarrow kl}}{d|\hat{t}|}. \tag{1.29}$$

The two body cross section can be given by following.

$$\frac{d\sigma}{d|t|} = \frac{1}{16\pi[s-(m_1+m_2)^2][s-(m_1-m_2)^2]}|M(s,t)|^2 \tag{1.30}$$

And then the invariant amplitude of each two body scattering process is shown in Fig.1.4.4.

The integrated cross section of di-jet production can be obtained as follows

$$\sigma_{jet}(\sqrt{s}, p_0, \Delta y) = \sum_{k,l} \frac{1}{1+\delta_{k,l}} \int_{p_0} dp_T^2 \int_{\Delta y} dy_3 \int_{\Delta y} dy_4 \frac{d^3\sigma^{jet}}{dy_3 dy_4 dp_T^2} \tag{1.31}$$

The part of Kronecker delta take account of symmetry factor of the final state with identical particles. Therefor we can get the number of diet in heavy ion collision as following using overlap function.

$$N_{jet}^{AA}(\sqrt{s}, p_0, \Delta y, b) \approx T_{AA}(b)\sigma_{jet}(\sqrt{s}, p_0, \Delta y) \tag{1.32}$$

Table 1.2: Matrix elements of two-parton scattering and production sub-process in the lowest order perturbative QCD

Process	$|M|^2/(16\pi^2\alpha_s\alpha Q_g^2)$
$q\bar{q} \to q'\bar{q}'$	$\frac{4}{9}\frac{t^2+u^2}{s^2}$
$qq' \to qq'$	$\frac{4}{9}\frac{s^2+u^2}{t^2}$
$q\bar{q}' \to q\bar{q}'$	$\frac{4}{9}\frac{s^2+u^2}{t^2}$
$q\bar{q} \to q\bar{q}$	$\frac{4}{9}\left(\frac{t^2+u^2}{s^2} + \frac{s^2+u^2}{t^2}\right) - \frac{8}{27}\frac{u^2}{st}$
$qq \to qq$	$\frac{4}{9}\left(\frac{s^2+u^2}{t^2} + \frac{s^2+t^2}{u^2}\right) - \frac{8}{27}\frac{s^2}{ut}$
$gg \to q\bar{q}$	$\frac{1}{6}\frac{t^2+u^2}{tu} - \frac{3}{8}\frac{t^2+u^2}{s^2}$
$q\bar{q} \to gg$	$\frac{32}{27}\frac{t^2+u^2}{tu} - \frac{3}{8}\frac{t^2+u^2}{s^2}$
$qg \to qg$	$-\frac{4}{9}\left(\frac{s^2+u^2}{su} + \frac{s^2+u^2}{t^2}\right) - \frac{8}{27}\frac{u^2}{st}$
$gg \to gg$	$\frac{9}{2}\left(3 - \frac{tu}{s^2} - \frac{su}{t^2}\right) - \frac{st}{u^2}$
$q\bar{q} \to g\gamma*$	$\frac{8}{9}\frac{t^2+u^2+2s(s+t+u)}{tu}$
$qg \to q\gamma*$	$-\frac{1}{3}\frac{s^2+u^2+2t(s+t+u)}{su}$

Number of particle produced by jets should strongly depend on number of produced jets. So we can give number of produced particles in unit longitudinal momentum fraction z by jets as following.

$$\frac{dN_{particle}}{dz} = N_{jet}^{AA} \times F(z,Q) \tag{1.33}$$

$$F(z,Q) = \sum_{i,h} D_i^h(z,Q) \tag{1.34}$$

where $D_i^h(z,Q)$ is production ratio of hadron h for each parton species i so called "fragmentation function". The production ratio could not be calculated by perturbative QCD, so that the variation with Q can be predicted provided Q is sufficiently large. If we would like to know the production ratio, we have to determine in experiment.

In left figure of Fig.1.9 the predicted transverse momentum distribution of neutral pions and inclusive charged hadrons is shown. Which is calculated on pQCD for Leading order. In LHC, a huge number of particles are produced compared with the number of production in RHIC energy. Therefor the experiments at LHC has statistical advantage in measurements for high momentum prove. Then we can do direct measurements on jet measurements using high statistics which we could not do due to statistical limit in experiments with low collision energy.

In right figure of Fig.1.9 provide production ratio of neutral pions and charged particles. The neutral pion ratio is rapidly decreasing with transverse momentum due to production of kaon and proton is dominant in high momentum region. That indicate high momentum particles come from jets via fragmentation so that such kaons and proton should be produced by fragmentation of partons. We have to remark that the ratio is higher in LHC than in RHIC energy. The effects come from gluon saturation in projectile nucleus as we see in Fig.1.6. Then number of produced neutral particles increase compared with the number of them in RHC energy. We can

also use information of difference of production mechanism between quark recombination and fragmentation which is seen in pion production ratio with respect to proton to investigate jet modification in QGP.
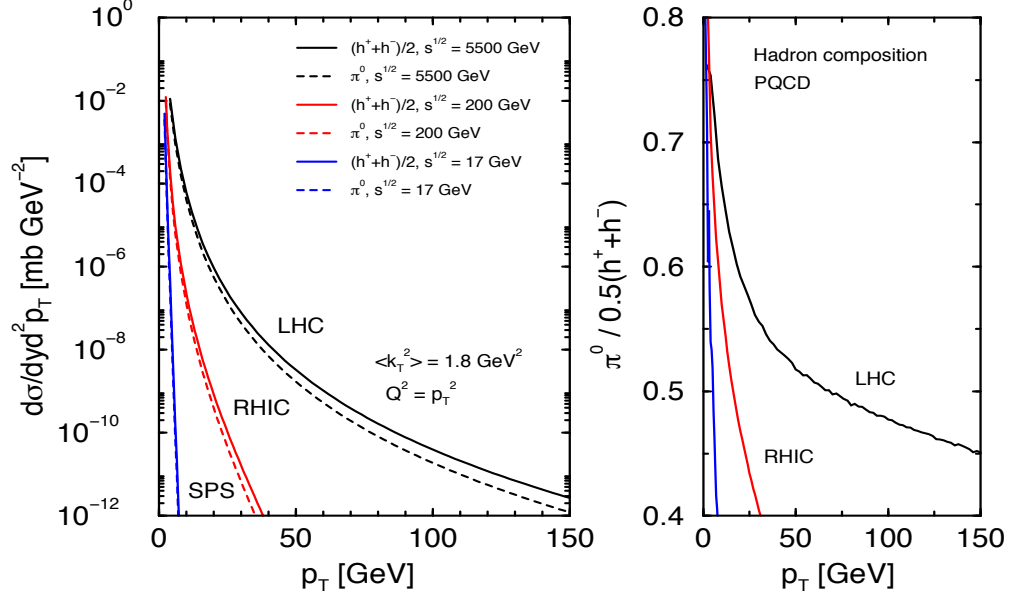
Figure 1.9: Left:The predicted LO differential cross section for inclusive neutral pions and charged particle production at mid-rapidity $y = 0$ in pp collision for $\sqrt{s} = 17, 200$ and 500GeV.Right:The ratio of neutral pions to inclusive charged hadrons as function of transverse momentum p_T [11]

1.4.5 Energy Loss of Parton in QGP[12]

In heavy ion collisions at RHIC and LHC energies, we have seen the results that the particle yield in high p_T region is suppressed compared with the yield of *pp* collision. The cause is considered that inside partons of jet lost their energy by several effects. We can describe amount of energy loss of a parton using parton position l,path length L, scattering probability density $dP(l)/dl$ and mean free path λ in general,

$$\Delta E = \int_0^L dl \frac{dP(l)}{dl} \lambda(l) \frac{dE(l, E)}{dl}, \frac{dP(l)}{dl} = \frac{1}{\lambda(l)} \exp(-l/\lambda(l)). \qquad (1.35)$$

It is considered that there are two mechanisms.The first one is collisional energy loss when the parton lose their energy colliding constituents partons of QGP. Latter one is radiative energy loss when the parton radiate gluons.

Thus,Eq.1.35 can be describe by sum of energy loss as follows.

$$\Delta E = \Delta E_{\text{collisional}} + \Delta E_{\text{radiative}} \qquad (1.36)$$

Collisional Energy Loss

The collisional energy loss due to elastic scattering with high-momentum transfer has been origi-
nally estimated by Bjorken as following.

$$\frac{dE_{\text{collisional}}}{dl} = \frac{1}{4T\lambda\sigma} \int_{\mu_D^2}^{t_{max}} dt \frac{d\sigma}{dt} dt \tag{1.37}$$

$$\frac{d\sigma}{dt} \approx C \frac{2\pi\alpha_s^2(t)}{t^2} \frac{E^2}{E^2 - m_p^2} \tag{1.38}$$

where $\mu_D^2(T) \approx 4\pi\alpha_s T^2(1 + N_f/6)$ is Debye screening mass squared and $t_{max} = [s - (m_p + m_0)][s - (m_p - m_0)^2]/s$ is maximum momentum transfer with $s = 2m_0 E + m_0^2 + m_p^2$. In fact, the
energy loss also has effects due to elastic scattering with low momentum transfer. However the
process does not contribute much to the total collisional loss in compared with high-momentum
scattering (due to absence of large factor $\sim \ln(E/\mu_D)$ where μ_D is the Debye screening mass).
According to a simple estimation[13], scattering angle of thermalized particle as function of
transfer momentum squared can be given by,

$$\theta_Q = \tan^{-1}(\frac{2m_0}{\sqrt{Q}}). \tag{1.39}$$

Radiative Energy Loss

Here are amount of energy loss in unit pass length by massless gluon radiation estimated by
BDMS framework.

$$\frac{dE_{\text{radiative}}}{dl} = \frac{2\alpha_s(\mu_D^2)C_R}{\pi L} \int_{\omega_{min}}^{E} d\omega[1 - y + \frac{y^2}{2}] \ln|\cos(\omega_1\tau_1)| \tag{1.40}$$

$$\omega_1 = \sqrt{i(1 + -y + \frac{C_R}{3}y^2)\bar{\kappa} \ln \frac{16}{\bar{\kappa}}}, \bar{\kappa} = \frac{\mu_D^2\lambda_g}{\omega(1 - y)} \tag{1.41}$$

In the BDMS frameworks, the strength of multiple scattering is characterized by the transport
coefficient $\hat{q} = \mu_D^2/\lambda_g$ where λ_g is mean free path of gluons. In principle mean free pass can be
given by $\lambda = 1/\rho\sigma(\rho \sim dN_g/dy$ in GLV framework[14], $\propto T^3$ in BDMS framework[15]). So
energy loss by gluon radiation strongly related to properties of QGP. It also means, if energy loss
correlate with pass length we can have knowledge of properties of QGP using jet modification
as probe. If gluon emission lead to gauss function, angular spectrum of emitted gluon given by
[13],

$$\frac{dN^g}{d\theta} \propto \sin\theta \exp(-\frac{(\theta - \theta_0)^2}{2\theta_0^2}) \tag{1.42}$$

where θ_0 is σ of gaussian.

Probe of Energy Loss

Because of energy loss of partons, momentum distribution of particles also modified. Then high momentum particles looks re-distributed into low momentum particles. And if jet modification has pass length dependence, energy of reconstructed jet also has pass length dependence so that smearing of jet shape depends on pass length. In heavy ion collision, jets with small pass length come from surface of QGP. So if we trigger shape jet, away-side jet should be strongly modified due to trigger effects.

1.5 Experimental Results

Let we show current experimental results concerning jet modification before starting to describe the motivation of the thesis. You will see the history and progression of jet modification measurement in this section.

1.5.1 At RHIC

a) Suppression of High Momentum Particles (jet)
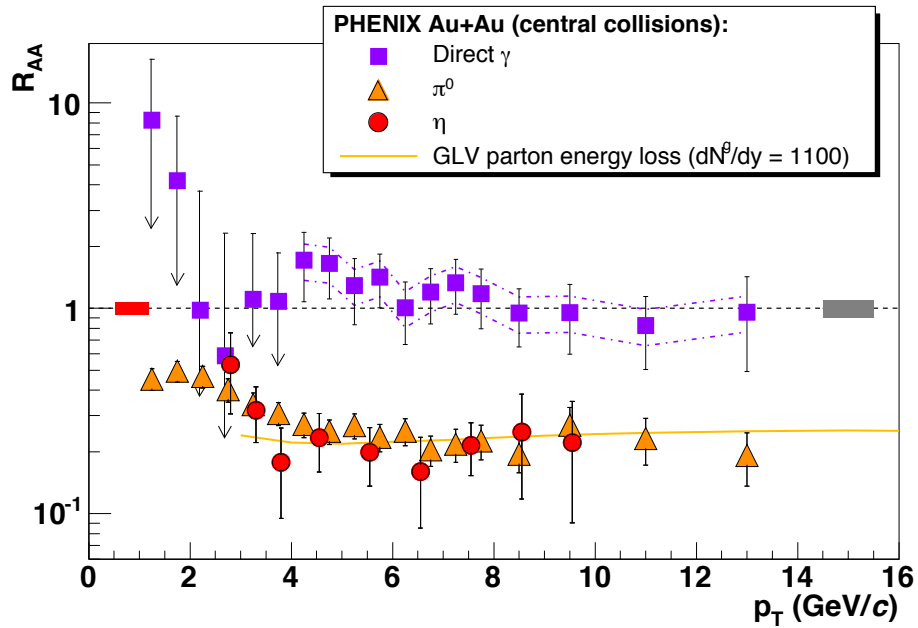
Figure 1.10: Nuclear modification factor R_{AA} as function of p_T for η, π^0 and γ in central collision of Au+Au collision at $\sqrt{s_{NN}} = 200\text{GeV}/c$[16]. The solid yellow curve is a parton energy loss prediction for a medium with density $dN^g/dy = 1100$

Manifestation of the characteristic energy loss of parton is

a) Suppression of high momentum particles (jet)

b) Loss of away-side jet

In the beginning of jet modification measurements,suppression of particle production in high momentum region were measured with experiments at the RHIC. Fig.1.10 provides us yield ratio for neutral π,η mesons and direct γ which is measured in Au+Au collisions with respect to the yield measured in pp collisions called R$_{AA}$. The definition of R$_{AA}$ of particle species h is following.

$$R_{AA}^h(p_T, b) \equiv \frac{\frac{dN^{AA \to h+X}}{d^2 p_T}}{N_{bin}(b)\frac{dN^{pp \to h+X}}{d^2 p_T}} \tag{1.43}$$

Direct γ in high p_T range are produced by scattering process with high momentum process like as jet. However γ has no color charge, so they are not sensitive to interaction with matter which is constituents of QGP. On the other hands, neutral π meson produced by partons via hadronization characterized by fragmentation function. But Coulomb effects are minimized after the hadronization because the π^0 mesons has no charge. As far as we see Fig.1.10 the yield of π^0 of Au+Au is suppressed compared with pp collisions scaled by number of collisions. The fact indicates that π^0 production is affected by some effects before hadronization like as parton interaction in hot/dense matter.

b) Loss of Away-Side Jet

Fig1.11 shows us associated charged particle yield as function of azimuthal direction with respect to trigger particle which is measured at STAR experiment. In bottom figure of Fig.1.11, it is compared that particle yield from pp,d+Au and Au+Au collisions.Around near-side to trigger particle, there are no drastic modification, however, in away-side from trigger particle we can see strong yield suppression in Au+Au collisions compared with the other.It is considered that this modification also come from jet modification effects, in near-side surface bias in trigger particle due to jet modification should contain, so near side peak looks almost same as the peak from pp collisions. In contrast, associate particles distributions are constrained by trigger particle, then yield from Au+Au suppress strongly.

Several results were measured which indicate strong modification in high momentum particle region due to jet modification. However, they could not measure jet directory because of low statistics due to collision energy. From end of 2010, LHC start circulate heavy ion. At LHC energy,we can reconstruct jets with fine resolution and efficiency and we are in new stage for these kind of measurements.
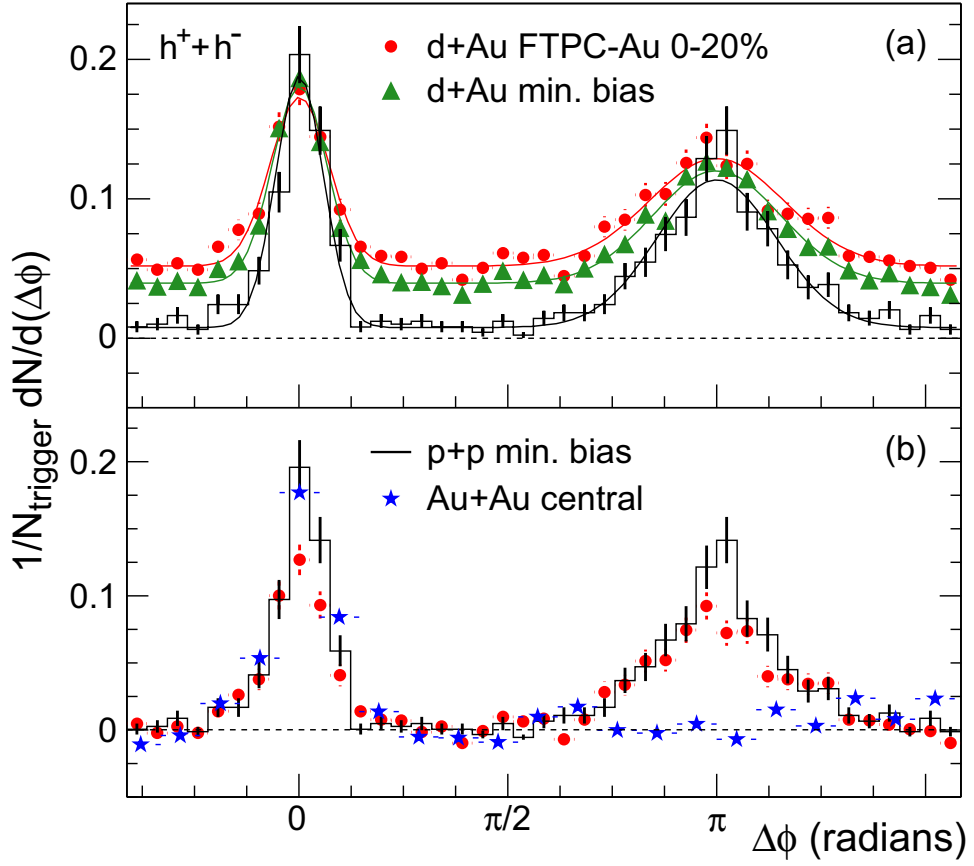
Figure 1.11: (a) Two-particle azimuthal distributions for minimum bias and central d+Au collisions and for pp collisions (b)Comparison of two-particle azimuthal distributions for central Au+Au collisions and d+Au collisions and pp collisions [17]

1.5.2 At LHC

The experiments at LHC started direct measurements for jet and jet modification. The clear unbalances di-jet which is reconstructed with CMS detector is shown in Fig.1.12. The figure shows transverse energy for all particles in $\phi - \eta$ plane.They can reconstruct both of charged particles and neutral particles(including photon), the also can reconstruct full jet using all particles.We can see sharp peak with huge transverse energy as leading jet and small peak compared with leading jet energy at opposite side in azimuthal direction.
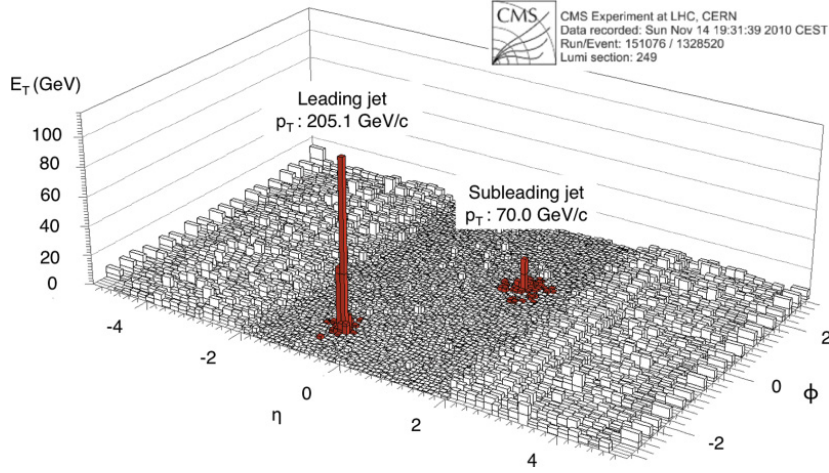
Figure 1.12: Example of an unbalanced di-jet in a Pb-Pb collision event at $\sqrt{s_{NN}} = 2.76$ [18]

a) Suppression of High Momentum Particles (jet)

At LHC, we have sufficient statistics of jet to measure jet suppression instead of particle suppression as we see in Fig.1.10. Fig.1.13 shows nuclear modification factor of jets which is measured by CMS. As same as suppression of particle production, jet production also strongly suppressed in central collision in particular.
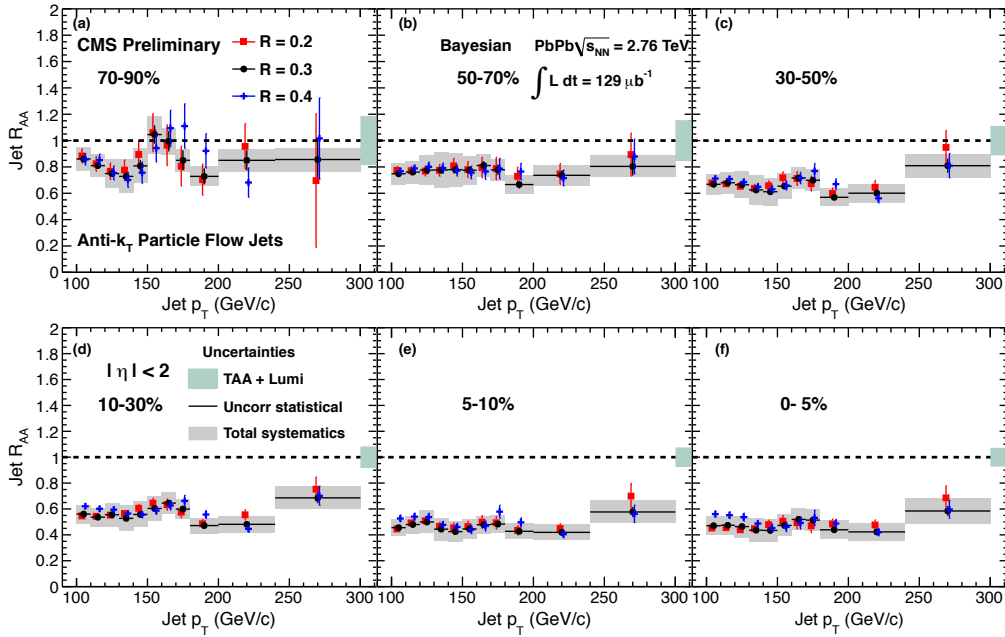
Figure 1.13: Centrality dependence of jet Jet R_{AA} for different cone size with anti-k$_T$ algorithm [19]

b) Loss of Away-Side Jet
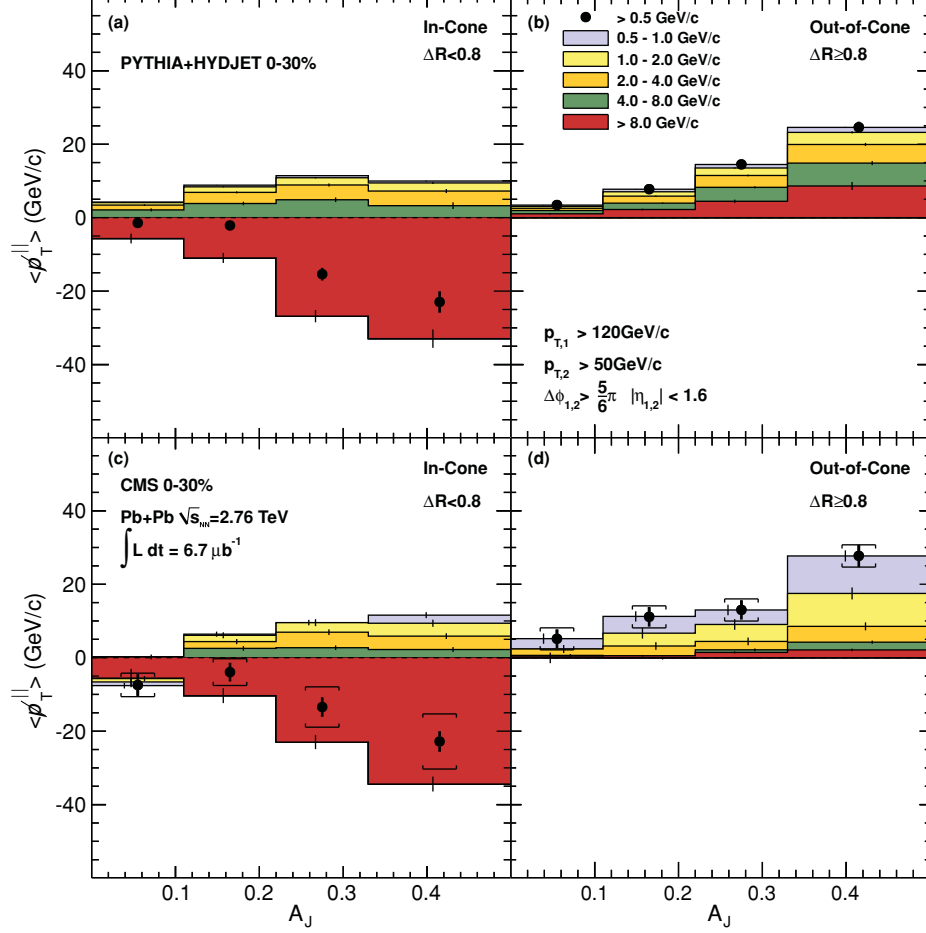
Figure 1.14: Average missing transverse momentum $< \not{p}_T^{||} >$ for tracks with $p_T > 0.5$ GeV/c, projected onto the leading jet axis (solid circles). The $< \not{p}_T^{||} >$ values are shown as a function of di-jet asymmetry A_J for $0\%-30\%$ centrality, inside ($\Delta R < 0.8$) one of the leading or subleading jet cones (left-hand side) and outside ($\Delta R > 0.8$) the leading and subleading jet cones (right-hand side). For the solid circles, vertical bars and brackets represent the statistical and systematic uncertainties, respectively. For the individual p_T ranges, the statistical uncertainties are shown as vertical bars.

The results in Fig.1.14 are also from CMS experiment. These figure shows average missing transverse momentum ($< \not{p}_T^{||} >$) as function of di-jet momentum asymmetry($A_j = (p_T^{\text{lead}} - p_T^{\text{sub-lead}})/(p_T^{\text{lead}} + p_T^{\text{sub-lead}})$). Missing transverse momentum is given by

$$\not{p}_T^{||} = \sum_i -p_T^i \cos(\phi_i - \phi_{\text{leading-jet}}). \tag{1.44}$$

Two event set were use for the measurement,one is data of Pb-Pb collision at $\sqrt{s_{NN}} = 2.76$ TeV and PYTHIA jet embedded HYDJET Monte Carlo event anchored the data. In latter event set don't consider jet modification effects and other un-expected effects. So in principle, we can see jet modification effects comparing the results of two event set. And they focus on the missing energy in the region close to jet axis (ΔR(track-jet)) and other region. By doing so, we can compare how much energy missing in jet and how re-distribute to out of jet.

There are no much difference in left two figure, but you see drastic difference in right two figure. These figure tell us in away-side of leading jet direction, production of high momentum particles are suppress and the energy re-distributed to low-momentum particles production. This results consistent with the picture which Fig.1.11 shows.
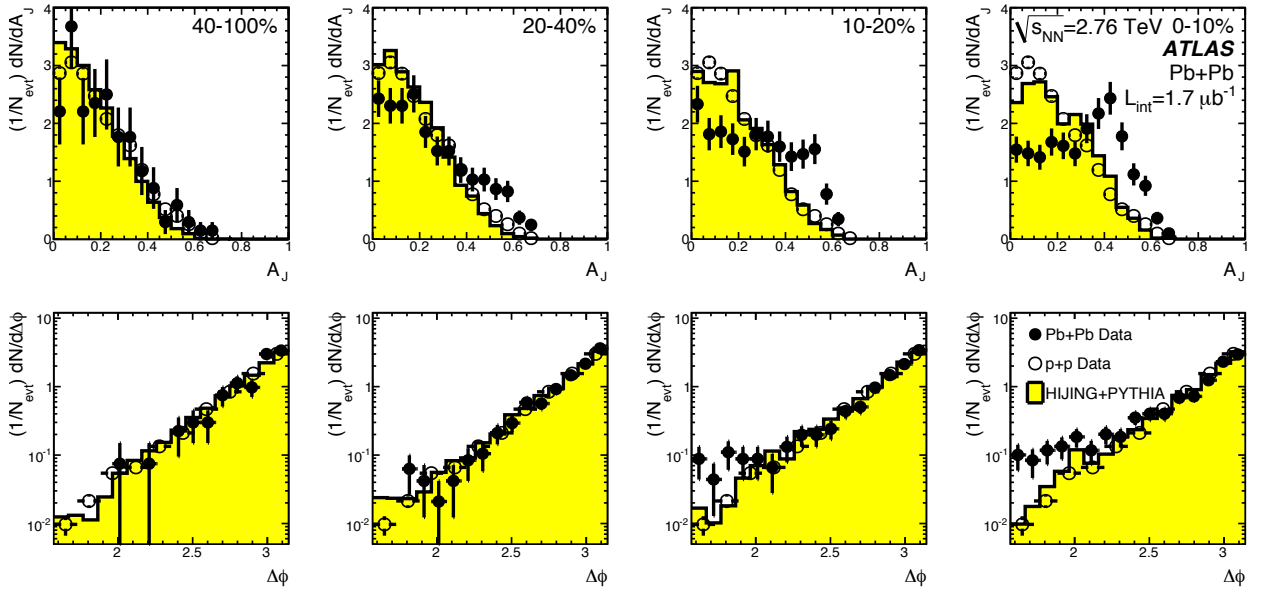
Figure 1.15: (top) Di-jet asymmetry distributions for data (points) and un-
quenched HIJING with superimposed PYTHIA di-jets (solid
yellow histograms), as a function of collision centrality (left
to right from peripheral to central events). Proton-proton
data from $\sqrt{s} = 7$ TeV, analyzed with the same jet selec-
tion, is shown as open circles. (bottom) Distribution of $\Delta\phi$,
the azimuthal angle between the two jets, for data and HI-
JING+PYTHIA, also as a function of centrality [20]

If jets are wider by jet modification, reconstructed energy should be smaller and di-jet axis open angle should be larger. Fig.1.15 shows di-jet asymmetry distribution (top) and di-jet open angle distribution. In top figure, A_j is larger with centrality and difference between close point and open point is also larger with centrality. That conform away-side jets with respect to leading jet loss their energy(momentum). The reason is, if jets are wider due to jet modification, reconstructed momentum should be smaller with respect to narrow jets.

In experiments at LHC started measurements for jet modification jet by jet. We got same tendency of jet modification results which were measured at RHIC. However energy re-distribution in jet itself is still unknown, and we could not see jet modification effects in particle which distribute in away-side as same as in near-side because $< \not{p}_T^{\parallel} >$ shows us momentum balance of triggers di-jet event. To investigate particle(energy) re-distribution by jet modification, new analysis method is needed. And we have to measure same kind of effects in the momentum range between RHIC and ATLAS, CMS.

1.6 Thesis Motivation

In this chapter, we reviewed the results which revealed jet modification effects at RHIC and LHC energy. The results indicated that jet production is suppressed and missed energy of high energy particles re-distributed into the energy to produce low momentum particles. And the results also indicate that it is pass length dependence in jet modification. Here are summary of the knowledge we have from the results.

- Jet and high momentum particles production are suppressed

- Away-side peaks looks loosing their energy. That indicate jet modification has pass length dependence.

- Missing energy of high momentum particles redistribute to the energy to produce low momentum particles in out-of cone region

At RHIC energy, it is measured yield ratio of particles in nuclear-nuclear collisions with respect to proton-proton collisions and away-side yield modification in two particle correlations. These results give us knowledge of jet modification, however , it is difficult to reconstruct jets due to collision energy. Therefor we can not extract information of jet modification directory.

At LHC energy, it is analyzed associated particle distribution with jet axis. Then we can know detail of relation of jet and particle distribution affected by jet modification. However to reduce effects which uncorrelated to jet like elliptic flow, CMS measured missing energy in di-jet event. Therefor we lose information of inside of jet affected jet modification. In particular information of particle re-distribution for each leading jet and sub-leading jet. And we also lose angle information of broadening of re-distributed particles.

As we had seen theory of jet modification, angle information is one of important observable because that correlated to gluon emission angle and scattered angle related to jet modification described by Eq.1.39 and Eq.1.42. To understand picture of jet modification, we need to know particle re-distribution with spread angle information. For the reason, we established the method of azimuthal correlation between jet and charged particles. To measure jets modification, we need to subtract background energy precisely. So we also established the method of background subtraction which take into account elliptic flow and triangular flow.

In this thesis, we present measurements of particle distribution in jet for Pb-Pb collisions and pp collisions using jet-particle azimuthal correlation. Then we draw out information of particle re-distribution with angle comparing the particle distribution of Pb-Pb collisions and pp collisions. Then we will discuss concerning concrete pictures in jet modification and their pass length dependence from the results of particle distribution.

Chapter 2

Experimental Apparatus

As seen in previous chapter, heavy ion collision is a unique method for research of hot/dense matter like as QGP. The ALICE detector is composed by multiple detectors for several physical purpose to study QGP. In this chapter we describe the overview of the Large-Hadron Collider(LHC) and purpose of each detectors with their detector performance. In this measurements, we use SPD which is innermost detector of ITS and VZERO detector as detector for online event trigger. We also use ZDC to apply timing cuts in offline for Pb-Pb collisions. For reconstruction of charged tracks, we use ITS and TPC in central barrel.

2.1 Large Hadron Collider[21]
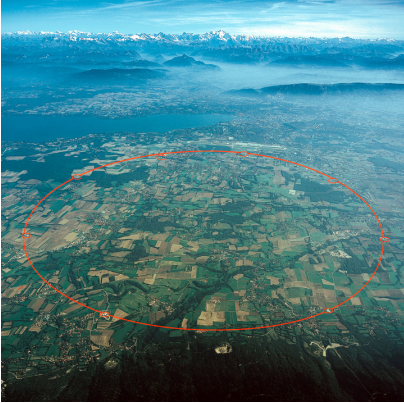
Figure 2.1: Aerial view of LHC ring
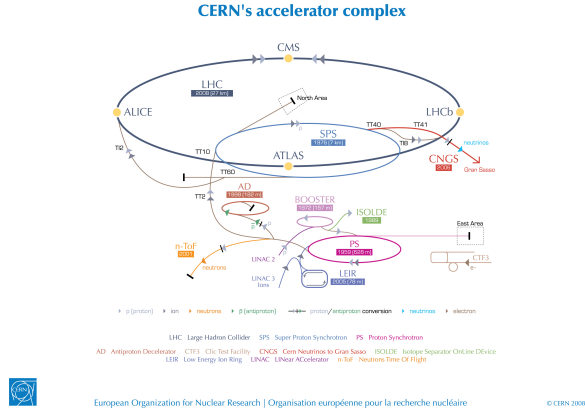
Figure 2.2: LHC and pre-accelerators

A Large Hadron Collider (LHC)[22] is located CERN laboratory over border between Switzerland and France. The LHC was built for particle and nuclear physics with the highest energy in the world on the tunnel of LEP ring. The LHC has two rings which length is 27km go the opposite direction each other. And LHC has two pre-accelerators called Super Proton Synchrotron(SPS) and Proton Synchrotron(PS) to accelerate nucleon and nuclear to the LHC injection energy. The LHC was designed that it can run at $\sqrt{s} = 14$ TeV for proton-proton collision and $\sqrt{s_{NN}} = 5.5$

TeV for lead-lead collision at the maximum energy.

The first beam were circulated successfully on 10th September 2008. It was started physics run for proton-proton collision since 2009 after long shutdown to investigate and fix electrical problem on the magnets at the previous year runs. Then physics run for Pb-Pb collision started since end of 2010. LHC has two huge experiments ATLAS[23], CMS[24] and two middle experiments ALICE, LHCb[25].

Table2.1 provide summary of parameters nominal proton beam operation. LHC can be filled banshees 25ns steps in full bunches operation. And LHC can accelerate proton to 7TeV from injection energy 450GeV.

Table 2.1: LHC beam parameters relevant for the luminosity lifetime [21]

		Injection	Collision
Beam Data			
Proton Energy	[GeV]	450	7000
Relativistic gamma		479.6	7461
Number of particles per bunch		1.15×10^{11}	
Number of bunches		2808	
Longitudinal emittance (4σ)	[eVs]	1.0	2.5
Transverse normalized emittance	[μm rad]	3.5	3.75
Circulating beam current	[A]	0.582	
Stored energy per beam	[MJ]	23.3	362
Peak Luminosity Related Data			
RMS bunch length	[cm]	11.24	7.55
RMS beam size at the IP1 and IP5	[μm]	375.2	16.7
RMS beam size at the IP2 and IP8	[μm]	279.6	70.9
Geometric luminosity reduction factor F		-	0.836
Peak luminosity in IP1 and IP5	[cm^{-2}sec^{-1}]	-	1.0×10^{34}
Peak luminosity per bunch crossing in IP1 and IP5	[cm^{-2}sec^{-1}]	-	3.56×10^{30}

Fig.2.3 provide integrated luminosity of pp collisions at $\sqrt{s} = 7$ TeV and Pb-Pb collisions at $\sqrt{s_{NN}} = 2.76$ TeV which is token in 2010. The red point lower than the other. The other experiments use silicon detectors as tracking system with high speed readout. But ALICE use a type of drift chamber to reconstruct charged track called TPC. In particular, the rate of data taking in ALICE is limited by recording rate of TPC. Because the TPC of ALICE use multi-wire proportional chamber(MWPC) as readout, it's not enough to use gating to reduce ion back flow during high rate pp collisions of LHC provide. However we are going to update readout of TPC from MWPC to Gas Electron Multiplier(GEM). If the updating succeed, we can take data with more high rate.
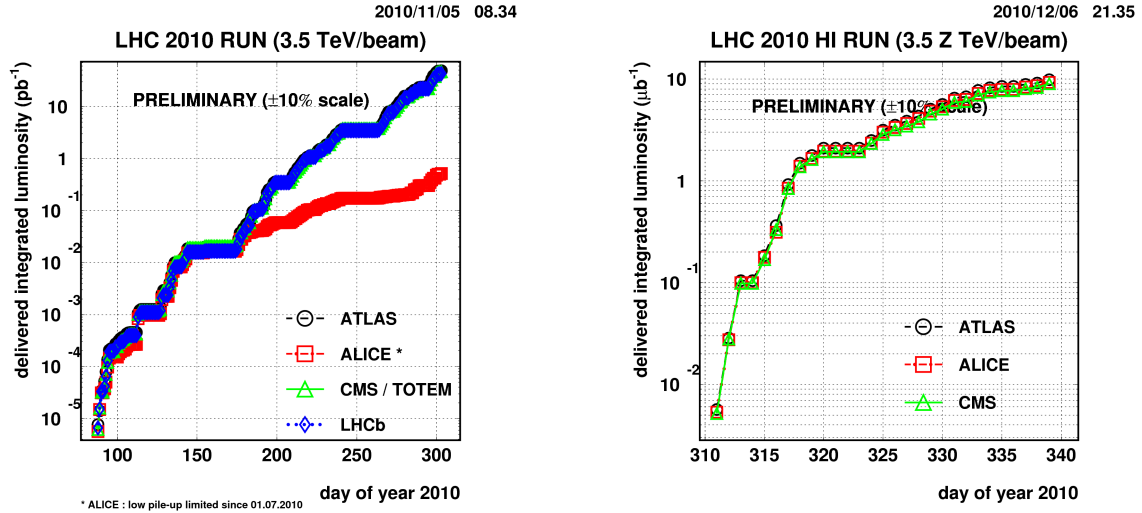
Figure 2.3: Left : Integrated Luminosity of pp collisions at $\sqrt{s} = 7$ TeV in 2010,Right:Integrated Luminosity of Pb-Pb collisions at $\sqrt{s_{NN}} = 2.76$ TeV in 2010

2.2   ALICE detector overview
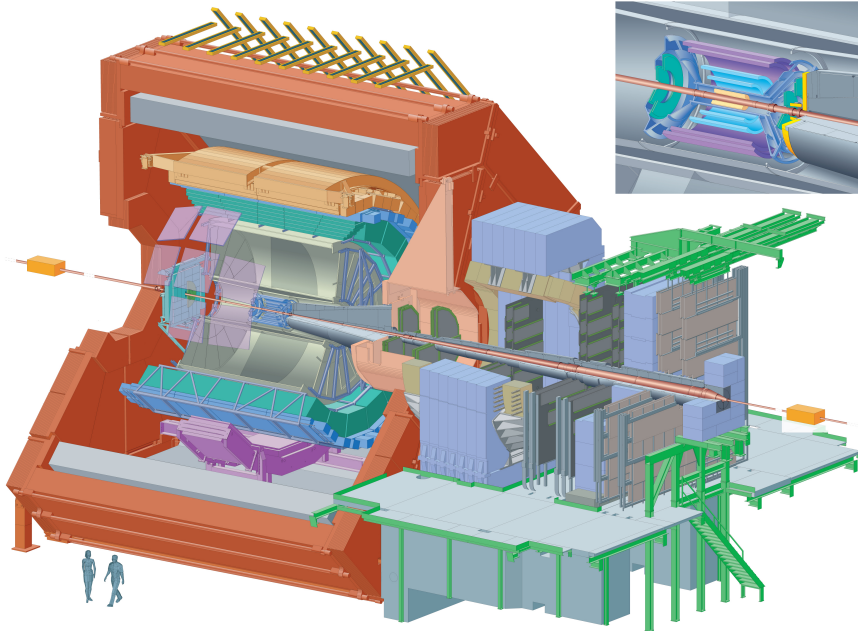
Figure 2.4: Overview of ALICE detector

A Large Ion Collider Experiment(ALICE) was build as general-purpose detector for measurements of ultra relativistic heavy ion collision at LHC. So ALICE was optimized to be capable

of measuring thermal bulk properties.Especially ALICE has advantages in charge particle recon-struction with particle identify in very low momentum region ∼100MeV compared with ATLAS and CMS for measurements of Pb-Pb collision. Table2.2 provide us over view geometrical prop-erties of sub-detectors of ALICE detector. In latter section we will describe more detail of sub-detectors.As far as we can see on the table ALICE is not symmetrical detector to η direc-tion. We call A-side the side beam pipe go to ATLAS site and C-side the other direction which go to CMS site.

Table 2.2: ALICE detector overview

Detector	Radius	Rapidity	Azimuthal Range	Purpose
Global Detectors				
T0	-	$-3.3 < \eta < -2.9$	360°	timing supply
		$4.5 < \eta < 5.0$		
V0	-	$-3.7 < \eta < -1.7$	360°	event trigger
		$2.8 < \eta < 5.1$		event plane determination
				centrality determination
ZDC	-	$\eta \sim -8.8$	360°	centrality determination
		$\eta \sim 8.8$		
Central Detectors				
ITS	$4 < R < 44$ cm	$-0.9 < \eta < 0.9$	360°	charged particle tracking
				vertex reconstruction
TPC	$90 < R < 250$ cm	$-0.9 < \eta < 0.9$	360°	charged particle tracking
TRD	$290 < R < 370$ cm	$-0.9 < \eta < 0.9$	360°	electron identification
TOF	$370 < R < 400$ cm	$-0.9 < \eta < 0.9$	360°	hadron identification
EMCal	430 cm $> R$	$-0.7 < \eta < 0.7$	110°	determine particle energy
PHOS	460 cm $> R$	$-0.12 < \eta < 0.12$	13°	determine photon energy
HMPID	470 cm $> R$	$-0.6 < \eta < 0.6$	57.6°	high momentum particle identification
Forwared Detectors				
FMD	-	$-3.4 < \eta < -1.7$	360°	forward multiplicity determination
		$1.7 < \eta < 5.0$		
PMD	-	$1.8 < \eta < 2.6$	360°	photon multiplicity determination
MUON spectrometer	-	$-4.0 < \eta < -2.5$	360°	forward muon detection

2.3 Magnets at ALICE

ALICE has two type of large magnets. First one is large solenoidal magnet called ALICE magnet which was used at L3 experiment[26]. The magnet is operate to apply 0.5T in central barrel to bend track of charged particles for particle identification. In ALICE magnet, we have tracking detectors, PID detectors and calorimeters. The latter magnets is large dipole magnet which also used at L3 experiment. The magnet concept has been elaborated in several design phases. A first decision was taken in 1996 to opt for a magnet with room temperature coils. The dipole magnet is located in middle of muon spectrometer and just after of ALICE magnet bricking muon chambers after absorber. The magnet is used to bend track of muons.

2.4   Global detectors

2.4.1   T0 [27]

The T0 detector consists a array of fine-mesh PMTs with 12 Cherenkov radiators for both side A and C (see the detector for C-side in Fig.2.5). T0 at C-side locate very close to end cap of ITS.But T0 at A-side locate a bit far from collision point. T0 detector is designed to get fast timing with fine timing resolution ($\sigma \sim 50$ps) signal for Level-0 trigger and reference time for TOF in ALICE magnet(0.5T). In addition T0 signals are used as "wake up signal" for TRD. And the fast signal is used as start signal for PID by TOF and timing estimation of ZDC hit for offline event trigger.
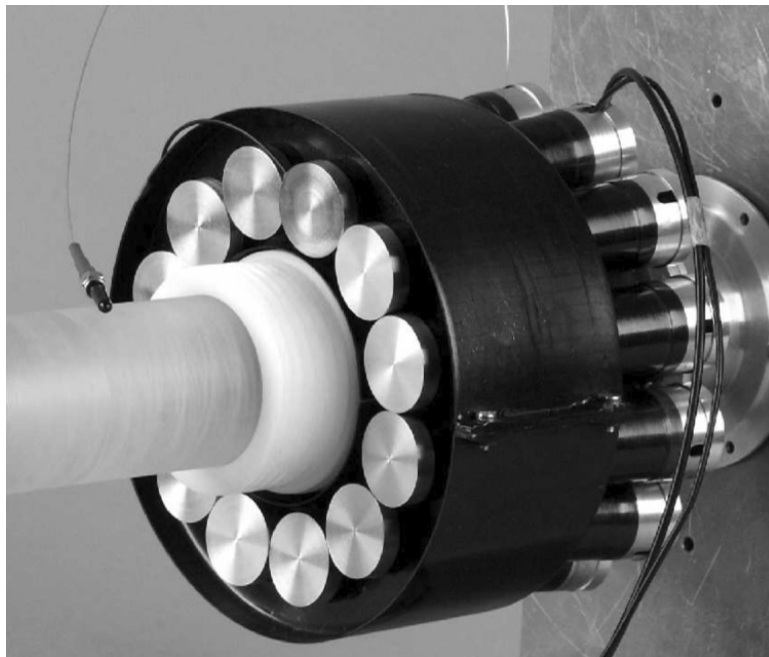
Figure 2.5: A photo of one module of T0 detector. The detector composed
by 12 Cherenkov radiators with photo multiplier

2.4.2   VZERO [27]

The V0 detector is located close to T0 detector of both side. The detector is composed of scintillators(4rings,16sectors) arranged radially. It was designed for main functions of the detector as following.

- To provide minimum-bias trigger for central barrel detectors in pp and Pb-Pb collisions.

- To determine centrality in Pb-Pb collisions

- To determine event plane in Pb-Pb collisions
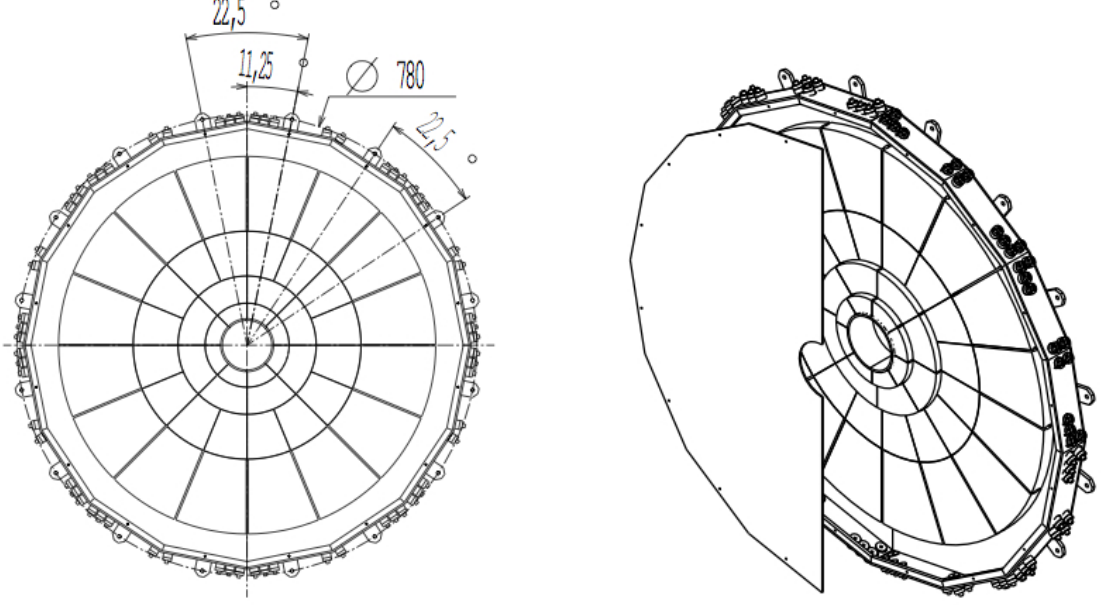
Figure 2.6: Overview of VZERO detector. The detector composed by scintillators with PMT

To meet the requirements,it provide a high and uniform light signal from the one minimum-ionization particle(MIP) with fine timing resolution($\sigma < 1$ns). Trigger efficiency is over than 80%in pp collision and almost 100% in Pb-Pb collisions.

2.4.3 Zero Degree Calorimeter(ZDC) [28]

The ZDC is located far from interaction point(IP) over than 100m. The detector is built with classical technics of calorimeter which composed of sandwich of lead and scintillator to measure particle energy. By measuring energy of particles which didn't contribute the collision, we can suppose collision geometry. If we specify the energy of nucleons E_A per nucleon and spectator E_S, we can have simple relation of number of interacting nucleons N_p as following.

$$N_p = A - E_S/E_A \tag{2.1}$$

where A is the number of the ion.Then we can calculate number of participants in Glauber framework as following.

$$N_p(\vec{b}) = \int d^2s \{ A T_A(\vec{s}) [1 - (1 - \sigma_N T_B(\vec{b} - \vec{s}))^B]$$
$$+ B T_B(\vec{b} - \vec{s}) [1 - (1 - \sigma_N T_A(\vec{s}))^A] \} \tag{2.2}$$

where A,B are mass numbers of colliding nuclei and " $\vec{}$ " means two-dimensional vector in transverse plane. We can get impact parameter from relation of dropped energy in ZDC and number of participants.The resolution of impact parameter of ALICE-ZDC is shown Fig.2.8 which is estimated by GEANT simulation.
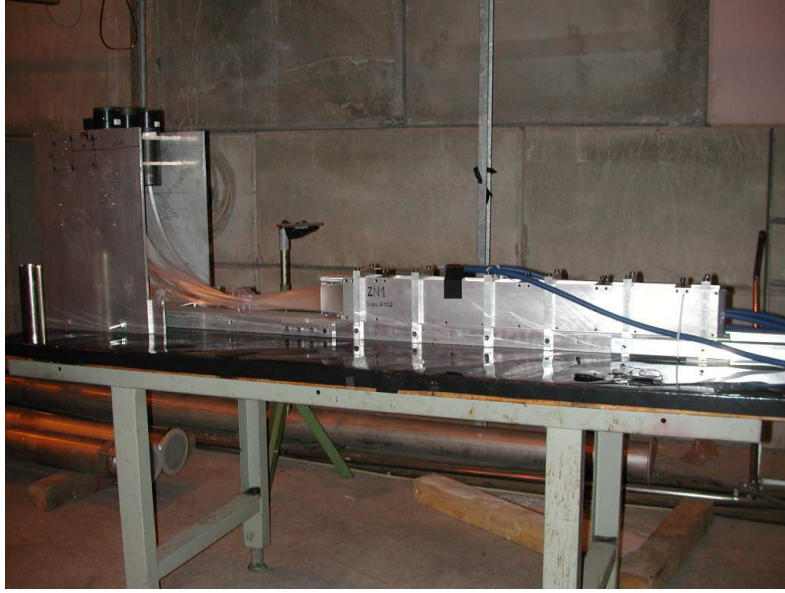
Figure 2.7: A photo of a super module of Zero Degree Calorimeter. The detectors are a type of sandwich of lead and scintillator with PMT
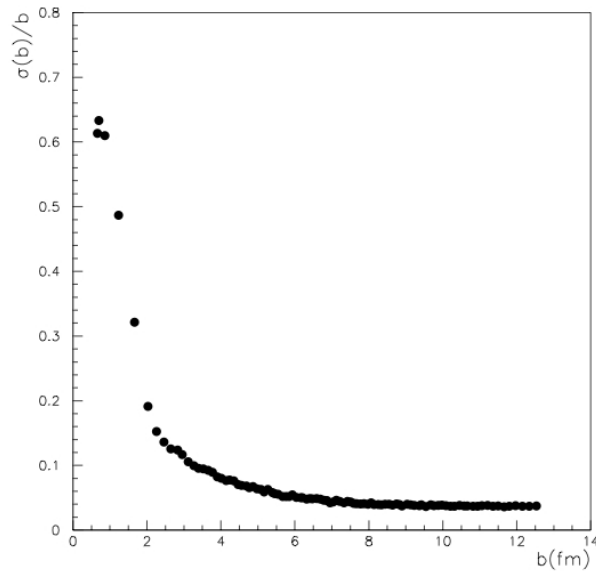
Figure 2.8: Resolution on the impact parameter for the ALICE ZDCs which is estimated by GEAN simulation

2.5 Central detectors

Fig.2.9 shows cross section view of central barrel. In mid-rapidity, we have many kind of detectors for several physics purpose.Mainly, we need detectors for track reconstruction with fine resolution and efficiency, particle identify and estimate energies of charged particles and photons. For tracking, silicon tracking detector is located most inferrer in central barrel the 1st layer and 2nd layer of ITS is used as trigger detector for minimum bias trigger as well as VZERO detectors. Just outer of ITS, TPC cover whole azimuthal acceptance. The TPC is another main tracking system to reconstruct with large solid angle. Then we have two kind of PID detectors called TRD and TOF. In outermost layer, we have two type of calorimeter and ring imaging Cherenkov counter for PID of high momentum particles.In the section, we will explain more detail of detectors in central barrel.
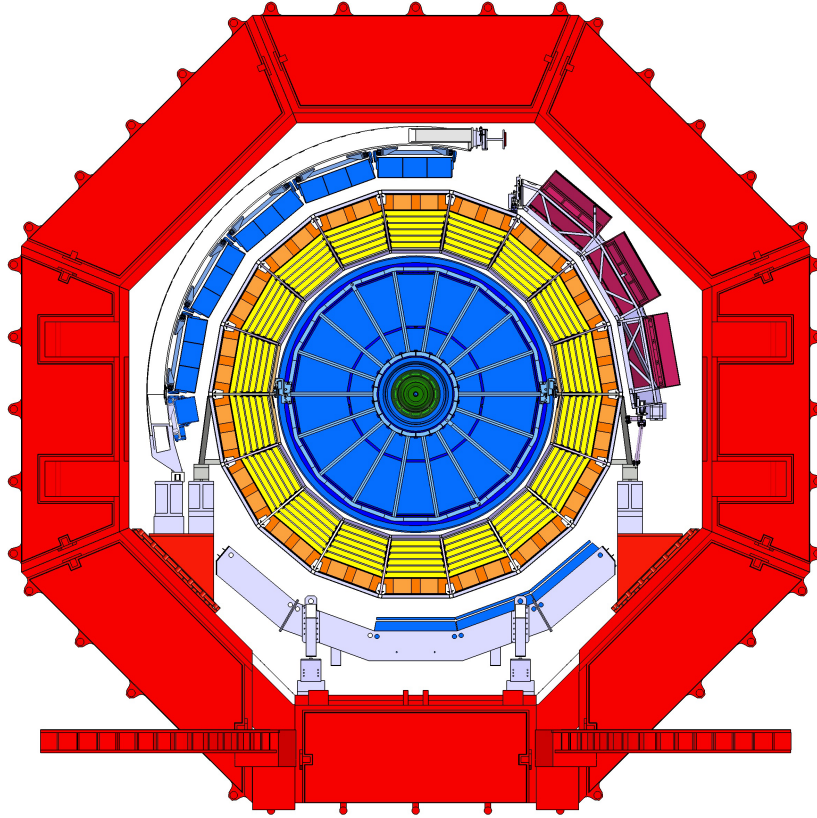
Figure 2.9: A sketch of cross-section of ALICE central barrel from A-side. It has ITS, TPC, TRD and TOF in inner cylinder, two calorimeters and Cherenkov counter in outer

2.5.1 Inner Tracking System (ITS)[29]

As Fig.2.10 shows, the ITS has six silicon detectors for charged particle reconstruction with excellent pointing resolution. The pair of each two layers called Silicon Pixel Detector(SPD), Silicon Drift Detector(SDD) and Silicon Strip Detector(SSD) from IP. The rapidity range of most

outer layer is $|\eta| < 0.9$, and of most inner layer is $|\eta| < 1.75$ for measurements of charged particle multiplicity. In below, we will present results of simulated detector performance using FLUKA with HINJING simulation for Pb-Pb collision.
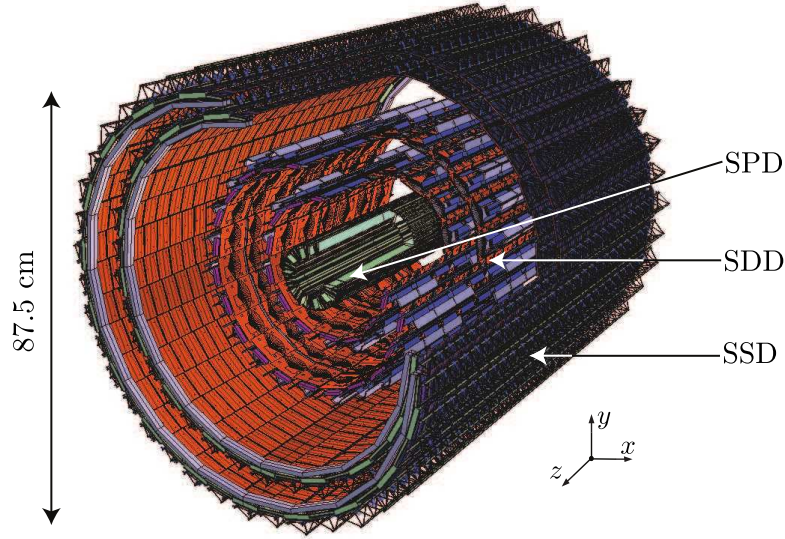
Figure 2.10: A sketch of Inner Tracking System. There are six layer of silicon detectors, it is named SPD, SDD and SSD for each two layers from IP
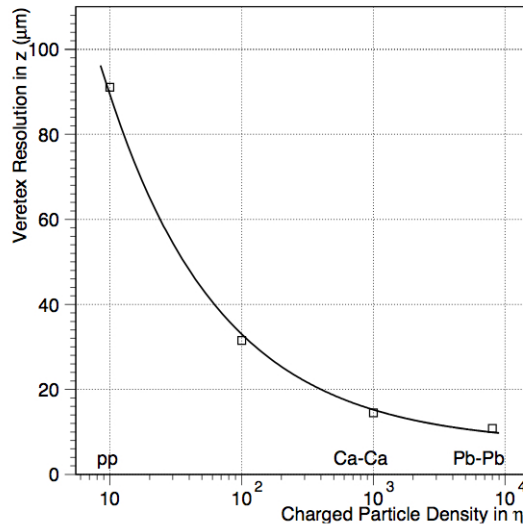
Figure 2.11: Vertrex resolution in z as function of charged particle density in η

The general function of TPC are following.

- reconstruction of the primary vertex and the secondary vertexes for the reconstruction heavy flavor decay.

- low-momentum particle tracking with particle identified

- improvement of the momentum and pointing resolution of the TPC tracking.

The transverse position of LHC bunches under our control, the distribution width is only 15μm. Therefor only we have to take care is reconstruction of longitudinal vertex position, as known issuer, the distribution width (RMS) $\sigma_z \sim 7.5$cm. We can reconstruct primary vertex without track reconstruction. We can assume the position by angle formed by hits.

Fig.2.11 provide us resolution of longitudinal vertex reconstruction as function of charged particle density.As we can see in the figure, we can get collision vertexes with fine resolution.
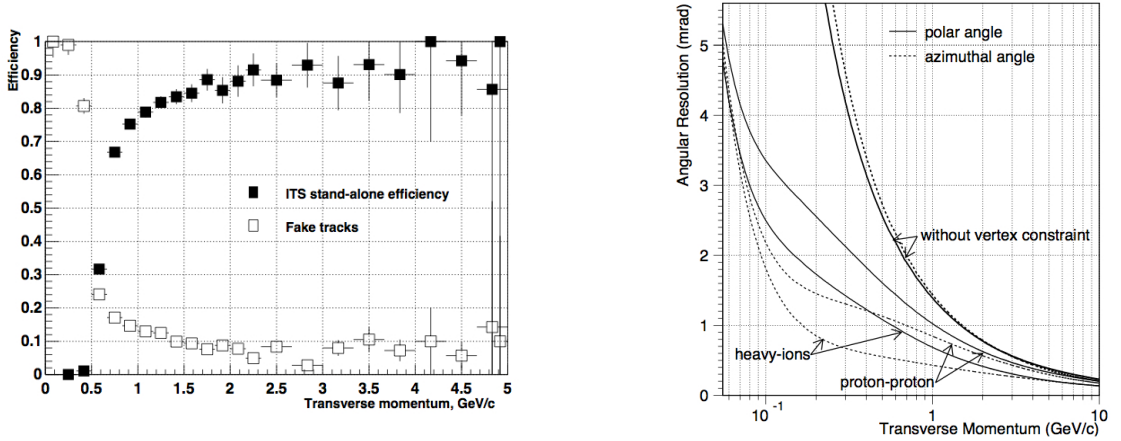
Figure 2.12: Left: ITS stand-alone efficiency and fake track rate as function of transverse momentum. Right: Angular resolution as function of transverse momentum of ITS

In the ALICE experiment, it is used a method based on Kalman filter algorithm as track reconstruction. Fig.2.12 shows tracking efficiency and angular resolution of poler angle and azimuthal angle as function of transverse momentum using only ITS. At 2 GeV/c, we have 90% efficiency with less than 10% fake track ratio and angular resolution is less than 1 mrad.

In high momentum region of track, we have to reconstruct the tracking with large radius. Because it's too difficult to estimate momentum for the track which goes through detectors in a almost linear fashion so that it is difficult to estimate curvature factor for such tracks. For the reason, we need to combine ITS and TPC to reconstruct charged tracks. To make sure performance of tracking with TPC and ITS, we compared the momentum resolution of ITS+TPC reconstruction with TPC stand alone reconstruction. As we can see in Fig.2.13, if we compare thick solid line and thin solid line, thick line is lower than thin in high momentum region. Therefor momentum resolution get better using to sort and refit TPC track to ITS track in high momentum region.
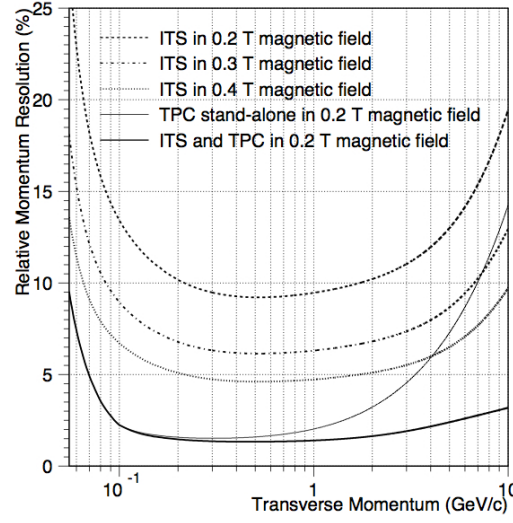
Figure 2.13: Momentum resolution of reconstructed tracks with ITS and TPC

2.5.2   Time Projection Chamber(TPC)[30]

The time projection chamber is one of most important sub-detectors which characterize ALICE experiment. TPC is a type of drift chamber with MWPC for three dimensional charged track reconstruction with fine pointing resolution and less materials . It can detect transverse trajectory as track of induced charge on read pad and longitudinal trajectory as difference of drift time. The tacks reconstruction by TPC is a classical approach, however such huge detector is unprecedented thus far.
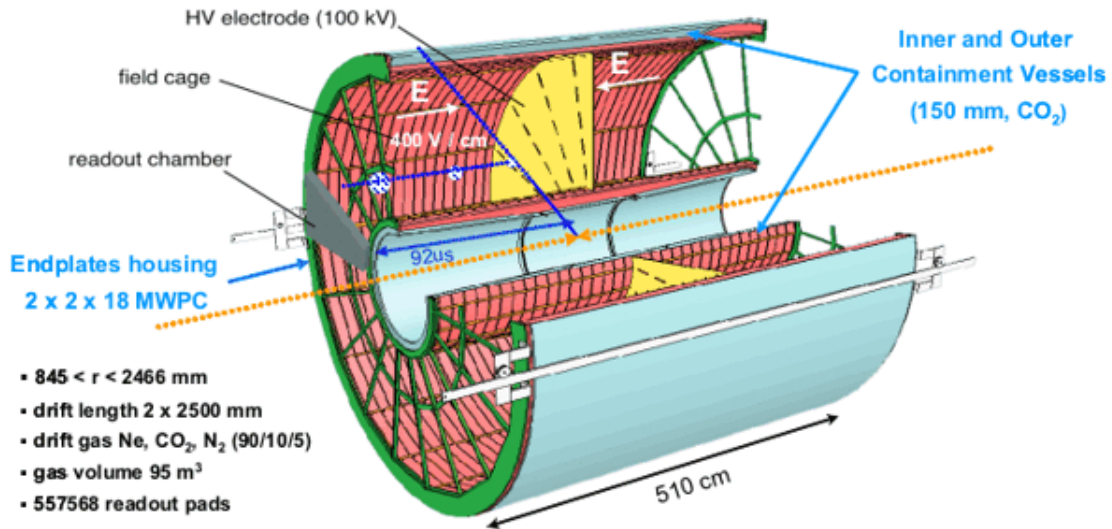
Figure 2.14: A sketch of Time Projection Chamber

TPC is designed cover following requirements at high charged tack multiplicity($dN/d\eta \sim$ 8000)

- nominal drift time ($< 100\mu$s for $Ne/CO_2/N_2(90:10:5)$)

- excellent tracking efficiency ($> 90\%$) and fine track matching to other detectors ($\sim 90\%$)

- fine momentum resolution (5% for 5GeV/c electron, $\sim 1.5\%$ for MIP)

- good particle identify performance (dE/dx $\sim 10\%$)

- signal-to-noise ratio for MIP better than ($\sim 20:1$ for inner, $\sim 30:1$ for outer)

- good two particle separation for correlation measurements(1cm separation $r\phi$ and z direction)

2.5.3 Transition Radiation Detector(TRD)[31]

The TRD provide sufficient electron identification capability for measurements of heavy flavor like as Charm and Beauty. TRD let us can reconstruct leptonic decay from D-meson and B-meson. Transition radiation is produced by relativistic particle when it pass through boundary of two material of different dielectric constants. The emission angle is inversely proportional to Lorentz-factor($\gamma = E/mc^2$), so radiation is emitted almost forward direction of injected particle. It is quite different between Lorentz-factors of electron and pion at same momentum for their particle mass. Therefor TRD can separate electrons from pions using the behavior.The momentum range of that TRD can reject pions from electrons could be 1GeV $\sim$ 100GeV in naive. ALICE have 18 super modules of TRD and 6layer and 5 stack modules for one super module in mid-rapidity.
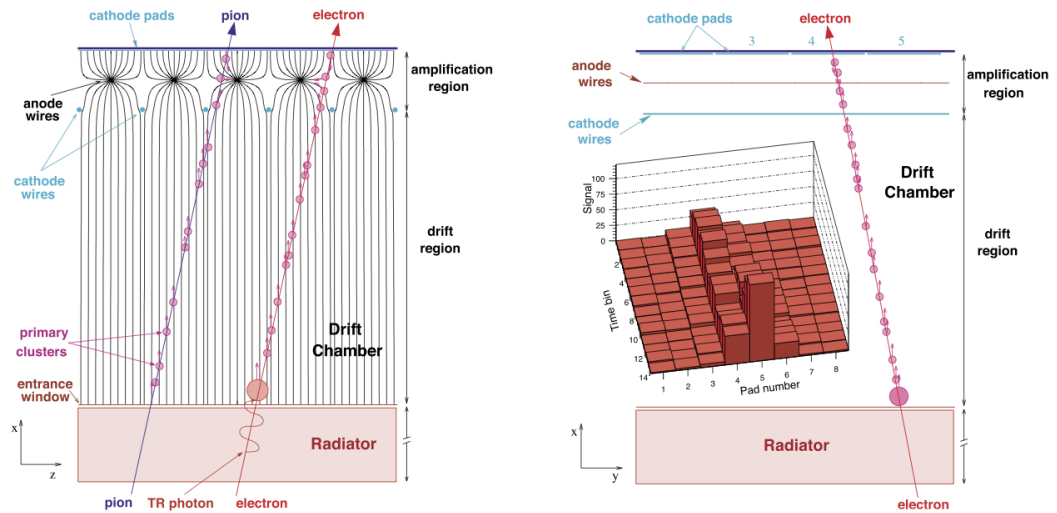
Figure 2.15: Principle of TRD detector, Left : electric field in TRD detector and sketch of electron cluster when pion and electron through the chamber
Right: signal amplitude as function of detection time

Fig.2.15 shows principle of transition radiation detector.As shown by the picture, TRD is composed by simple drift chamber with MWPC and radiator for transition radiation. In left figure,we can see two injected tracks of pion and electron. When electron is crossing TRD, transition radiation is generated at radiator in from t of drift region.Then we will have large energy deposit when transition radiation is absorbed in chamber. In right figure,we can see example pals height as function of drift time.It is important choose drift gas to have high pion rejection factor, we have to choose gas with short absorption length for transition radiation(we choose $Xe/CO_2(85:15)$). If we have such gas we can get high transition radiation efficiency and use drift time to reject pion as shown by right figure of Fig.2.15.
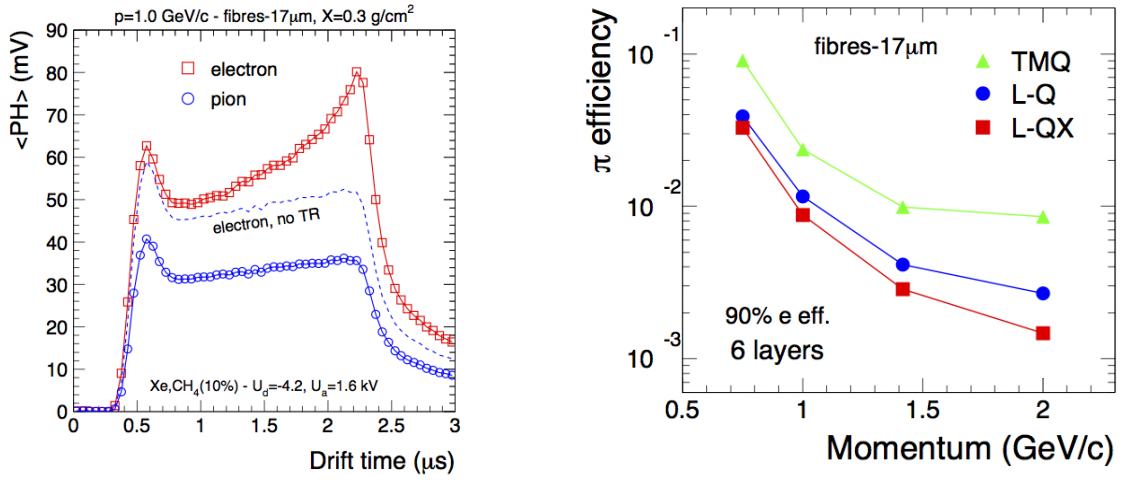
Figure 2.16: Left : Average pulse hight for electron and pion as function of
              drift time
              Right :Pion rejection factor at 90% electron efficiency

Left figure of Fig.2.16 shows mean pulse height as function of drift time for pion and electron.We can see clear peak at large drift time for electron, the peak come from energy deposit from transition radiation. And dashed line shows mean pulse height electron which is measured by same test without radiator. We evaluated pion rejection factor at 90% electron efficiency with 6layers TRD. Right figure of Fig.2.16 provide the result at beam test. We tested three method to evaluate likelihood TMQ,L-Q and L-QX. The mean energy deposit is used to calculate likelihood of TMQ, the total energy is used for L-Q.L-QX use the information of energy deposit and drift time.We have achieve rejection functor ~ 100 over $p_T > 1 GeV/c$ using L-Q and L-QX.

2.5.4   Time Of Flight(TOF)[32]

Time of flight is a methods to identify of charged hadrons,we can know particle mass using the velocity at the same momentum. Basically, hadron mass(m) can be calculated by following relation of their momentum(p) and flight time(t) of distance(L)

$$m^2 = p^2((\frac{t^2}{L^2}) - 1) \tag{2.3}$$

And the resolution of mass reconstruction can be described as following.

$$\left(\frac{\delta m}{m}\right)^2 = \frac{\delta p}{p} + \gamma^4\left(\left(\frac{\delta L}{L}\right)^2 + \left(\frac{\delta t}{t}\right)^2\right) \tag{2.4}$$

In experiment, we have to develop high timing resolution detector for hadron identification using TOF at large γ, so that flight length is fixed. We developed Multi Resistive Plate Chamber (MRPC) as high timing detector.MRPC have sandwich structure of resistive plate and gas layer. We can have high timing resolution with tin gas layer and high efficiency with multi gas layer.

We develop double stack MRPC with 5 layer per a stack which is shown in Fig.2.17.
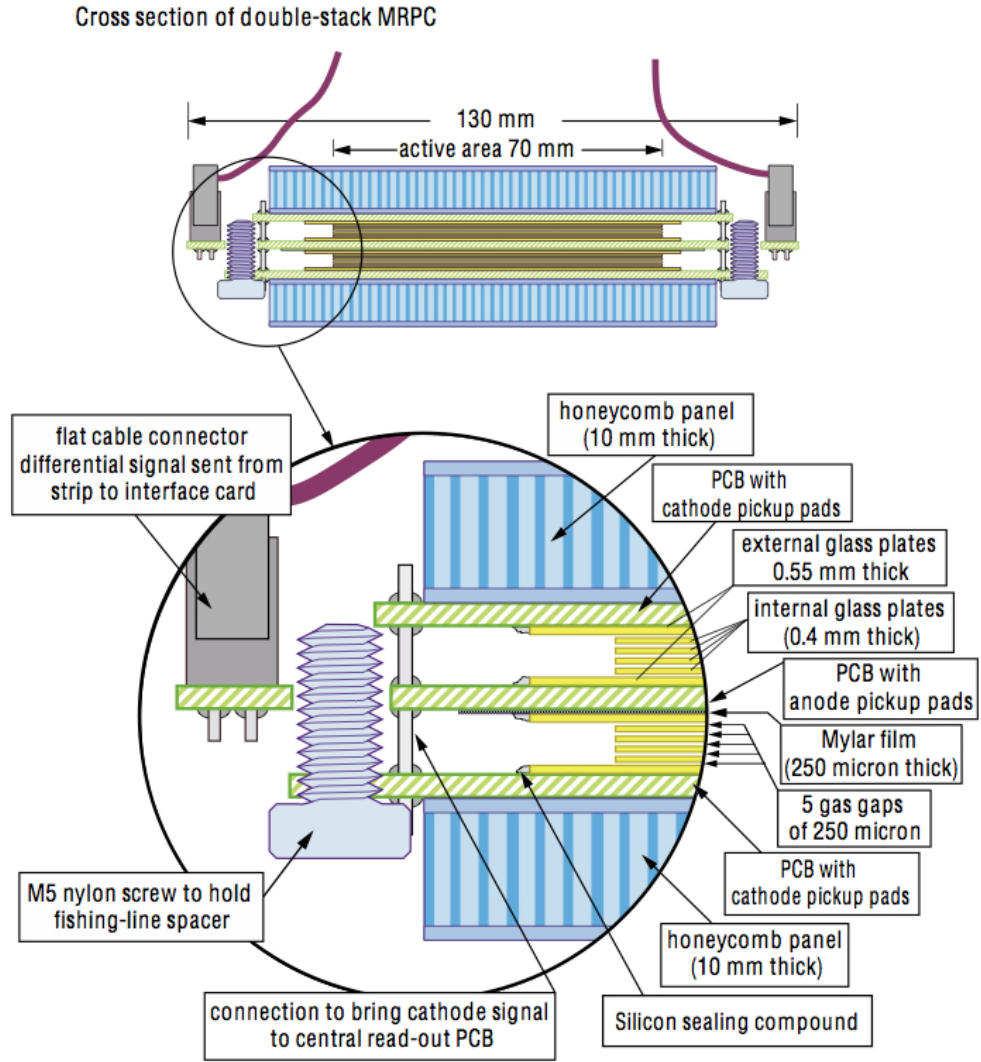
Figure 2.17: Cross section of TOF detector which has 2 stacks with 5 gaps for each stack

Left figure of Fig.2.18 shows the efficiency as a function of the applied electric field in a gap. We observed that the efficiency of the 10 gap(2×5 gap) MRPC is close to 100% and reaches the plateau at lower electric field.And right figure of Fig.2.18 shows the resolution as function

of the electric field. The MRPC for ALICE has excellent timing resolution very close to 40ps to reconstruct particle mass.
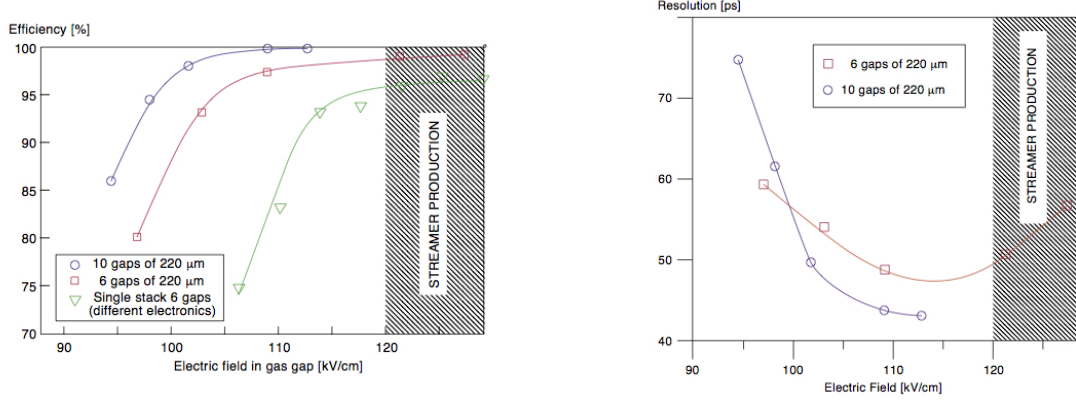
Figure 2.18: Performance of TOF detector, Left : detection efficiency as function of applied electric field, Right : timing resolution as function of electric field for each prototype

2.5.5 Electromagnetic Calorimeter(EMCal)[33]

ALICE detector has two type of electromagnetic calorimeter,one is classical lead-scintillator sampling calorimeter, the other one is lead-tungstate crystal calorimeter. First one is developed to detect electrons and photons with large acceptance for especially high momentum physics. Latter one is built for photon physics but with small acceptance(more detail in latter section).
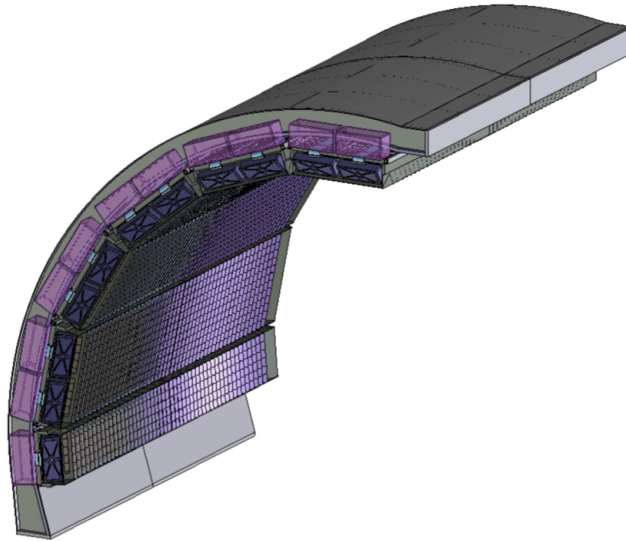
Figure 2.19: The array of super modules of EMCal shown in the installed position on their support structure

Fig.2.19 illustrate overview of full installed EMCal super modules. EMCal cover 110° in azimuthal 1.4 in rapidity. And individual tower acceptances are about 0.014×0.014 at $\eta = 0$.

In general, energy resolution can be given as following

$$\frac{\sigma_E}{E} = \sqrt{(\frac{a}{E})^2 + (\frac{b}{\sqrt{E}})^2 + c^2} \tag{2.5}$$

where b represents the stochastic term,and a represents the system noise in readout channel,and c represents constant term. In low energy and/or intermediate region it is important factor in energy resolution, light yield and collection efficiency. It's also important background hits. For EMCal, it can work in stable therefore it can be ignorable term of b which come from system noise in readout channel.

Fig.2.20 provide the combined results of energy resolution of electron which are measured at PS and SPS in CERN. The dashed carve shows simulated energy resolution by GEANT3. The Modules has fine requested performance.
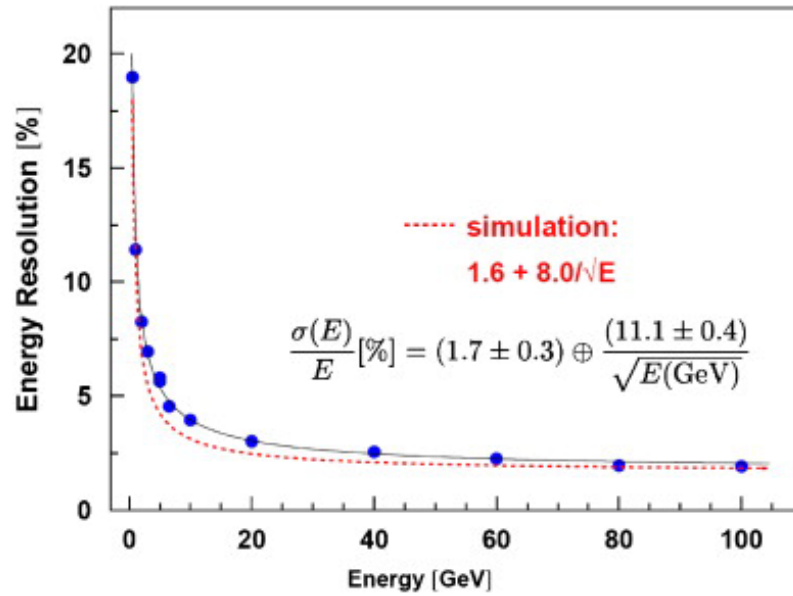
Figure 2.20: Energy resolution of EMCal as function of electron energy and
fitting result by Eq.2.5

From early 2013, additional EMCal called DCal(di-jet callrimeter) in opposite side of EMCal next to PHOS.

2.5.6 PHOton Spectrometer(PHOS)[34]

The PHOS detector was developed to take out initial phase information of collision in particular initial temperature , via direct single photon and di-photon measurements. The PHOS is located 460cm from collision point.The PHOS is a type of electro magnetic calorimeter made by lead-tungstate crystal (PbWO$_4$) with photo diode as readout.

Fig.2.21 shows overview of super modules on installation frame.Which is located 460cm from collision point.The PHOS is a type of electro magnetic calorimeter made by lead-tungstate crystal ($PbWO_4$) with photo diode as readout.
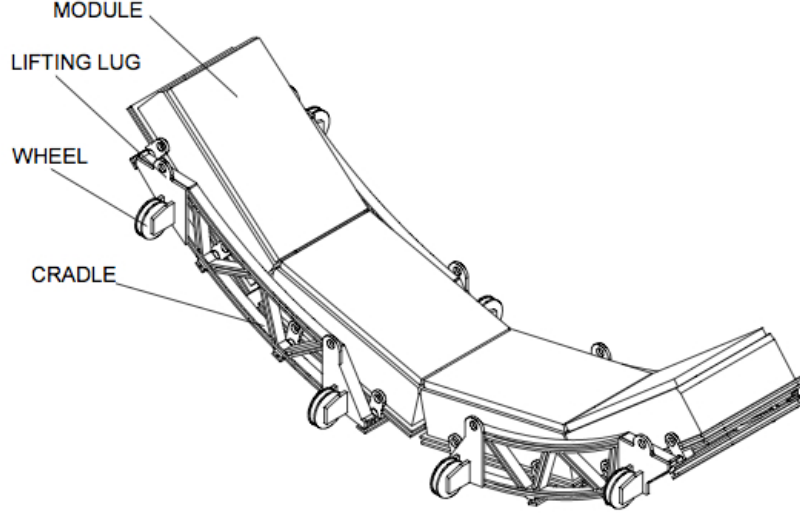
Figure 2.21: A sketch of the configuration of the PHOS calorimeter with
installation arm

Fig.2.22 shows us, energy resolution of electron for each results of beam test in PS and SPS. We have excellent resolution as designed.The PHOS detector is sensitive to electrical noise, so we operate the detector under $-17°C$. And the term of a in fund. Eq.2.5 should be considered.
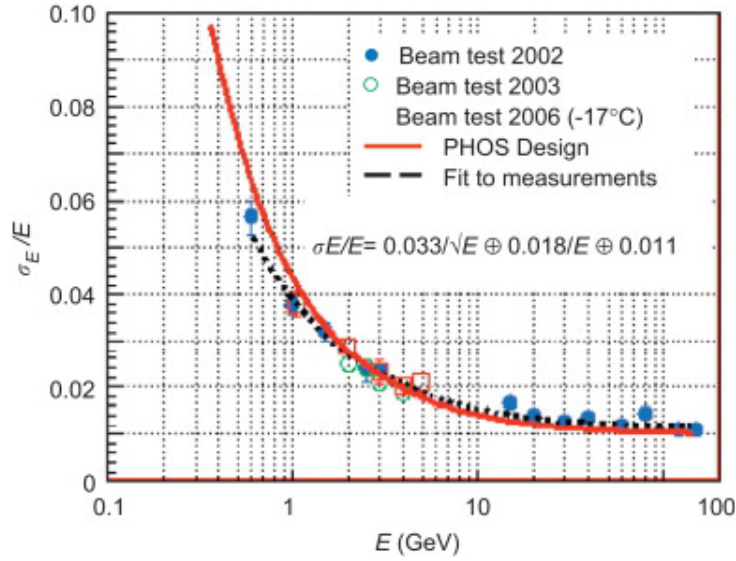
Figure 2.22: Energy resolution of PHOS as function of electron energy and
fitting result by Eq.2.5

2.5.7   High Momentum Particle Identification(HMPID)

The High-Momentum Particle IDentification (HMPID), devoted to the identification of the high-momentum particles. The detector is a type of Ring Imaging Cherenkov Counter(RICH) which is designed as MWPC with C_6F_{14} radiator. The HMPID in ALICE can identify pions and kaons in the momentum range 1 to 3 GeV/c with separation power 3σ and it can also identify protons in the range 1 to 5 GeV/c with 3σ separation. The detector will let us be able to have knowledge in fragmentation function in jet.

2.6   Forward Detectors

2.6.1   Forward Multiplicity Detector(FMD)[27]

The FMD was built to study multiplicity fluctuation in forward rapidity on an event-by event basis. The number of segment of FMD is larger compared with other forward detectors with large acceptance and with large η gaps from mid-rapidity. Therefor FMD is suitable to measure multiplicity independently to see the correlation of multiplicity in mid-rapidity. The FMD also can reconstruct event plane with fine resolution by benefit of it has many segment in ϕ direction.

2.6.2   Photon Multiplicity Detector(PMD)[36]

We have several physics goals with PMD via measurements of inclusive photon. The first goal of PMD is getting the signal of Disoriented chiral condensate(DCC) using the correlation between charged particles and inclusive photons through the measurements of N_γ/N_{ch} ratio with full azimuthal coverage. And we might have some signal of critical phenomena near the phase boundary leading to fluctuations in global observables like multiplicity, mean transverse momentum and pseudorapidity distributions.And SPD can measure inclusive photon flow and estimate event plane by photon.

2.6.3   Forward Muon Spectrometer[37]

The forward muon spectrometer is built as combined components of detector,absorber and dipole magnet. The Muon Spectrometer is developed for the measurements of quarkonia behavior via $\mu^+\mu^-$. At RHIC it is observed suppression of vector meson production like as J/Ψ. It is considered the suppression come from Debye screening of color charges. The forward muon spectrometer allow us to study such physics concerning quarkonia which contain heavy flavors.

Chapter 3

Data Reduction

In this chapter we describe details of the analysis approach to measure azimuthal correlation between jets and particles. At first, we present the event trigger information for the analysis. Latter of that we describe event characterization of the events in Pb-Pb collision by the centrality and the event plane. Then we present how to reconstruct track of the charged particles and the reconstruct jets, and subtract the backgrounds from jet momentum. At the end it is described the method of jet-particle correlation.

3.1 Minimum Bias Event Trigger

In this analysis, we only use the minimum bias events of both pp and Pb-Pb collisions. Ideally, the minimum bias trigger of ALICE provide fine efficiency for both of the low multiplicity events and the diffractive events with fine beam backgrounds(beam-gas and beam-halo interaction) rejection. In ALICE experiment, the signals from the three detectors are used to define the minimum bias trigger, VZERO(V0), SPD and ZDC. It is called V0A for V0 at A-side and V0C at the C-side.

VZERO

The merits to use VZERO detector for the event trigger are that VZERO is stable detector in the high magnetic fields with the radiation tolerance and VZERO has large acceptance in forward rapidity and it can provide fast signal to trigger events. Therefore VZERO is used as online trigger detector in the forward rapidity. To have good background event rejection, we can use timing information of VZERO detector. We can predict approximate arrival time to get signal from collision by location of detectors from the interaction point(IP). The time should be 11.3 ns for V0A(3.4 m from IP) and 3.0 ns for V0C(90 cm from IP). By cutting out events using timing cut of VZERO signal, ALICE get events with fine efficiency with fine background rejection.

SPD

To get the signal to triggered events in the mid-rapidity, we require at least one hit for each layers of SPD which is two layers of pixel detector located inner most ITS (called Fast-OR signal). To reduce backgrounds, we define the acceptable range of secondly hit as that first hit should be on

diagonal line between IP and secondly hit. Then if we got secondly hit in proper range we call the signal Global Fast-OR signal.

ZDC

In Pb-Pb collisions, spectator which is nucleons did not join collision pass through along beam pipe. We can assume the position of that the point spectator passing through. We put calorimeter on the point to detect the spectator. We also can assume the arrival time of nucleons to ZDC. We apply timing cut of ZDC for minimum bias events in Pb-Pb collisions on offline.

3.1.1 proton-proton collision

We require the signal of either V0 signal (V0A or V0C) or SPD signal (Global Fast-OR) as minimum bias trigger like as following.

$$\text{MB : (GLOBAL} - \text{FO} \cup \text{VZERO} - \text{OR)} \cap \overline{\text{BKG}} \tag{3.1}$$

We can get 99.9% efficiency for the non-diffractive event and 79.9% for the diffractive event, totally 93.6% of all the inelastic events. For the backgrounds we get 7.7% efficiency of the beam-gas events and 2.3% efficiency of the beam-halo events with the trigger configuration. Then we cut out the event which event has reconstructed primary vertex point of z-direction over than 10 cm from expected point in offline analysis. In this analysis, 63 million minimum bias events are analyzed for $\sqrt{s} = 2.76$ TeV and 313 million events are analyzed for 7 TeV.

3.1.2 Pb-Pb collision

To trigger minimum bias events in Pb-Pb collisions, we use the same trigger configuration class of pp collisions online, to have fine trigger purity we applied ZDC timing cut additionally in offline analysis. In this analysis, 19 million minimum bias events are analyzed.

3.2 Centrality

As we discussed at Sec1.2.1, Pb-Pb events are characterized by the collision geometry. In experiment we can assume the collision geometry connecting the centrality with number of particles using a Monte Carlo Glauber model. The model assumes that the number of independently decaying precursor particles(ancestors) is given by $N_{\text{ancestors}} = \alpha \times N_{\text{coll}} + (1 - \alpha) \times N_{\text{part}}$, where α quantifies their relative contributions.

Then we assume that every ancestors emits particles according to a Negative Binomial Distribution(NBD)

$$P_n(\kappa) = \frac{\Gamma(n + \kappa)}{\kappa(n - 1)\kappa(\kappa)} \left(\frac{\mu/\kappa}{1 + \mu/\kappa}\right)^n \frac{1}{(1 + \mu/\kappa)^\kappa}, \tag{3.2}$$

where the parameter μ is the mean multiplicity per precursor, and κ defines the width of the NBD and therefore controls the fluctuations to large multiplicity. We estimate the centrality using calibrated VZERO amplitude, so that it can let we have fine centrality resolution in the all centrality range. The resolution is 0.5% in the central and 2% in the peripheral.

Fig.3.1 shows VZERO calibrated amplitude distribution with the centrality bins which is fitted by Glauber Model estimation. As far as we see the figure, we have fine centrality estimation which is expected by Glauber model.
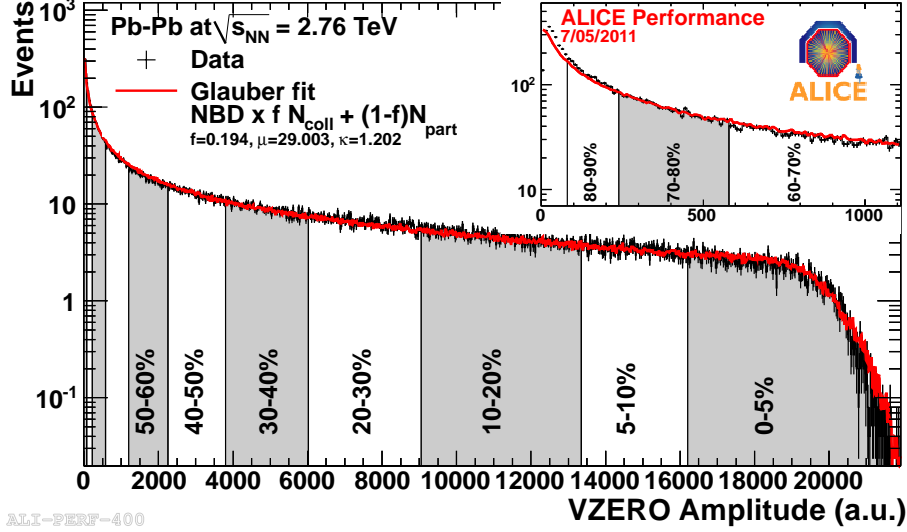
Figure 3.1: VZERO amplitude distribution for centrality determination

3.3   Event Plane

In Sec.1.4.3, we explained anisotropic flow with respect to the event plane. So we can determine the event plane from the spacial anisotropy of particle distribution. It is better to use the detector in forward rapidity with large acceptance to reduce non-flow effects (like as jet and resonance decay) when we determine the event plane for each events.

Experimentally , we can calculate the event plane according to Eq.3.3. Q_x and Q_y is the projection of the event plane to x and y axes respectively. Then we choose multiplication of total multiplicity and charge ratio of the cell with respect to the total charge of VZERO detector.

3.3.1   Re-centering Calibration

Width of Q vector of x, y axis Q_x and Q_y become wider with the increasing the centrality percentile. Then we can correct Q vectors with respected to width of Q_x and Q_y distribution. Re-centering correction is defined as following,

$$2\Psi^{corr} = \tan^{-1}(\frac{Q_y^{corr}}{Q_x^{corr}}), \tag{3.3}$$

$$Q_x^{corr} = \frac{Q_x - <Q_x>}{\sigma_x}, \tag{3.4}$$

$$Q_y^{corr} = \frac{Q_y - <Q_y>}{\sigma_y}. \tag{3.5}$$

The width of Q vectors are extracted by RMS of Q vectors distribution.

3.3.2 Event Plane Resolution

In the real experiment, only finite number of particles are emitted and detected in each collisions. This introduces some fluctuations in observing the anisotropy on an event-by- event basis. Even if the distribution is azimuthally anisotropic, statistical fluctuations can lead to non-zero coefficients v_n. In high energy nuclear collisions, we usually define resolution of the event plane to correction anisotropic flow as following,

$$\sigma_{\text{plane}_{v_n}} = < \cos(n(\Psi_{\text{measured}} - \Psi_{\text{true}})) > . \tag{3.6}$$

If measured plane at A-side and C-side is very close, we can assume the event plane as follows,

$$
\begin{aligned}
&<\cos(n(\Psi_{\text{measured}} - \Psi_{\text{true}}))> \\
&= \quad <\cos(n(\Psi_A - \Psi_{\text{true}}))> \\
&\sim \quad \sqrt{<\cos(n(\Psi_A - \Psi_{\text{true}}))><\cos(n(\Psi_C - \Psi_{\text{true}}))>} \\
&\sim \quad \sqrt{<\cos(n(\Psi_A - \Psi_{\text{true}}))><\cos(n(\Psi_C - \Psi_{\text{true}}))> + <\sin(n(\Psi_A - \Psi_{\text{true}}))><\sin(n(\Psi_C - \Psi_{\text{true}}))>} \\
&= \quad <\cos(n(\Psi_A - \Psi) - (\Psi_C - \Psi))> = <\cos(n(\Psi_A - \Psi_C))>.
\end{aligned}
\tag{3.7}
$$
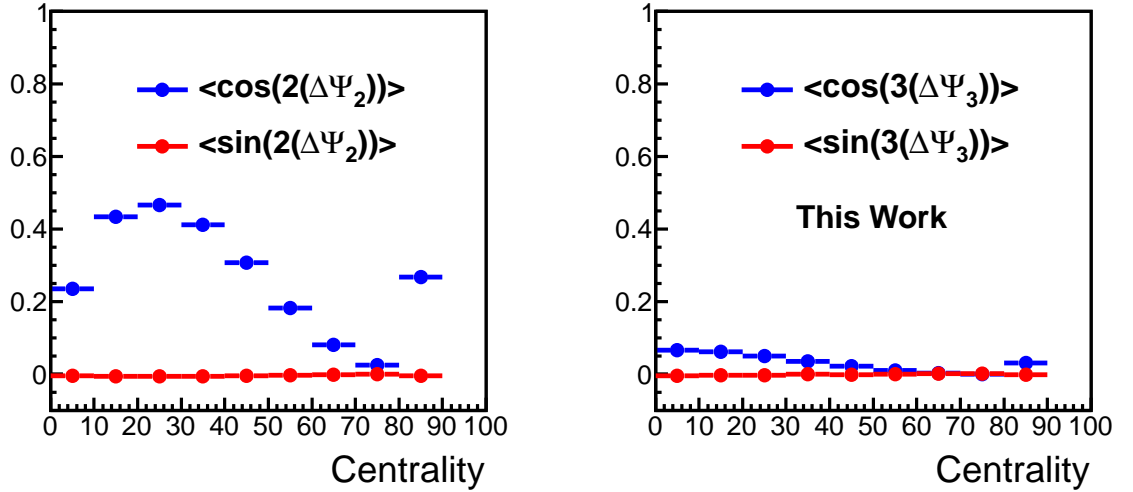
Figure 3.2: Left : Event plane resolution of 2nd order, Right : Event plane resolution of 3rd order

Fig.3.2 shows the event plane resolution of 2nd and 3rd order. Average $\sin(n(\Psi_A - \Psi_C))$ is close to zero. That means approximation in Eq.3.7 is natural. For 2nd order, in the central collisions, the anisotropy of the collision geometry is small, so the event plane resolution also small. And in the peripheral collisions, the event plane resolution also small so that particles for estimation the event plane is limited. For 3rd order, fraction of 3rd order flow is still high. That is why the resolution of 3rd plane in the central is high compared with the over centrality.

3.4 Global Track Reconstruction

In this analysis, we use tracks reconstructed by ITS and TPC with the momentum range 0.15 GeV/c $< p_T$ (the upper limit of the momentum range is limited as 80GeV/c automatically because we only use jets their momentum smaller than 80GeV/c) in $|\eta| < 0.9$ within 0.5 T solenoidal magnetic field. We use three tracking classes to reconstruct the primary charged particles. So that ITS has non-uniform efficiency in ϕ and η space, because of the problem of SPD(innermost layer of ITS) cooling during the runs which we analyze in this measurements. The first tracking class accepted the tracks which is reconstructed by TPC and has hit on one of the two layer of SPD. The second tracking class don't require SPD hit but require the primary vertex instead of the SPD hit as a point of reconstructed track. And The third class require the primary vertex but don't re-fit track of TPC to ITS track.

Detail of track cuts are following.
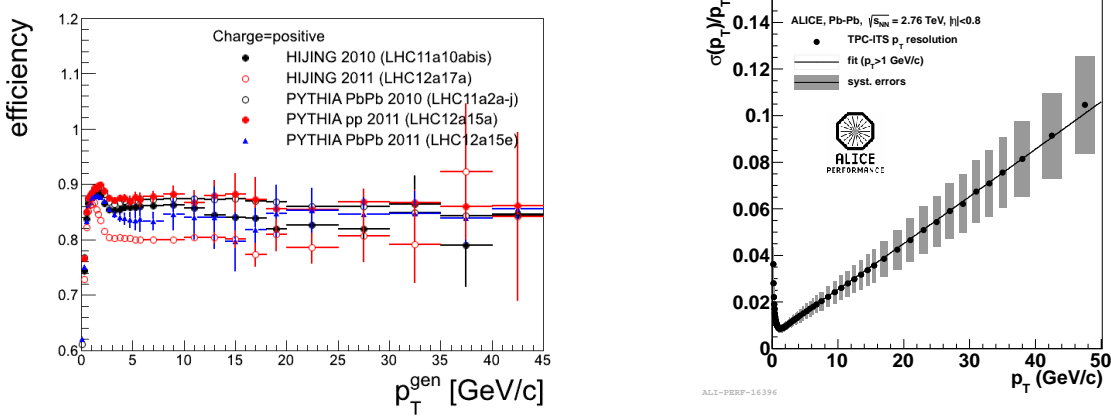
Figure 3.3: Left:Efficiency of global track as a function of p_T for each Monte Carlo configuration LHC11a2a-j is anchored to pp collisions at $\sqrt{s} = 2.76$ TeV and LHC11a10 is anchored to Pb-Pb collisions at $\sqrt{s} = 2.76$ TeV

Right:Momentum resolution of global track as a function of p_T in Pb-Pb collisions at $\sqrt{s} = 2.76$ TeV

- TPC cluster should be over than 70.

- Maximum χ^2 per TPC cluster is 4.

- TPC stand alone tracking required at first iteration of tracking.

- Required refit to ITS from second iteration.

- No identified kink is required.

- χ^2 per ITS cluster smaller than 36.

- It should contain a hit on SPD otherwise primary vertex can be used instead of SPD hit.

- Maximum distance of closest approach to vertex in longitudinal direction is 3.2 and in transverse direction 2.4 cm.

- Do not require sigma cut to vertex

The left figure of Fig.3.3 shows the track reconstruction efficiency of the setup. LHC11a2a-j is anchored to pp collisions at $\sqrt{s} = 2.76$ TeV and LHC11a10 is anchored to Pb-Pb collisions at $\sqrt{s} = 2.76$ TeV. According to the efficiency measurements using Monte Carlo events, we have about 85% in pp collisions, 80% in Pb-Pb collisions at 40 GeV/c . The right figure of Fig.3.3 shows momentum resolution of tracks in Pb-Pb collisions. We can reconstruct global tracks with the resolution less than 10% at 40 GeV/c.

3.5 Jet Finding Algorithm

To find out jets, we have two type of algorithms to reconstruct jet energy(momentum) and axis in general way. First one is cone type algorithm. This way is a classical approach to find jets and it was used from a few decades ago for example at UA1 experiment. The basic idea of the algorithms is sum up all particles in fixed radius from the trigger particle(highest momentum particle is a natural choice) in $\eta \times \phi$ space. However we had known the methods are not infrared safe at the some order in the perturbation theory in previous research [38].

These days we usually use the sequential clustering algorithm which is latter one of the two instead of cone type algorithm. In this analysis we use anti-k$_T$ algorithm[39] in FASTJET package[40] for jet reconstruction. The procedure of jet reconstruction by anti-k$_T$ algorithm is follows.

1. Calculate weighted distance of all particles pair(i, j) given by

$$d_{ij} = min(\frac{1}{p_{Ti}^2}, \frac{1}{p_{Tj}^2})\Delta R_{ij}^2/R^2, \tag{3.8}$$

$$\Delta R_{ij}^2 = (\eta_i - \eta_j)^2 + (\phi_i - \phi_j)^2, \tag{3.9}$$

   where p_{Ti} is transverse momentum of particle i and R is jet-radius parameter.

2. Calculate distance between the beam and particle i : $d_{iB} = 1/p_{Ti}$

3. Compare d_{ij} and d_{iB}, if d_{ij} is smaller, merge particle i and j into a single particle. If d_{iB} is smaller, clustering is finished.

4. If the cluster pass the filter, we call cluster "jet". In ALICE experiment we have momentum threshold and jet area as filter.

5. Resume for the left particles 1 to 3 until no particles are left.

In this measurements, we required only charged tracks for jet reconstruction. We call the jet "charged jet" when we would like to distinguish from jet, reconstructed by charged and neutral particles (called "full jet" in the case). The parameters for charged jet reconstruction are following.

Table 3.1: FASTJET parameters

Parameter	Value
Algorithm	anti-k_T
$R(= \sqrt{\Delta\phi^2 + \Delta\eta^2})$	0.4
Strategy	Best
Recombination Scheme	Boost Invariant p_T
Ghost Area	0.01
Active Area Repeats	1
Ghost η maximum	0.9
p_T input particle	$p_T > 0.15$ GeV/c
Jet p_T threshold	$p_T^{jet} > 10$ GeV/c
Jet acceptance	$|\eta| < 0.5$
Jet area	$\text{Area}^{jet} > 0.4$

The momentum distribution of the reconstructed jet are shown in the left figure of Fig.3.4. We can see the yield of the leading jet and the inclusive jet almost overlapped. That means almost jets were reconstructed as the leading jet in each event. And the right figure of Fig.3.4 shows the reconstruction efficiency and the axis resolution of the reconstructed leading jet with respect to the generated leading jet which pass jet reconstruction with not only charged particles but also neutral particles.
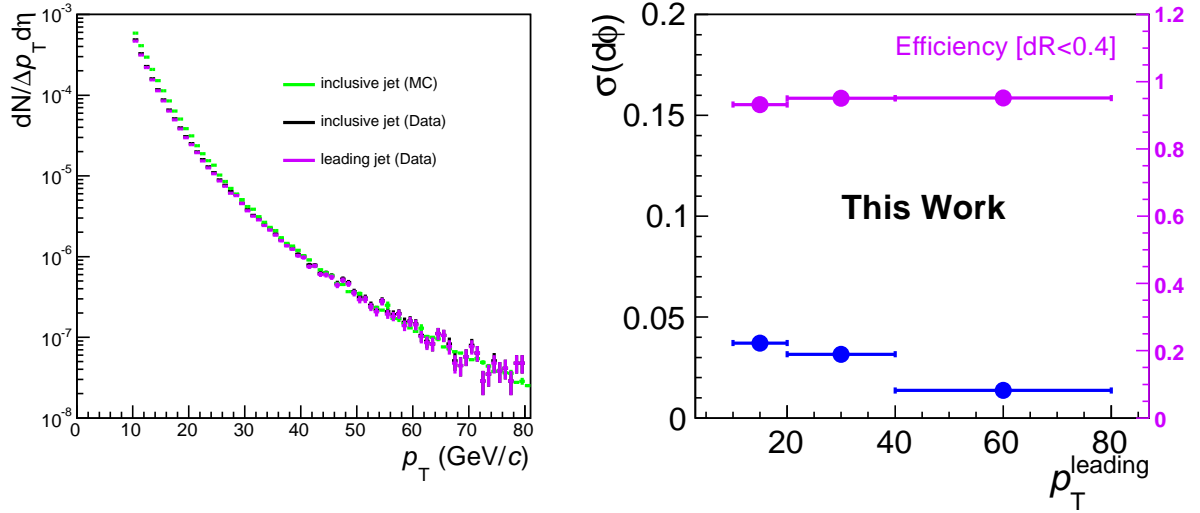
Figure 3.4: Left : Momentum distribution of reconstructed inclusive jet and
leading jet in pp collisions at $\sqrt{s} = 7$ TeV
Right : Jet reconstruction efficiency with matching parameter
$\Delta R < 0.4$ and reconstructed axis resolution with respect to generated jet

According to the results, we can reconstruct the leading jet axis with excellent resolution. In the analysis the leading jet axis will be used as the trigger axis, so the leading jet axis reconstruction resolution is one of most important performances. The reconstruction efficiency is also good. The efficiency is more than 90% where the momentum region we analyzed for the jet-particle correlation measurements.

3.6 Back Ground Subtraction

In heavy ion collisions, we have huge number of particles from thermal bulk. We already mentioned at Sec1.4.3, the azimuthal particle distribution is not uniform with respect to the event plane, so that bulk expansion is not only from radial expansion but also anisotropic expansion so called elliptic flow and triangular flow. These kind of effects are shown up as particle emission intensity v_2 and v_3 in the particle azimuthal distribution. For jet measurements, such huge number of particles should contribute as background and we have to take into account distribution of particle anisotropy in background estimation.
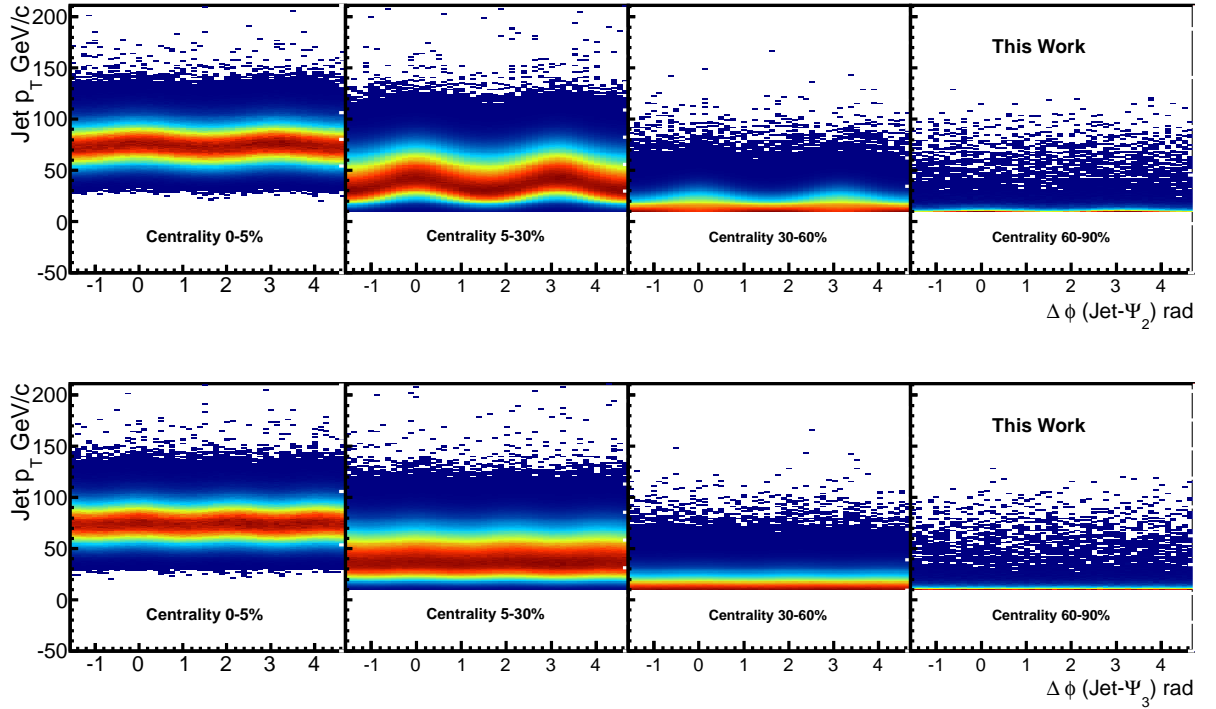
Figure 3.5: Top : Reconstructed jet momentum distribution as a function of jet axis with respect to Ψ_2 in heavy ion collisions
Bottom : Reconstructed jet momentum distribution as a function of jet axis with respect to Ψ_3 in heavy ion collisions

Fig.3.5 shows the momentum distribution of the reconstructed jets as a function of the jet azimuthal axis with respect to the event plane(Ψ_2) and the triangular plane(Ψ_3) in the four centrality bins. The jet momentum looks biased not only by the centrality but also the event

planes of second order and third order. The dependence of second order looks strong in the mid-central region compared with in the most central that effects come from the flow stronger in the mid-central due to the anisotropy of the collision geometry. The jet momentum also depends on Ψ_3 however the quantities are smaller then the quantities of second order.

We need to remove the background energy from the reconstructed jets energy in heavy ion collisions. The momentum density of particles which is generated by thermal bulk in ϕ - η space can be given by

$$\frac{dp_T^{\text{BKGtotal}}(\phi,\eta)}{d\phi d\eta} = \frac{dp_T^{\text{flat}}(\phi,\eta)}{d\phi d\eta} + \frac{dp_T^{\text{elliptic}}(\phi,\psi_2,\eta)}{d\phi d\eta} + \frac{dp_T^{\text{triangular}}(\phi,\psi_3,\eta)}{d\phi d\eta} + \cdots \qquad (3.10)$$

$$p_T^{\text{elliptic}}(\phi,\psi_2,\eta) = \sum p_T \times v_2 \times \cos(2(\phi - \psi_2)) \qquad (3.11)$$

$$p_T^{\text{triangular}}(\phi,\psi_3,\eta) = \sum p_T \times v_3 \times \cos(3(\phi - \psi_3)) \qquad (3.12)$$

where p_T^{elliptic} describe particle momentum weighted v_2 and $p_T^{\text{triangular}}$ also means momentum which come from triangular flow. The acceptance of ALICE detector in the mid-rapidity is sufficiently smaller than beam rapidity. Experimentally we can almost ignore η dependence of the momentum distribution.

In general, we can calculate the amount of the background momentum which is under area in $\phi - \eta$ space as following.

$$p_T^{\text{BKG}} = \text{Area} \times \frac{dp_T^{\text{BKGtotal}}(\eta,\phi)}{d\phi d\eta} \qquad (3.13)$$

3.6.1   Subtraction Method

In this analysis, we calculate the background momentum density event by event then subtract the background for each jets. The procedure of the background subtraction in jet reconstruction is following. Fig3.6 is conceptual diagram to follow up the procedure to subtract backgrounds from jets.

1. Fill all particles into two dimensional histogram in $\phi - \eta$ plane with their p_T.

2. Reconstruct jets with no background subtraction.

3. Fit function $[f = \text{A} + \text{B}\cos(2(\phi - \psi_2)) + \text{C}\cos(3(\phi - \psi_3))]$ to 2D histogram to get momentum density.

4. Subtract background momentum from reconstructed jets momentum according to Eq.3.13.

5. Correct bin value in $\Delta\text{R}(\text{bin} - \text{jet}) < 0.5$ to be average value of ϕ direction if corrected $p_T^{\text{jet}} > 3$ GeV/c.

6. Fit again to get correct background momentum density.

7. Subtract momentum from jet momentum.
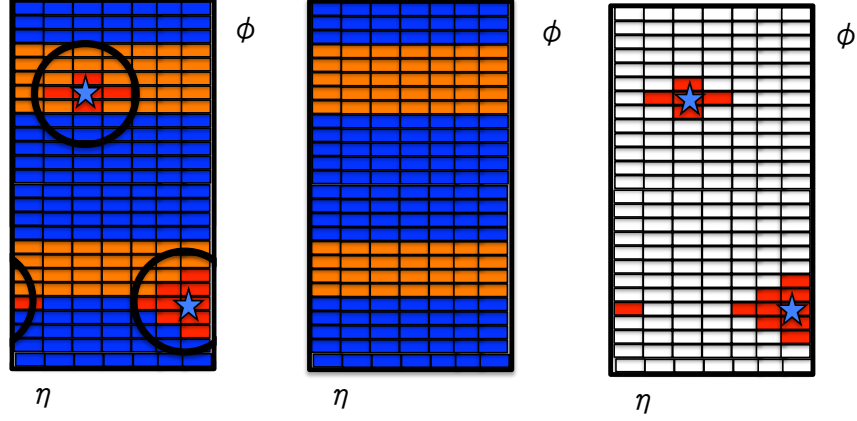
Figure 3.6: Momentum distribution in η-ϕ plane,

Left : Reconstructed jet axis with jet area ($\Delta R < 0.5$) (1-5)

Center : Jet removed distribution(6)

Right : Background subtracted distribution(7)
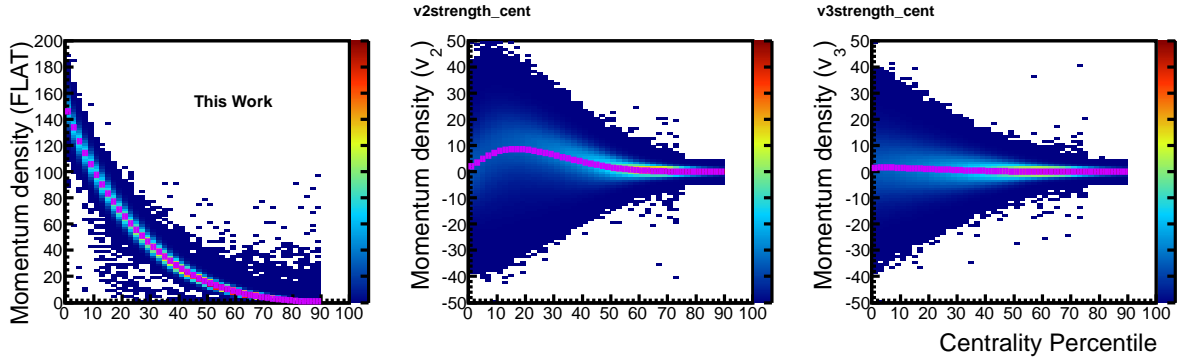
Figure 3.7: Background momentum density for each components as a function of centrality and their average,

Left : constant background,

Center : 2nd order background ,

Right : 3rd order background

The background momentum density which is estimated by fitting to 2D histogram of the momentum distribution in η-ϕ plane are shown in Fig.3.7. The flat component of the background density is strongly depends on centrality as we see in left figure on Fig.3.7. However the other distributions are fluctuated because the fluctuation of flow is large and we have finite resolution to estimate the event plane. In event by event, the event plane can be reconstructed transverse direction of the ideal reaction plane. In the most central region, the amplitude of fluctuation of 3rd order as large as 2nd order that means, it is mixed that the elliptic flow dominant event and the triangular flow dominant event in the central collisions.

The momentum distribution of the background-subtracted jets as a function of jet axis with respected to the event plane and the triangular plane are upper figures on Fig.3.8 and bottom. We get almost uniform distribution with respected to the event plane and the triangular plane. However we still have dependence of the event plane in the mid-central and the mid-peripheral which is shown on second and third figure from left on upper Fig.3.8. Mainly this dependence seems to come from two effects. One is pass length dependence of jet modification, we describe the dependence in Sec.1.4.5. If the picture is correct, there should have difference of jet energy scale between the reconstructed jet axis in the in-plane and the out-plane. That can be the origin of dependence we see in Fig.3.8. Another effect can come from the event plane dependence of the background momentum fluctuation.
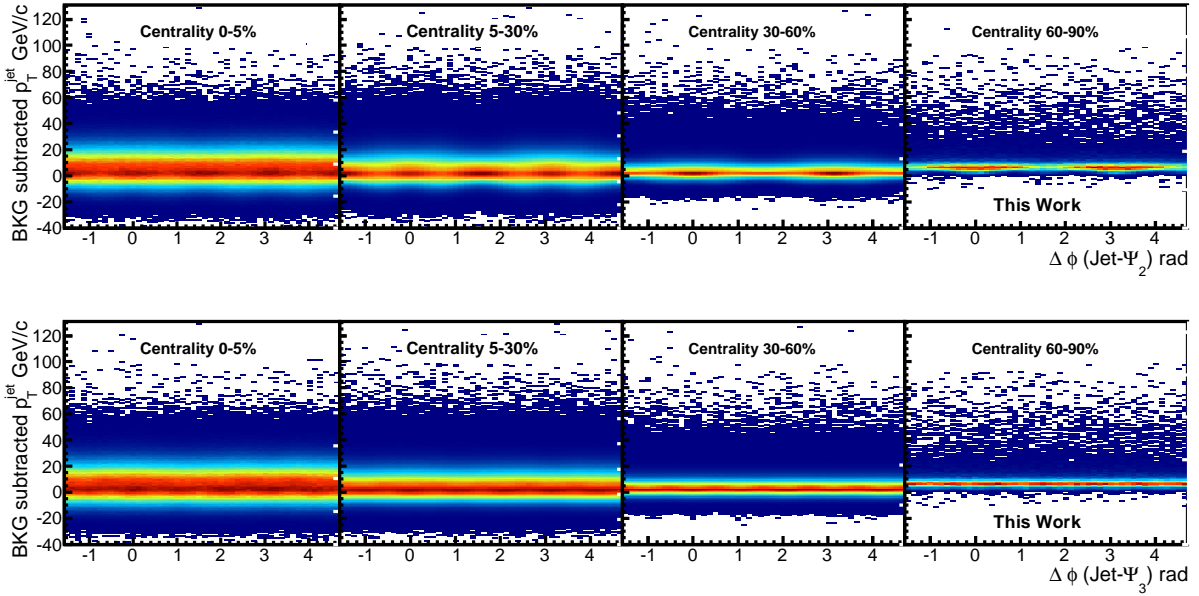
Figure 3.8: Momentum distribution of background subtracted jets as a func-
             tion of jet axis with respect to event planes for each centrality
             bins,
             Top : Momentum distribution with respect to Ψ_2,
             Bottom : Momentum distribution with respect to Ψ_3

Fig.3.9 shows the momentum distribution of the background subtracted jets which is divided into four centrality bins. The top four figures are the momentum distribution of jets which is subtracted flat background only. The bottom four figures are the momentum distribution of jets which is subtracted not only flat background but also backgrounds come from elliptic flow and triangular flow. In the distribution on the top figures, it is subtracted flat background including the event fluctuation of flat background. Averages of the distributions of the in-plane in all centrality are higher than averages of the out-plane. As we see in Fig.3.5, jet momentum is depending on emitting angle with respect to the event plane. On the other hands, in lower figures, the differences of the in-plane and the out-plane are smaller than the difference in the top figures. That means, back ground effects of elliptic flow and triangular flow is minimized by the

background subtraction of the analysis. As we had already seen in Fig.3.8 angular dependence with respect to the event plane is still in momentum distributions of background subtracted jet especially in the mid-central and the mid-peripheral collisions. It is compatible that the dependence come from the pass length dependence of jet modification.
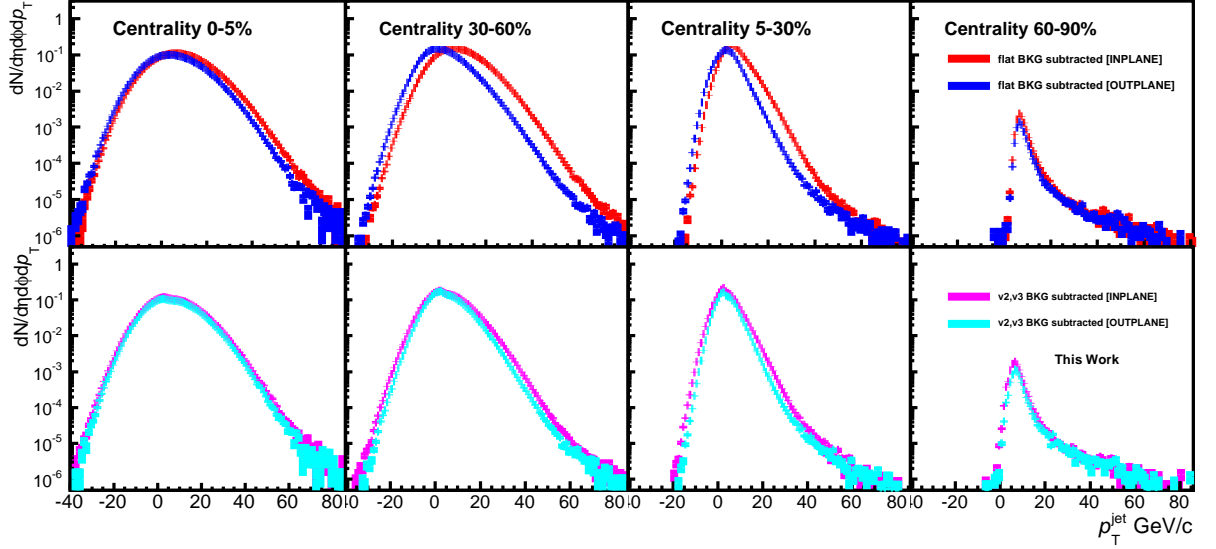
Figure 3.9: Momentum distribution of background subtracted jets divided into two jet angular class with respect to event plane for each centrality, Top : jet momentum which is flat background subtracted. Bottom : jet momentum which is flat,elliptic and triangular background subtracted.

3.6.2 Subtraction Performance

To check performance of the background subtraction method, and to get the knowledge of the origin of the event plane dependence in the background subtracted jet momentum, we test the background subtraction for PYTHIA di-jet events embedding to Pb-Pb events.

Fig.3.10 shows the average of the background density in ϕ and η space for each term of Pb-Pb collisions and PYTHIA di-jet embedded Pb-Pb events. The difference of non di-jet embedded sample and di-jet embedded sample is small in all term of the background momentum density, flat, v_2 and v_3. That means the background subtraction method has in-sensitivity against di-jet sample, that also means the method is stable.

In the case of Fig.3.10, it is not considered interaction between jets and hot/dense matter. If there are such effects, it is possible to jets bias strength of backgrounds. Therefore we also checked momentum dependence of triggered jet in the background momentum distribution.

The momentum density for each term as a function of the centrality is shown in Fig.3.11. The left figure of Fig.3.11 shows the momentum density of the flat background term. In central collisions, black line is between blue and red, that means background of minimum bias is described
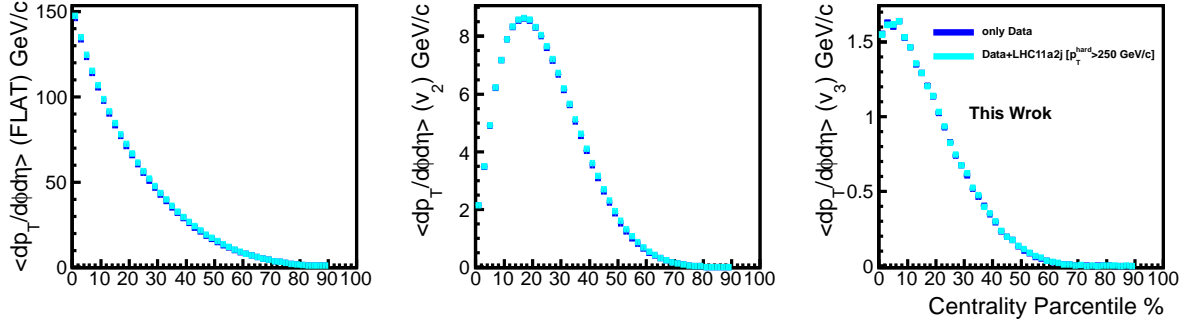
Figure 3.10: Average background momentum density as a function cen-
trality in Pb-Pb collisions and PYTHIA di-jet embedded Pb-
Pb events .Blue line shows the mean value of background for
events without any di-jet sample and Cyan shows the results
in $250 < p_T^{\mathrm{hard}}$GeV/c
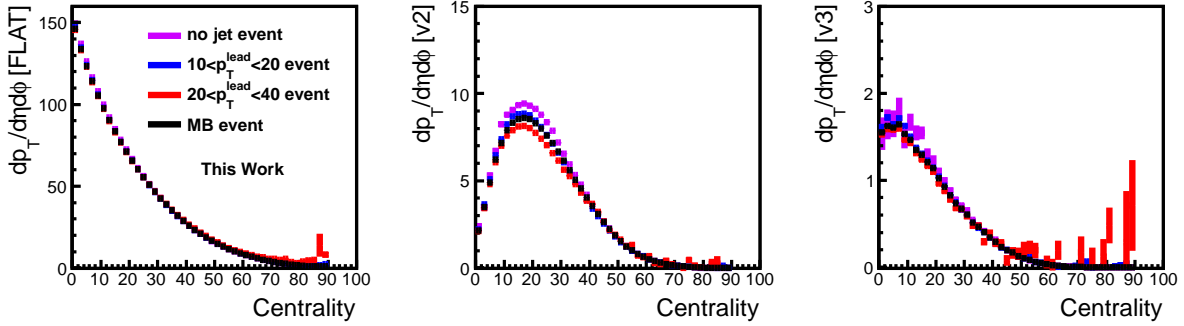
Figure 3.11: Left : Average background momentum of flat term as a func-
tion of centrality for each leading jet momentum. Center :
Average background momentum of v_2 term as a function of
centrality for each leading jet momentum. Right : Average
background momentum of v_3 term as a function of centrality
for each leading jet momentum.

as events between the event has jet in $10 < p_T < 20$ GeV/c and in $20 < p_T < 40$ GeV/c. That
also means the background momentum has dependence of the leading jet momentum. It might
comes from bias of trigger events. If we triggered high momentum jets, the energy density of
the QGP of the events lower than the events which has no jets. In natural understanding, the
high momentum jets can be triggered with less jet modification. On the other hands, in the
peripheral, the flat background with high momentum jets is higher than the other. It might
come from the effects of the momentum of triggered jets dependence in underlying events[41].

In the center figure and the right figure of Fig.3.11, black line also is in between red and blue. That also mans, v_2 and v_3 are affected by jets. Still unknown why jets affects v_2 and v_3, it might comes from that the high momentum particles are re-distributed into production of the low momentum particles. In the average background of PYTHIA embedded data, embedded particles are in $|\eta| < 0.9$. Therefore embedded charged particles can not affect to event plane estimation so that acceptance of VZERO detectors are out of range $|\eta| < 0.9$. The difference in Fig.3.10 and Fig.3.11, can bias jet momentum. In latter measurements the differences are considered as systematic uncertainty.

To check performance of the background subtraction, we have to compare properties of embedded PYTHIA jet with reconstructed jet in huge background. In this analysis, we choose axis difference as matching parameter of PYTHIA jet with the reconstructed jet. Fig.3.12 shows azimuthal axis difference as a function of embedded leading jet momentum for each centrality. We can see the clear peak around $\Delta\phi = 0$ that means the method is able to reconstruct the leading jet axis correctly. We also see border peak in the away side of the embedded leading jet axis, if the embedded di-jet momentum is balanced the leading jet reconstructed as the sub-leading jet, the sub-leading jet also can be swapped during reconstruction procedure. And we see uncorrelated distribution with respect to the embedded leading jet, that come from jets which is contained in data. If data has higher momentum of jets compared with momentum of embedded di-jet sample, jet contained in data should reconstruct as the leading jet instead of the embedded leading jet.
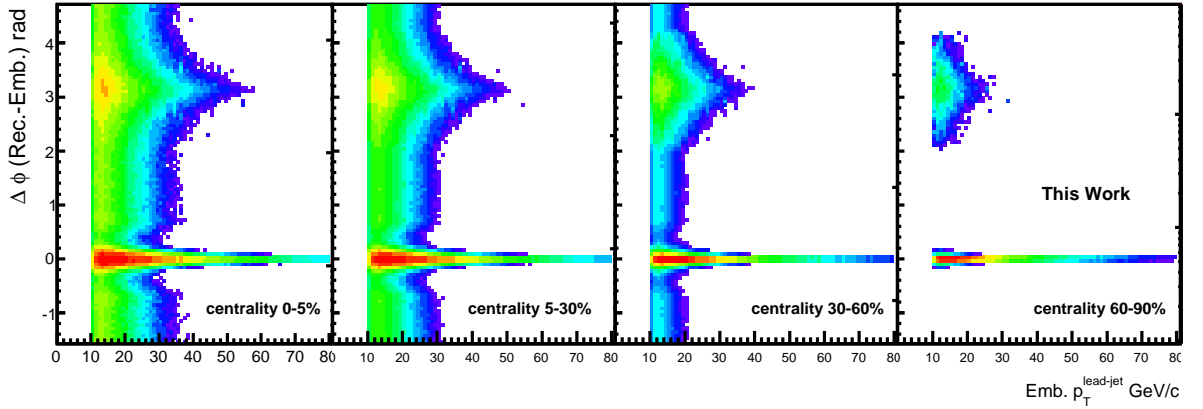
Figure 3.12: Axis difference between reconstruct leading jet and embedded leading jet as a function of transverse momentum of leading jet $p_T^{\text{lead}-\text{jet}}$ for each centrality bins

The left figure of Fig.3.13 shows the matching efficiency of the reconstructed jets with respect to the embedded jets as a function of the momentum of the leading jet of embedded di-jet sample for each centrality. The matching efficiency is decreasing with centrality. The reason is data of central collisions has a large number of jets due to multi nucleon collisions then most central collision has many uncorrelated jet with embedded di-jet sample. That is why the matching

efficiency decrease with centrality.

For the analysis we choose dR=0.3 as axis matching parameter. The matching parameter is smaller than cone radius to reconstruct jet. That is why fake jet is rejected from the matched jet samples by definition. But we still have the combinatorial jets.

The right figure of Fig.3.13 shows the momentum distribution of reconstructed PYTHIA jet in Pb-Pb events which is matched jet axis with the embedded jet axis. Black line shows the distribution of embedded PYTHIA and the other color shows the distribution of matched jet for each centrality. In the low momentum region, the yield is decreasing with the centrality. The reason is in the region matching efficiency is small as shown left figure. In contrast, the yield is enhanced in the high momentum region. It is considered that the low momentum of the reconstructed jets is increase due to background, then the yield increased by contribution of low momentum jet.
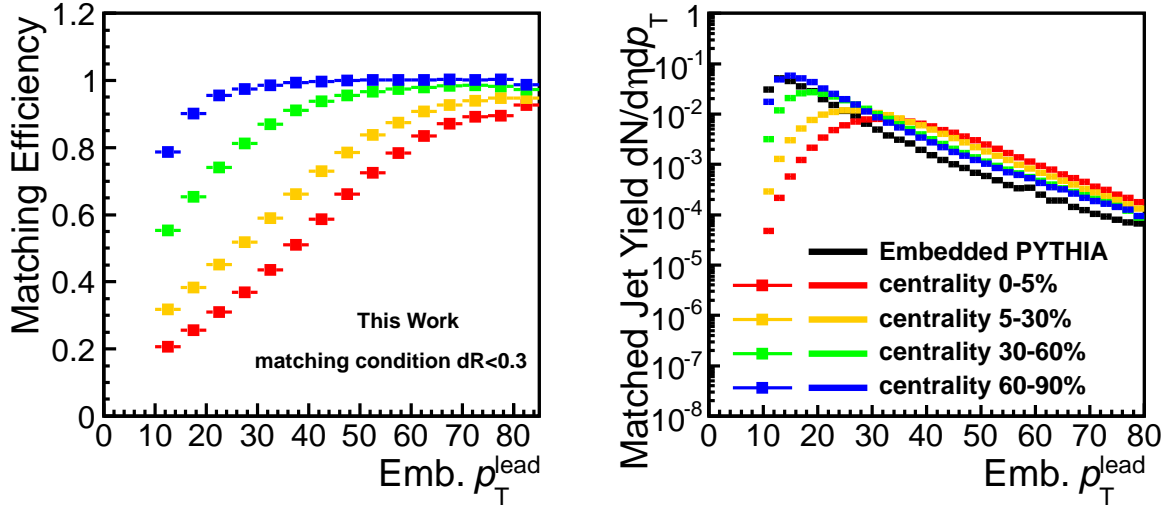
Figure 3.13: Left : Matching efficiency of reconstructed jets with respect
to embedded jets as a function of momentum of leading jet
of embedded di-jet sample for each centrality, Right : momen-
tum distribution of reconstructed PYTHIA jet in Pb-Pb events
which is matched jet axis with embedded jet axis.

The momentum correlation of the embedded and the reconstructed leading jet pair is shown in Fig.3.14. Black line show average value of scattered plot and violet line gives us balanced momentum line. In the peripheral collision which is shown in the first right figure, the pair has strong correlation. On the other hands, the jet momentum scale and the resolution of the reconstructed momentum are smeared by huge background fluctuation. As we see in the bottom figures, black line is higher than violet dashed line in the low momentum region of embedded jet. That means the reconstructed jet momentum is larger than embedded jet momentum in the low momentum region of the embedded jet. The dependence comes from the contribution

of combinatorial jets which is merged with background jets effects and predominant in the low embedded jet momentum region. Due to the effects, the yield of reconstructed jets in huge background particles is enhanced as shown right figure of Fig.3.13.
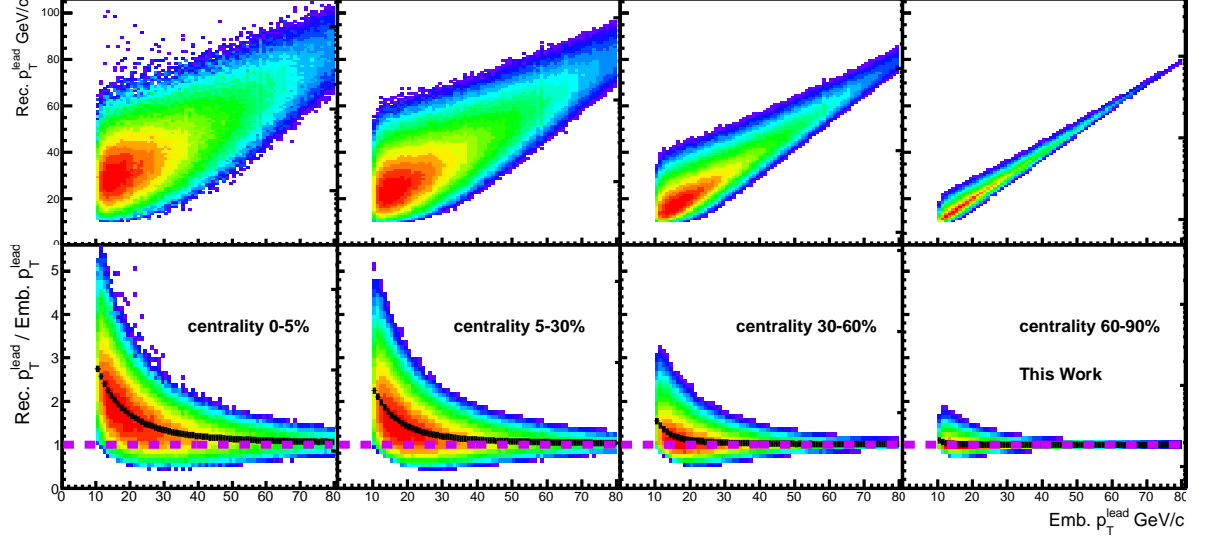
Figure 3.14: Momentum correlation of reconstructed leading jet and embedded leading jet after background subtraction, Top : momentum correlation of reconstructed jet and embedded jet, Bottom : Momentum ratio of reconstructed jet with respect to embedded jet.

3.7 Di-Jet Event Reconstruction

As we mentioned in Sec1.5.2, the missed energy of the sub-leading side looks re-distributed to out of jet cone with large angle. It is also interesting in the modification seeing the effects in the away-side. To see the modification effects clearly we trigger di-jet event for both events of pp collisions and Pb-Pb collisions.

The di-jet selection condition is following.

1. $p_T^{\text{leading}} > 10\text{GeV/c}$.

2. $p_T^{\text{sub−leading}} > 10\text{GeV/c}$.

3. $\cos(\phi^{\text{leadin}} - \phi^{\text{sub−leading}}) < -0.5$.

Fig.3.15 shows the momentum distribution of the leading jet and the leading jet in di-jet triggered events and di-jet trigger ratio as a function of the leading jet momentum in pp collisions at $\sqrt{s} = 7$ TeV. Di-jet trigger ratio is depending on the leading jet transverse momentum which is shown right figure in Fig3.15. In high momentum range, $20 \sim 30\%$ of the leading jet reconstructed
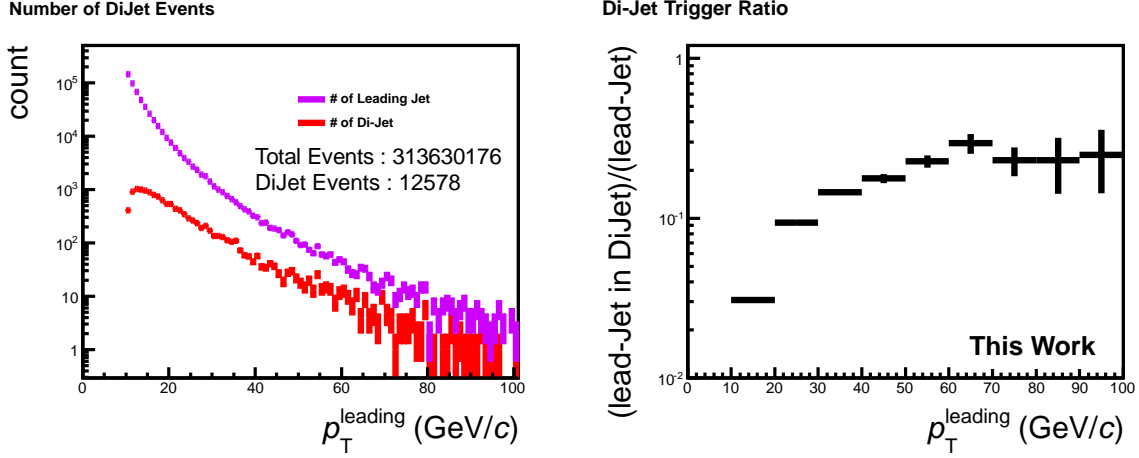
Figure 3.15: Left : momentum distribution of leading jet and leading jet in
triggered di-jet event in pp collisions at $\sqrt{s} = 7$ TeV
Right : Di-jet trigger event ratio as a function of transverse
momentum of leading jet

events are triggered as di-jet event. At $\sqrt{s} = 2.76$ TeV, it has same dependence of the events at $\sqrt{s} = 7$ TeV.
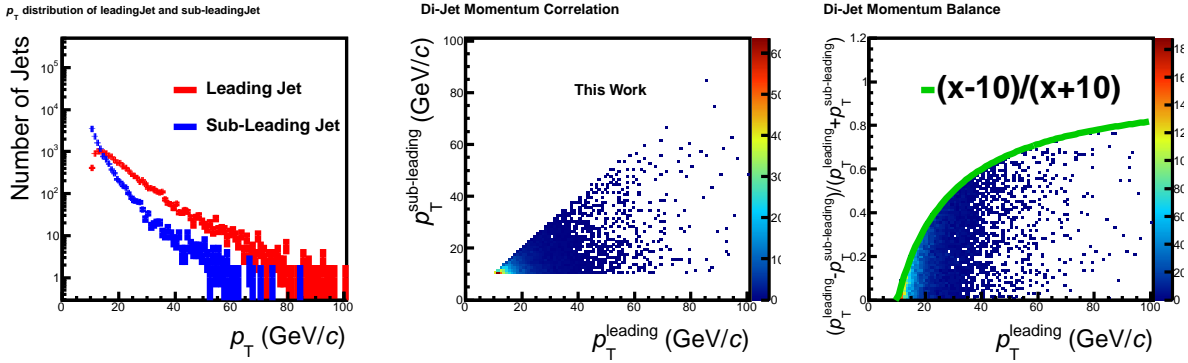
Figure 3.16: Triggered di-jet property in pp collisions at $\sqrt{s} = 7$ TeV, Left
: transverse momentum distribution of leading jet and sub-
leading jet, Center : momentum correlation of leading jet and
sub-leading jet, Right : di-jet momentum asymmetry $A_j = (p_T^{\text{sub-lead}} - p_T^{\text{lead}})/(p_T^{\text{sub-lead}} + p_T^{\text{lead}})$

In Fig.3.16, we can see triggered di-jet properties in pp at $\sqrt{s} = 7$ TeV. The momentum asymmetry of the di-jet is provided right in Fig.3.16. The figure indicate, the di-jet momentum asymmetry is limited by threshold of the sub-leading jets because green line is on the edge of scattered plot. The green line suppose the case momentum of sub-leading jet is just on threshold

for di-jet selection.
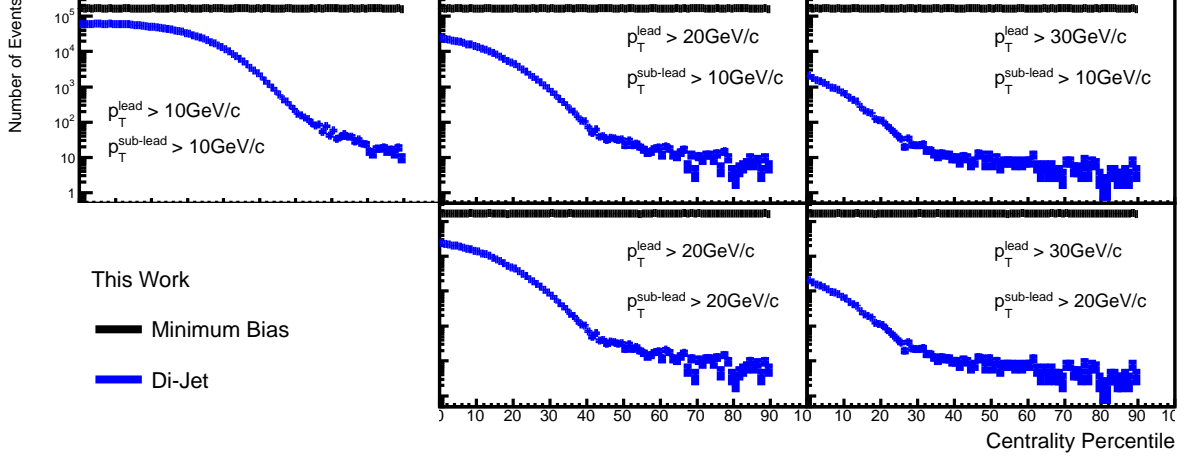
Figure 3.17: Number of trigger events of minimum bias event and di-jet event as a function of centrality, for several momentum threshold of di-jet trigger

The number of di-jet production should be strongly related to the number of nucleon collisions. Therefore the number of di-jet trigger is related to the centrality . Fig.3.17 shows the number of minimum bias trigger events and the number of event which has di-jet pair. We can find large number of di-jet events in central compared with peripheral so that the number of collisions is large in the central collisions. If we apply higher momentum threshold to select the di-jet event, the number of triggered events are reduced, however slope looks smooth compared with the low momentum threshold. That indicates amount of jet momentum modification is large and/or fake jet rate is higher in the central collisions.

To check the purity of the di-jet event, we checked the number of di-jet events as a function of the centrality and the number of collisions. The left figure of Fig.3.18 shows the number of jet per event as a a function of centrality for each jet momentum range. The number of jets is calculated by integrated of the momentum distribution of jets which are background subtracted. The 2nd left figure of Fig.3.18 shows number of jets and di-jets in momentum range $10 < p_T < 20$ GeV/c as a function of number of nucleon-nucleon collisions N_{col}. N_{col} is estimated by fitting by the Glauber a function. The Glauber a function is characterized by NBD $\times f \times N_{\mathrm{col}} + (1 - f) \times N_{\mathrm{part}}$. where NBD a function given by Eq.3.2 and $f = 0.194$ which is given by the fitting shown in Fig.3.1. The 2nd right figure of Fig.3.18 shows the number of jets and di-jets in the momentum range $20 < p_T < 40$ GeV/c as a function of N_{col}. The right figure of Fig.3.18 shows the number of jets and di-jets in the momentum range $40 < p_T < 80$ GeV/c as a function of N_{col}.

In the right figure and the 2nd right figure, di-jet yield lower than single jet yield in for each N_{col} range. Single jet yield is rapidly increase with N_{col} on the other hands, di-jet yield is proportional to N_{col}. However, in the low momentum range, single jet yield and di-jet yield is higher in the mid-central and the mid-peripheral compared with the most-central as we seen in the high momentum range. The trend can be understood elliptic flow makes fake di-jet pair.
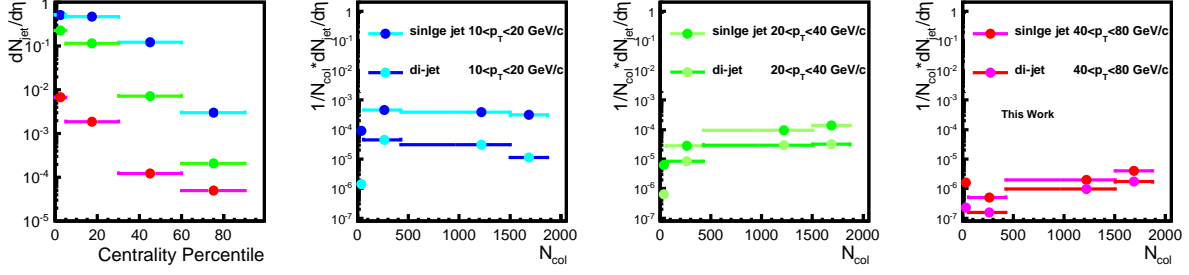
Figure 3.18: Left : Number of jets in a event as a function of centrality. 2nd
Left : number of jets in $10 < p_T < 20$ GeV/c and di-jets in
$10 < p_T^{\text{lead}} < 20$ GeV/c as a function of number of collision N_{col}
estimated by Glauber model. 2nd Right : number of jets in
$20 < p_T < 40$ GeV/c and di-jets in $20 < p_T^{\text{lead}} < 40$ GeV/c as a
function of N_{col}. Right : number of jets in $40 < p_T < 80$ GeV/c
and di-jets in $40 < p_T^{\text{lead}} < 80$ GeV/c as a function of N_{col}.

3.8   Jet Particle Correlation

Let we consider the jet-particle correlation measurements. In this analysis we describe the mo-
mentum weighted $\Delta\phi$ distribution of the associate charged particles with respect to the triggered
leading jet axis in di-jet event as shown Eq.3.14 for pp collisions and Eq.3.15 for Pb-Pb collisions,

$$
\left. \frac{d(\sum p_T^{\text{asso}}(\Delta\phi))}{dn^{\text{dijet}}} \right|_{p_T^{\min}<p_T^{\text{lead}}<p_T^{\max}}
$$
$$
= \left. \frac{d(Eff \times (\sum p_T^{\text{hard}}(\Delta\phi) + \sum p_T^{\text{contami}}(\Delta\phi)))}{dn^{\text{dijet}}} \right|_{p_T^{\min}<p_T^{\text{lead}}<p_T^{\max}}, \tag{3.14}
$$

$$
\left. \frac{d(\sum p_T^{\text{asso}}(\Delta\phi))}{dn^{\text{dijet}}} \right|_{p_T^{\min}<p_T^{\text{lead}}<p_T^{\max}}
$$
$$
= \left. \frac{d(Eff \times (\sum p_T^{\text{hard}}(\Delta\phi) + \sum p_T^{\text{BKG}}(\Delta\phi)))}{dn^{\text{dijet}}} \right|_{p_T^{\min}<p_T^{\text{lead}}<p_T^{\max}}, \tag{3.15}
$$

$$
\sum p_T^{\text{BKG}}(\Delta\phi) = \sum p_T^{\text{contami}}(\Delta\phi) + \sum p_T^{\text{BKG}^{\text{hard}}}(\Delta\phi) + \sum p_T^{\text{BKG}^{\text{soft}}}(\Delta\phi). \tag{3.16}
$$

where $\sum p_T^{\text{asso}}$ is the total momentum of the associate particles in a bin, $\Delta\phi$ is angle difference
between particle and the leading jet, n^{dijet} is number of di-jet triggered event in the momentum
range of the reconstructed leading jet $p_T^{\min} < p_T^{\text{lead}} < p_T^{\max}$ for normalization. The right hand of
Eq.3.14 and Eq.3.15 shows detail of the left hands. The momentum is decreased by the detector
efficiency. And the total momentum include the momentum from non-physical charged particles
like as electrons via γ conversion or Dalitz decay as contamination. In addition, the background

momentum can be contained in momentum from the particles from thermal bulk and/or the particles come from fake jet or combinatorial jet in Pb-Pb collisions.

A jet-particle azimuthal correlation is shown in Fig.3.19 as an example. Mainly we can get five information of di-jet event from the figure as follows.
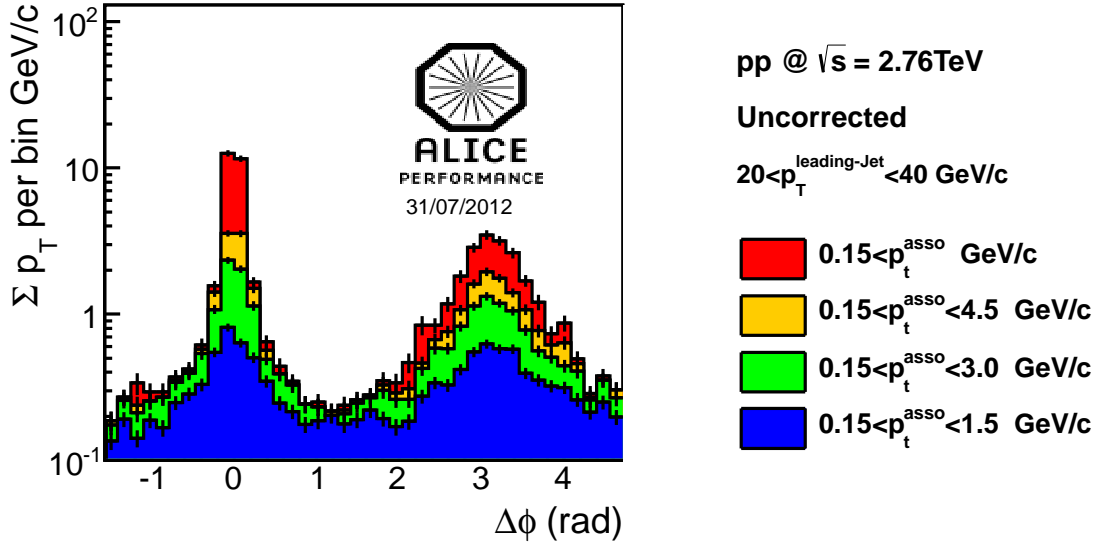
Figure 3.19: $\Delta\phi$ distribution of momentum of associate particle with respect to jet axis which is given by Eq.3.14 in pp collisions at $\sqrt{s} = 2.76$ TeV. The momentum range of associate particles divided into four bins as shown legend in right

1. leading jet properties

   We can see information of the leading jet in the near side of Fig.3.19. Average jet momentum in the leading jet momentum range is shown as sum of momentum in the near-side peak and jet shape also shown as width of the distribution.

2. Sub-leading jet properties The sub-leading jet properties can be shown in the away-side of the distribution as well as the leading jet. However the away-side width is not only coming from the sub-leading jet shape, di-jet axis fluctuation should be included in the away-side width.

3. Di-jet momentum asymmetry We can see the di-jet momentum asymmetry as difference between peak of near side and away side.

4. Underlying momentum distribution The momentum distribution of uncorrelated particle to with respect to di-jet is shown as base line of the distribution where around $-1/2\pi, 1/2\pi$ and $3/2\pi$.

5. Fragmentation function The distribution do not provide the fragmentation function itself but they have the information strongly correlated to the fragmentation function. You see the associate momentum region are separated to four bins which is shown blue, green, yellow and red. We can see how particle distributed in the leading jet and the sub-leading jet.

3.8.1   Comparing with MC event

In order to present we have proper tuned Monte Carlo events for the measurements. We show the results comparing with Monte Carlo events. We compared the $\Delta\phi$ distribution of Data with Monte Carlo in the whole azimuthal range and in the azimuthal range of the leading jet by fitting gauss function.

Fig.3.20 shows an example yield of jet particle correlation on data and Monte Carlo for the several associate particle momentum range in the same leading momentum range $20 < p_T^{\text{lead}} < 40$ GeV/c at $\sqrt{s} = 2.76$ TeV. If you see right figure of Fig.3.20, the yield ratio of data and Monte Carlo. The yield of data looks comparable but bit higher than the yield of Monte Carlo events. In the near-side and the away-side, the yield ratio is in $\pm 10\%$. However in the other region the ratio looks more higher around $\pm 20\%$. That indicate, Monte Carlo events can provide almost similar jets but the difference of underlying events between data and Monte Carlo is bit large.
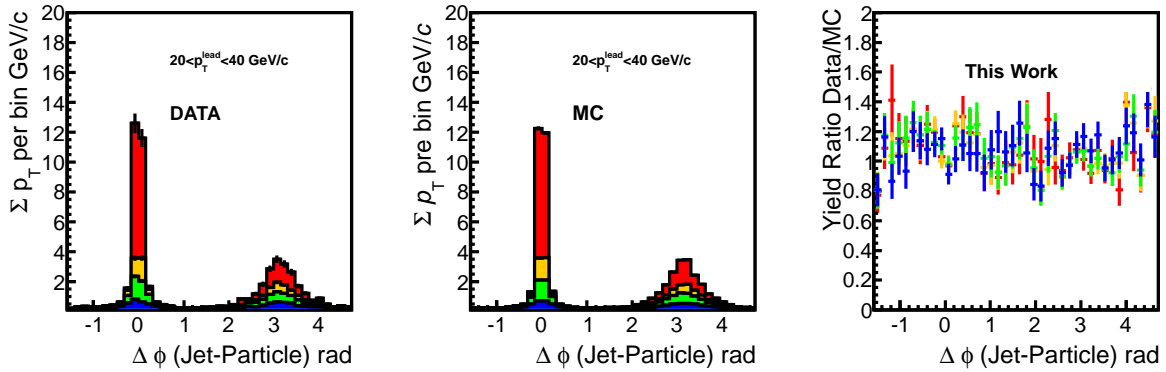
Figure 3.20: $\Delta\phi$ distribution of momentum of associate particles with respect to jet axis for data and Monte Carlo event for pp collisions at $\sqrt{s} = 2.76$ TeV, Left : jet-particle azimuthal correlation of data, Center : jet-particle azimuthal correlation of Monte Carlo, Right : yield ratio of data and Monte Carlo

Fig.3.21 shows shape of the near-side peak of the jet particle correlation for data and MC. We estimate jet width and height in momentum space fitting gauss function to the near-side peak of the yield. Width of the near-side peak is narrow with the increasing p_T of the associate particle range and the peak height is higher with p_T of the associate particle. And as far as we see the results, Monte Carlo events are consistent with data for all the associate particle momentum range for all the leading jet momentum range. You might have question why we have completely

matched shape with the shape of yield of data. The answer of the question is that we applied the fitting to the histogram with fine binning. If you look back right figure of Fig.3.20, you will realize the yield ratio around near-side peak is close to one.
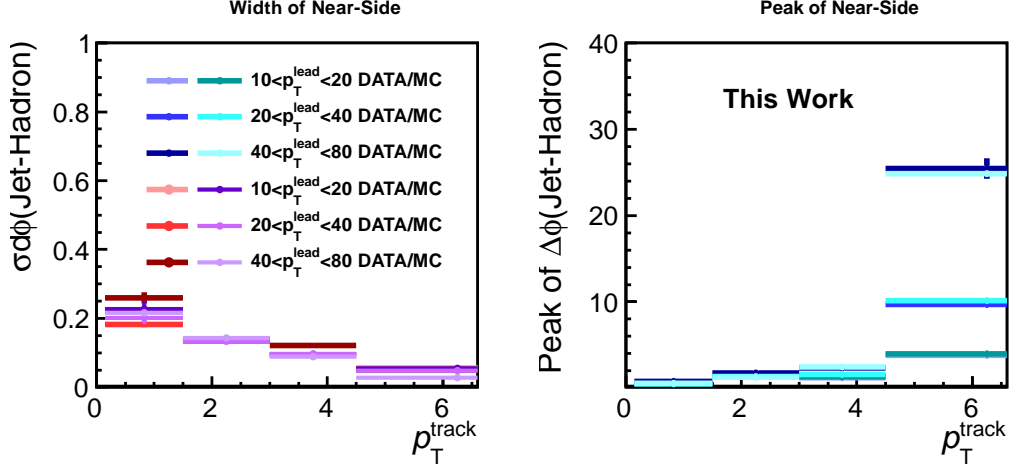
Figure 3.21: The peak and width of near-side shape of jet-particle azimuthal correlation estimated by fitting gauss function for data and Monte Carlo at $\sqrt{s} = 2.76$ TeV

3.8.2 Smearing and Contaminations

So far, we provide the uncorrected distribution in pp collisions, however the distribution is smeared by detector effects because of that we have non-ideal efficiency and finite resolution which is shown Fig.3.3. In addition, there are contribution of contamination charged particles which is not produced via fragmentation like decay from neutral mesons called Dalitz decay. To extract contribution meaningful physical particles in the jet-particle correlation, we have to estimate the ratio of physical particles in reconstructed particles. In general, the jet momentum also corrected due to such kind effects but in this analysis we don't correct jet momentum scale. The reason is we would like to compare the correlation within same reconstructed jet momentum scale. Actually we did not compare corrected distribution in pp collisions with un-corrected distribution in Pb-Pb collisions to let the effects cancel. But it's useful to understand physics information in jet-particle correlations.

By the relation we can estimate the detector smearing effects and the contaminations contribution in the distributions using Monte Carlo events from the relation. Fig.3.22 shows the smearing effects in reconstructed tracks and the contaminations ratio with respect to total generated particles in jet-particle correlation within triggered leading jet momentum range. And we can estimate the $\Delta\phi$ distribution of reconstructed physical particles applying correction factors which is shown by bottom figures in Fig.3.22. It is applied for only the inclusive yield for each trigger leading jet momentum range.If the correction factor is not applied the figure should added tag "Uncorrected".

When we compare the $\Delta\phi$ distribution in pp to compare the yield in Pb-Pb, we modified the

$\Delta\phi$ distribution in pp as that the di-jet event is reconstructed in huge background to minimize background effect when comparing with the yield in Pb-Pb. We will describe background effects in jet particle azimuthal correlation in Sec.4.3.1.
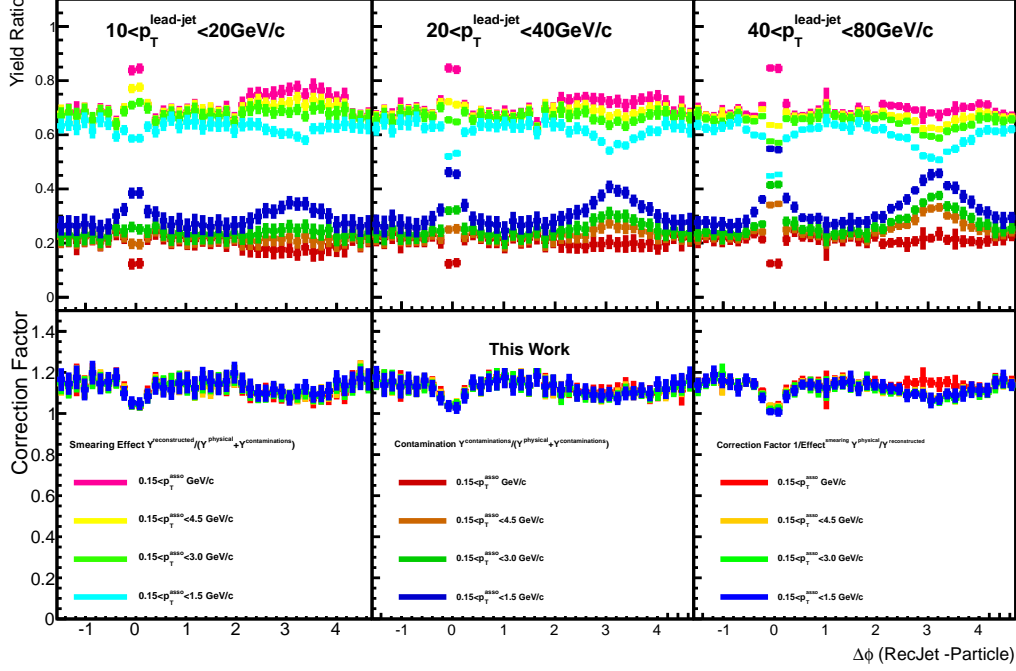
Figure 3.22: Top : Yield ratio to provide smearing effects by detectors and contribution of contamination particles in jet-particles azimuthal correlation, Bottom : Scaling factor to correct detector smearing effects and contamination contribution for each associate momentum range

3.9   Background Subtraction for Jet-Particle Correlation

Before we show the results of jet-particle correlation in Pb-Pb collisions, let us explain how to remove the background effects from $\Delta\phi$ distribution with respect to jet axis in huge background. As we explained in Sec.3.6 we can estimate background momentum contribution as Eq.3.13 in general. In jet-particle azimuthal correlation study, we can calculate the area of bins of histograms from width of x-bin and range of η acceptance. In this analysis acceptance of associate particles is chosen $|\eta| < 0.9$ which is limited by acceptance of global tracking. So the are of bins is given by Area$^{\text{bin}} = 2\pi/N_{\text{bin}} \times 1.8$, where N_{bin} is number of bins in $\Delta\phi$. However we divided the momentum region of the associate particles into four bins. Background density is different for each associate particle momentum range. Therefore we need to estimate the background momentum density for each associate momentum region as same as Sec.3.6.

Fig.3.23 shows background momentum density which comes from flat component, 2nd order
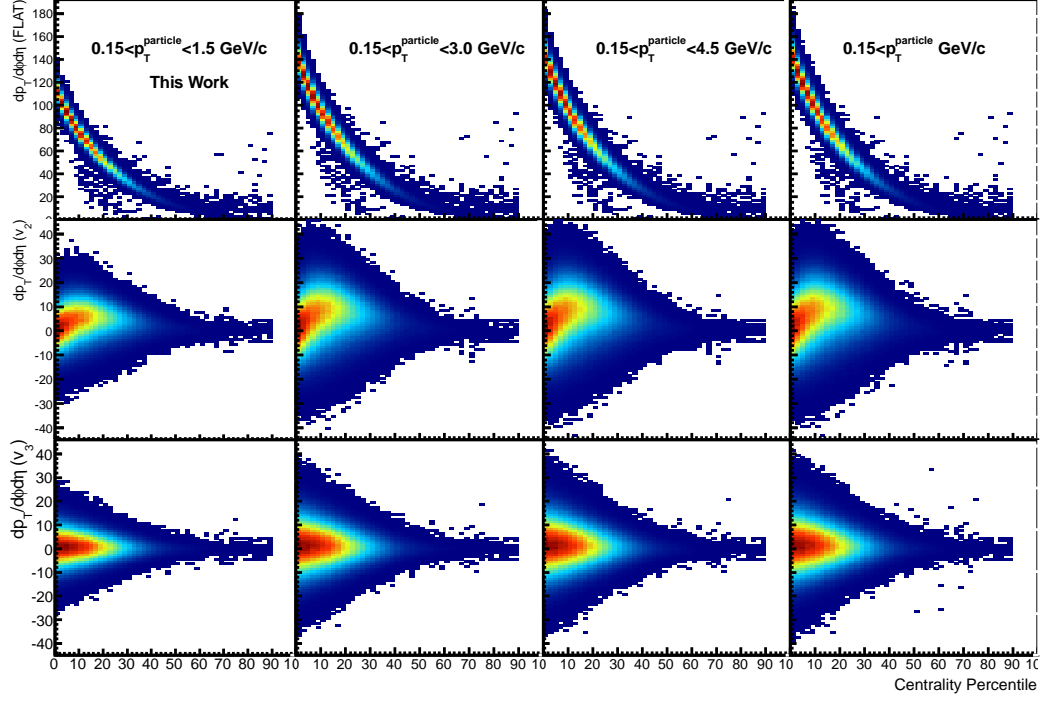
Figure 3.23: Background momentum density for each term in each momentum region of associate particles

component and 3rd order component for each momentum regions of associate particles. In the first figure from left,the momentum range is limited compared with the other. That is why the momentum density is smaller than the other. However in figure for the other momentum region, we can not see much difference. That suggest us background momentum is almost come from the particles which momentum less than 3.0 GeV/c.
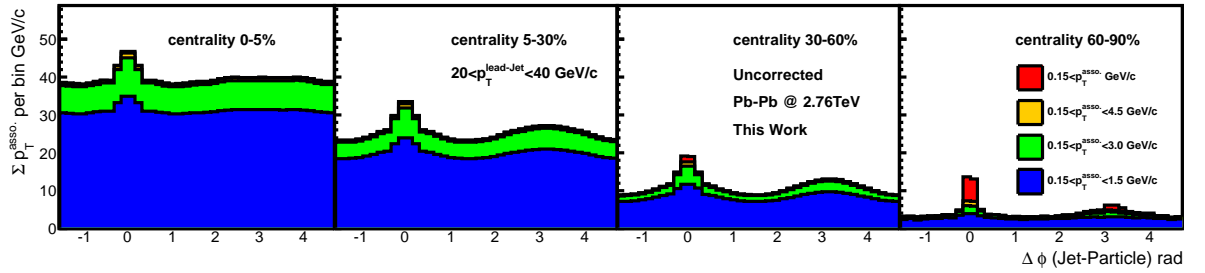
Figure 3.24: $\Delta\phi$ distribution of momentum of associate particles as a function of their axis with respect to jet axis before background subtracted from associate momentum distribution

Fig.3.24 shows the $\Delta\phi$ distributions with respect to the leading jet axis for each centrality

before background subtracted from the associate momentum distribution. We can see offset of underlying events with centrality. That offset comes from background particles which is generated by thermal bulk.
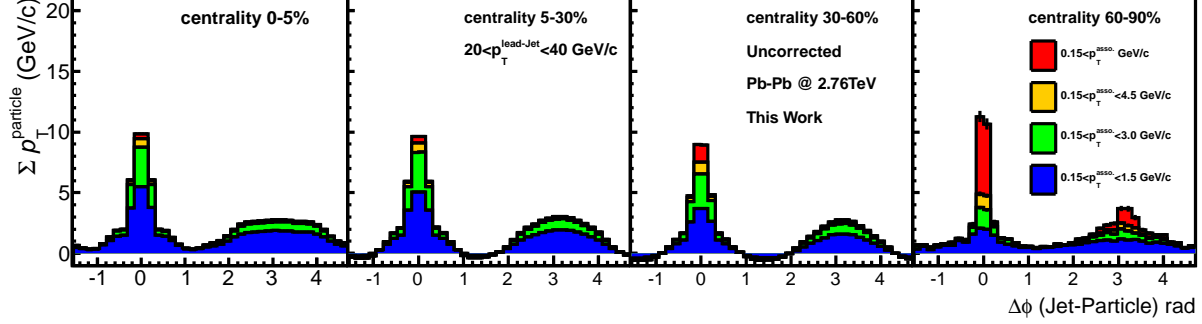
Figure 3.25: $\Delta\phi$ distribution of momentum of associate particles as a function of their axis with respect to jet axis after background subtracted from associate momentum distribution

Checking of the method to subtract background momentum from jet-particle correlation distribution can be cross-check of the background subtraction for reconstructed jet momentum. If the subtraction are not working for the jet measurements, it also don't work to subtract background momentum from distribution of jet-particle correlation. Fig.3.25 shows distribution of jet-particle correlation after background subtraction. As the figure shows, the background momentum looks subtracted for each centrality. As we can see, almost offset which we saw in Fig.3.24 is subtracted. That confirm our background subtraction works well.
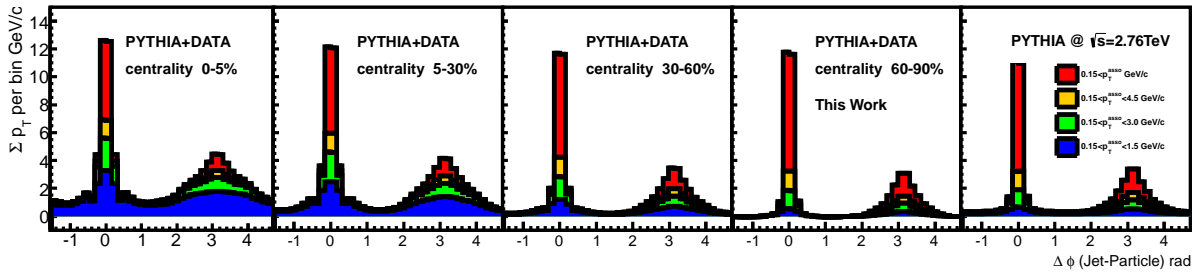
Figure 3.26: $\Delta\phi$ distribution of momentum of associate particles as a function of their axis with respect to jet axis for embedded PYTHIA di-jet into Pb-Pb events

We also try the method for data which is embedded PYTHIA di-jet event as we described in Sec.3.6. To see behavior the method that PYTHIA di-jet into events of Pb-Pb collisions, we embedded jets which is generated by PYTHIA and reconstructed by GEANT3 in pp-configuration

into events in Pb-Pb collisions at $\sqrt{s} = 2.76$ TeV.

To see background behavior in jet-particle correlation of PYTHIA embedded data we apply event selection as following,

- Di-jet event selection

- Matching axis $\Delta R(jet^{\text{lead-reconstructed}} - jet^{\text{lead-embedded}}) < 0.3$

Fig.3.26 shows yield of jet-particle correlation for embedded PYTHIA jets which reconstructed from data of Pb-Pb for each centrality. As we had seen the behavior to subtract background the distribution of PYTHIA which is embedded to Pb-Pb data.The background subtraction method looks completely working for jet-particle correlation measurements, as we mentioned that the result conform background subtraction for reconstructed jet momentum also should work.
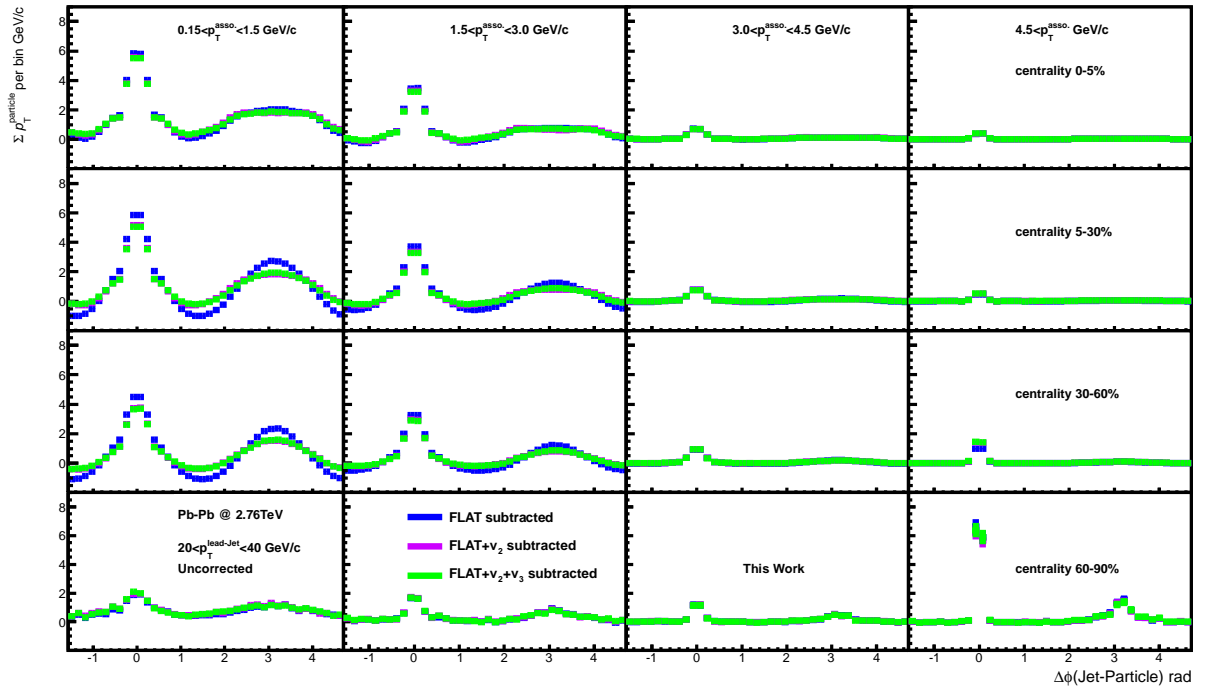
Figure 3.27: jet-particles azimuthal correlation in the momentum range of leading jet $20 < p_T^{\text{lead-jet}} < 40$ GeV/c for each centrality and for each associate momentum range. It is plotted the result with three back ground subtraction method. Blue line shows the distribution with only flat background subtraction. Violet line shows the distribution with flat and elliptic flow subtraction. And green line shows the distribution with flat , elliptic and triangular flow subtraction.

However we have to mention about base line of the distribution is smaller than zero in midcentral and mid-peripheral on Fig.3.25. And we can not see over subtraction which is appeared

in Fig.3.25. We are investigating the issue now. And it might be solved by tuning of parameters for the background estimation. But the effects might come from physics effects. In this analysis we keep the case because when we compare the yield of Pb-Pb with pp which is reconstructed in huge background, the effects can be ignore because almost technical systematic uncertainty should be canceled.

We checked contribution of background for each term in jet-particle correlations. The jet-particle correlations for each centrality and for each momentum range of the associate particles is shown in Fig.3.27. We test three background estimation. The first one is only flat background subtraction for jet reconstruction and momentum weighted azimuthal distribution(blue line). The second method is considered flat term and elliptic flow term in background estimation(violet line). And the last one is considered flat, elliptic flow and triangular term in background(green line). Violet line and green line are almost over rapped for all centrality and all momentum range of associate particles. There are clear difference between blue line and the others in low momentum range in the mid-central and the mid-peripheral. That results confirm that flow push the momentum of reconstructed jet. And magnitude of pushing by triangular is smaller than the magnitude of pushing by elliptic flow.

3.9.1   Systematic Uncertainties

In this analysis, we scale momentum weighted azimuthal distribution by number of triggered events. Therefore systematic uncertainty which come from trigger efficiency is canceled as definition. And, we have fine jet axis resolution and track axis resolution, so the effects can be ignorable.

It is considered as systematic uncertainties in jet particle azimuthal correlation as following.

- Momentum resolution of global track reconstruction $\pm 5\%$

  As we seen in right figure of Fig.3.3, the maximum momentum resolution of tracks is 10%. In this measurement, we add 5% uncertainty in the systematic uncertainty to get conservative results.

- Reconstruction efficiency of global track reconstruction $\pm 5\%$

  The statistical error in the track reconstruction efficiency can be systematic uncertainty, the maximum statistical errors in both of pp collisions and Pb-Pb collisions are around 3%. In this analysis, we added 5% uncertainty in the systematic error.

- Contaminations $\pm 1\%$ with respect to the distribution

  It are contained charged particles from gamma conversion and neutral particle decay about 6% in the low momentum region 2% in the high momentum region with respected to all reconstructed particles. In this analysis, we add 1% with respect to the yield of momentum weighted azimuthal distribution into systematic error for the contaminations.

- Momentum scale in jet reconstruction $\pm 10\%$

  For the momentum of reconstructed jets, the jet momentum scale can be changed by the momentum scale and the efficiency of the charged track reconstruction. And it is possibility to change the jet momentum by species of jet finding algorithm, parameters of the

algorithm. In pp collisions, we correct the distribution to extract meaningful information of the physical particles. And the correction factor was estimated using Monte Carlo event. Therefore we have to take into account the difference of data and Monte Carlo. We lump these kind of effects in the jet momentum scale. In this analysis, we estimate uncertainty in the jet momentum scale $\pm 10\%$.

For Pb-Pb collisions, we don't apply any correction. So we don't have to consider the difference of data and Monte Carlo. However we have uniform back ground like as the underlying event and the soft particles from the thermal bulk. The average difference of the flat background density is ± 1 GeV/c for all centrality except peripheral. And the average area of the reconstructed jets are 0.5. So the jet momentum can be changed in the range ± 0.5 GeV/c. To cover the range we keep $\pm 10\%$ for the jet momentum scale in Pb-Pb collisions.

- Flat back ground density for associate particles ± 1GeV/c (in Pb-Pb collisions)

  The background density of the flat term affect not only the jet momentum but also the associate particles yield. The uncertainty comes from the method of the background estimation and their parameters. We estimate the systematics uncertainty 1 GeV/c by Fig.3.11. And in the peripheral we decrease 2 GeV/c per unit η-ϕ space.

- Anisotropic back ground density $\pm 5\%$ for 2nd and 3rd order (in Pb-Pb collisions)

  In Pb-Pb collisions, we have non-uniform background, we also add for each term 5% which estimated by the maximum difference in Fig.3.11.

Chapter 4

Results and Discussions

In Chapter.3, we have described the detail of the analysis method of the jet measurements in ALICE and the jet-particle azimuthal correlations. In this chapter, we show the physics results in the jet-particle azimuthal correlations to extract the information of jet modification in Pb-Pb collisions. We show the distributions in pp collisions, followed by those in Pb-Pb collisions.

In the studies at CMS experiment, the missing momenta with respect to the di-jet axis have been measured to understand the particle re-distribution phenomena by jet modification. In the measurements by CMS, the momentum of particles are canceled out which distribute opposite direction along the di-jet axis to cancel out the background effects along di-jet axis like elliptic flow although the momentum of particle has the information of jet modification. And the measurements also do not provide the properties of jet, like spread angle, fragmentation function, and average momentum of the leading jets and the sub-leading jets.

In contrast, in this measurements, we can see average momentum of the jets and the particle distribution in the leading jet and the sub-leading jet individually with spread angle. Therefore we can extract jet properties in di-jet. And we also can extract jet modification effects in jets comparing the distribution in Pb-Pb collisions with those in pp collisions.

4.1   Jet-Particle Correlations in Proton-Proton Collision

First of all, we check behavior of the jets in pp collisions as a reference. Especially we provide momentum of the leading jet dependence of the jet shape. The momentum dependence is compared with the results on Pb-Pb collisions. And then we check the di-jet properties dependence to see more detail of jets in pp collisions, like particle multiplicity in the leading jets and the di-jet momentum asymmetry. We do not engage in deep discussion in this thesis, but these di-jet properties dependence are nice reference of jet modification in Pb-Pb collisions.

4.1.1   Leading Jet Momentum Dependence

Let's have a look at the momentum dependence of the corrected yield of the jet-particle azimuthal correlations. The detail of the measurements are described in Sec.3.8.

Fig.4.1 shows the momentum weighted azimuthal distributions of associate particle with respect to the leading jet axis for each momentum region of the associate particles; the lowest momentum bin is $0.15 < p_T^{\mathrm{asso}} < 1.5$ GeV/c, the following bin is $0.15 < p_T^{\mathrm{asso}} < 3.0$ GeV/c, the
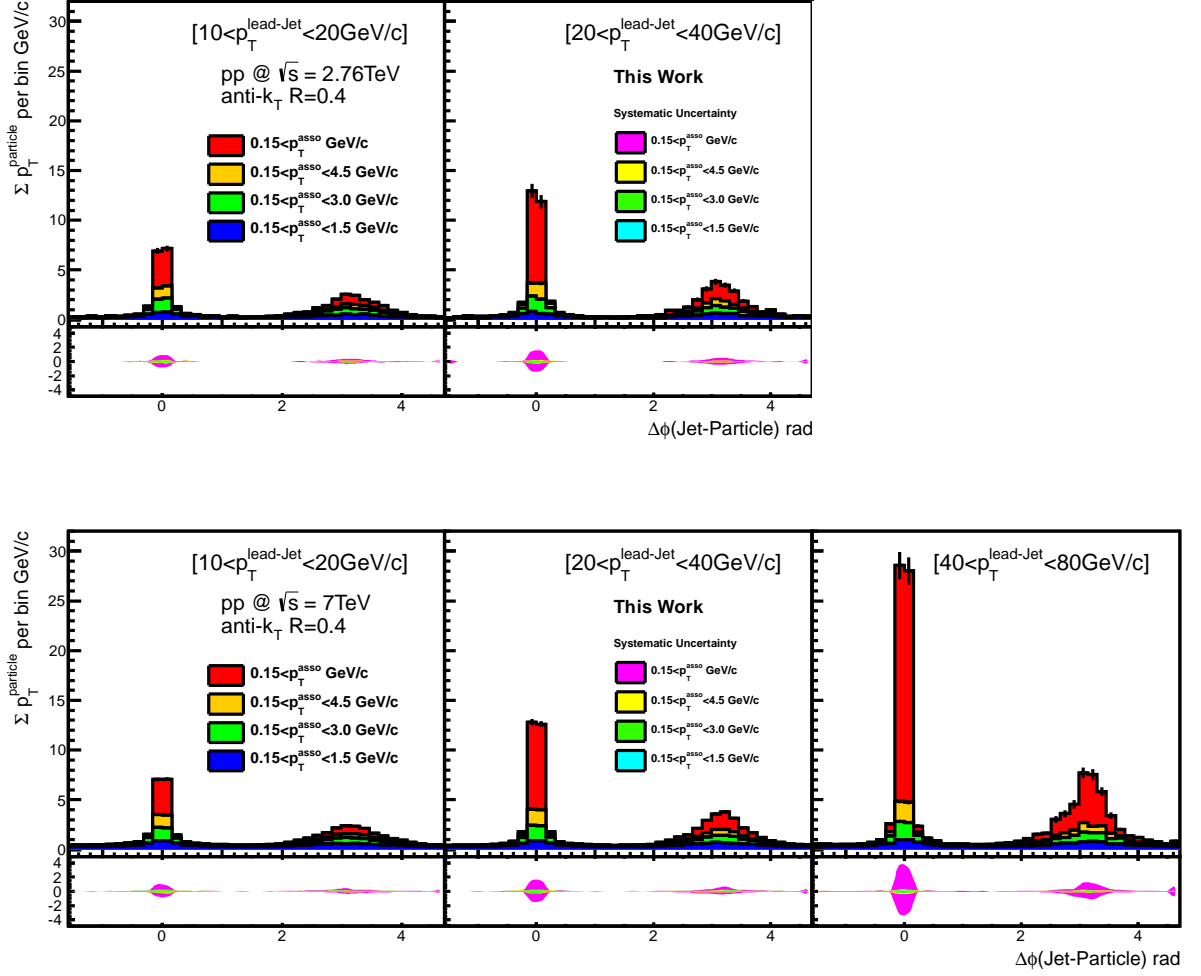
Figure 4.1: Momentum weighted azimuthal distribution of associate parti-
cles with respect to jet axis for each momentum range of leading
jet at $\sqrt{s} = 2.76$(Top) and 7 TeV(Bottom), divided into three
leading jet momentum region

2nd highest bin is $0.15 < p_T^{\text{asso}} < 4.5$ GeV/c and the highest bin is $0.15 < p_T^{\text{asso}}$ GeV/c. We also divide the momentum range of the leading jet into three bins; the lowest bin of jet momentum range is $10 < p_T^{\text{lead}} < 20$ GeV/c, the following bin as $20 < p_T^{\text{lead}} < 40$ GeV/c and the highest bin as $40 < p_T^{\text{lead}} < 80$ GeV/c. Due to the statistical limit, we only show till the 2nd momentum bin for $\sqrt{s} = 2.76$ TeV.

The systematic uncertainties(see Sec.3.9.1) are described in the lower small panel of the figures. As we look at the uncertainties, the uncertainties in lowest momentum bin of associate particles($0.15 < p_T^{\text{asso}} < 1.5$ GeV/c) shows 10% in all azimuthal range with respect to the leading jet axis($\Delta\phi$). But the uncertainties of the highest bin($0.15 < p_T^{\text{asso}}$ GeV/c) shows around 20% in close to the near-side peak and the away-side peak and around 10% in between the near-side

peak and the away-side peak.

As seen in the three bottom figures of Fig.4.1, the $\Delta\phi$ distribution at $\sqrt{s} = 7$ TeV shows that, the near-side peak become higher with the increasing the leading jet momentum and the fraction of the high momentum particles also looks increasing with the leading jet momentum. On the other hands the distribution of the lower momentum bin of associate particles does not strongly depend on the leading jet momentum. This fact indicates that the fragmentation function(see Eq.1.34) in low momentum particle does not strongly depend on the jet momentum because the fraction of each momentum bin of the associate particle strongly related to the fragmentation function. The behavior also can be seen in the away-side peak. The distributions at $\sqrt{s} = 2.76$ TeV which are shown on top in Fig.4.1 has same behavior of bottom figures.

The summary of the momentum dependence of the leading jet as following.

- The peak height of the near-side and the away-side become higher with the increasing jet momentum.

- The fraction of the high momentum particles is increasing with the leading jet momentum.

- The fraction of the low momentum particles do not strongly depend on the leading jet momentum.

- The distribution in pp at $\sqrt{s} = 2.76$ TeV looks similar to the distribution at $\sqrt{s} = 7$ TeV.

4.1.2 $M_{\text{ref.}}^{\text{lead}-\text{jet}}$ and A_j Dependence in Jet-Particle Correlation
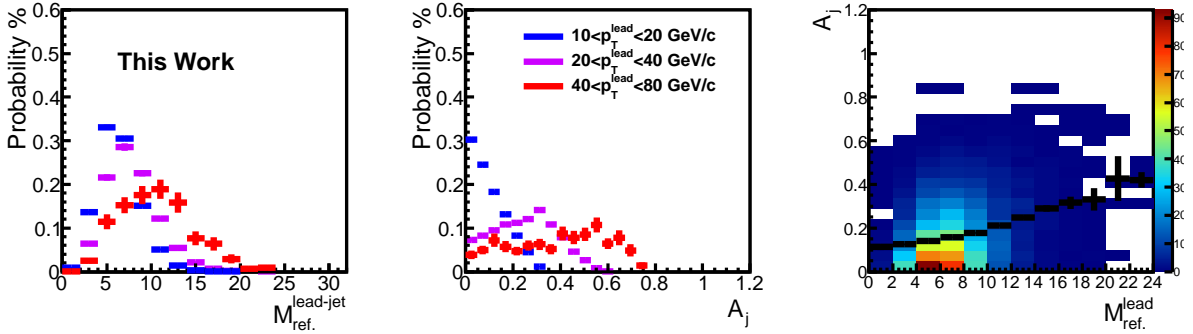
Figure 4.2: left : the distributions of multiplicity of constituents particles in leading jet, $M_{\text{ref.}}^{\text{lead}-\text{jet}}$ normalized by total entry of the distribution, center : the distributions of di-jet momentum asymmetry $A_j = (p_T^{\text{subleading}} - p_T^{\text{leading}})/(p_T^{\text{subleading}} + p_T^{\text{leading}})$, right : correlation of the constituents multiplicity and the momentum asymmetry

Let's explore in more detail of the di-jet properties. We see two type of properties; constituents particle multiplicity in the jet $M_{\text{ref.}}^{\text{lead}-\text{jet}}$ and di-jet momentum asymmetry A_j. First property is the constituents particle multiplicity dependence in the leading jet. The number

of constituents in the jets depend on parton species of the seed of the jets. It is known that gluon jets tend to have high multiplicity than quark jets[42]. Therefore the dependence of the properties provide knowledge of seed parton. It is also important to check effects of particle fluctuation in the distributions when we measure for the huge particle multiplicity events like Pb-Pb events. And the latter property is the di-jet momentum asymmetry A_j dependence. It is also important to check, because, we might use the di-jet momentum asymmetry to control the pass length in Pb-Pb collisions. The dependence is useful reference to investigate the effects. For the measurements we only provide the results of the distributions within the momentum range of the leading jet $20 < p_T^{\text{lead}} < 40$ GeV/c at $\sqrt{s} = 7$ TeV due to statistical limit of di-jet event at $\sqrt{s} = 2.76$ TeV. And for the study we do not apply any correction to the distributions. We describe the dependence of the particle multiplicity in the leading jet at first. Then we provide the dependence of the di-jet momentum asymmetry.

Fig.4.2 shows the properties of the di-jet which are analyzed. The left figure shows the distributions of multiplicity of the constituents particles in the leading jet, $M_{\text{ref.}}^{\text{lead-jet}}$ normalized by total entry of the distribution. And the center figure shows the distributions of the di-jet momentum asymmetry, $A_j = (p_T^{\text{subleading}} - p_T^{\text{leading}})/(p_T^{\text{subleading}} + p_T^{\text{leading}})$ normalized by the entry.

The average value of the highest momentum bin of the leading jet is larger than the value of the lowest momentum bin of the leading jet in the both figures the left and the center in Fig.4.2. This indicate the constituents multiplicity and the momentum asymmetry is increasing with the momentum of the leading jet. According to the right figure of Fig.4.2, The average of A_j goes up with $M_{\text{ref.}}^{\text{lead-jet}}$ that means, the di-jet momentum asymmetry increase with the multiplicity.

$M_{\text{ref.}}^{\text{lead-jet}}$ dependence
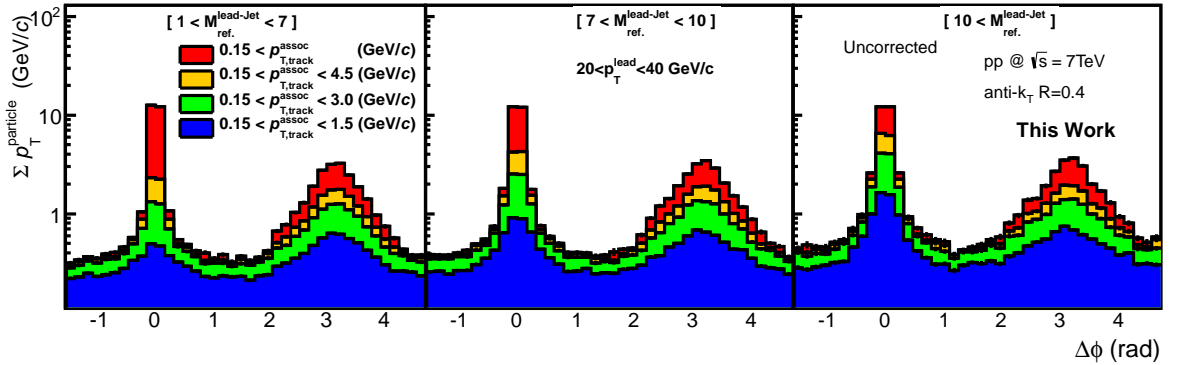
Figure 4.3: Jet-particles azimuthal correlations shown for three bins of the constituents multiplicity in the leading jet $M_{\text{ref.}}^{\text{lead-jet}}$ at pp $\sqrt{s} = 7$ TeV, the left for $1 < M_{\text{ref.}}^{\text{lead-jet}} < 7$, the center for $7 < M_{\text{ref.}}^{\text{lead-jet}} < 10$, the right for $10 < M_{\text{ref.}}^{\text{lead-jet}}$

At first, we see the multiplicity dependence in the leading jet. We divide the center figure

of bottom in Fig.4.1 into three multiplicity bins of the constituents particles in the leading jet $M_{ref.}^{lead-jet}$. The smallest bin provide the distribution in the range of $M_{ref.}^{lead-jet}$, $1 < M_{ref.}^{lead-jet} < 7$. The range of following bin is $7 < M_{ref.}^{lead-jet} < 10$. The range of last bin is $10 < M_{ref.}^{lead-jet}$.

The features we can get from Fig.4.3 are the following,

- The width of the near-side and the away-side peak seem to be broader with $M_{ref.}^{lead-jet}$,

- The fraction of the high momentum particles is decreasing with $M_{ref.}^{lead-jet}$,

- The momentum of the background particles is slightly increasing with $M_{ref.}^{lead-jet}$.

If we trigger the high multiplicity jets, shape of the jets is broader, and the leading jets tends to be triggered in the high multiplicity events. It is interesting that not only the peak is broader and the fraction of the high momentum particles is lower in near-side but also in the away-side. That can be understood as that, the probability of gluon jets are higher in the high multiplicity jets because gluon jets fragment with high particle multiplicity compared with quark jets[42].

A_j Dependence

We also see the dependence of momentum asymmetry A_j. We divide the center figure of bottom in Fig.4.1 into three A_j bins. The smallest bin provide the distribution in the range of A_j, $0 < A_j < 0.19$. The range of the following bin is $0.19 < A_j < 0.38$. The range of the last bin is $0.38 < A_j$.
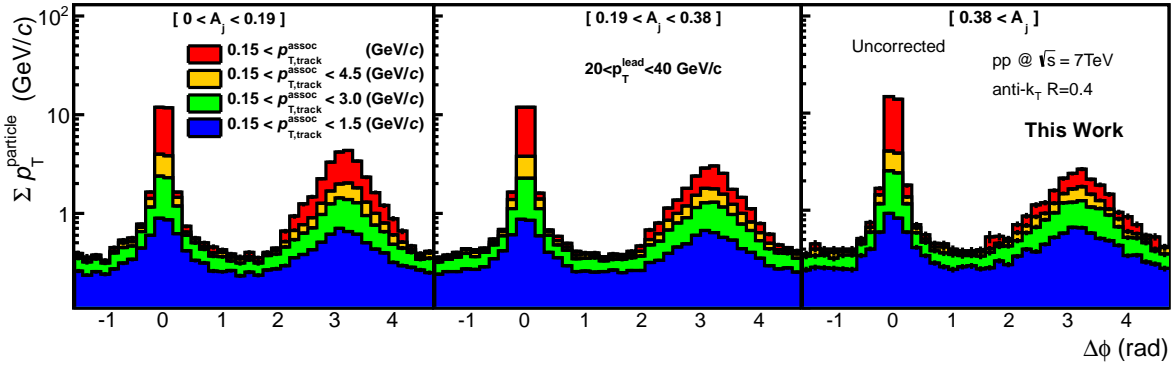
Figure 4.4: Jet-particles azimuthal correlations shown for three bins of di-
jet momentum asymmetry A_j in pp collisions at $\sqrt{s} = 7$ TeV,
the left for $0 < A_j < 0.19$, the center for $0.19 < A_j < 0.38$, the
right for $0.38 < A_j$.

The summary of Fig.4.4 is following,

- The height of the away-side peak is lower and width is broader with A_j,

- There are no much difference in shape of the near-side in all A_j bins, but the peak of the near-side is slightly higher with A_j.

The peak of the away-side in Fig.4.4 is lower and width is broader with A_j. That dependence comes from that if we select the large asymmetrical di-jet, average momentum of sub-leading jet should be lower. That is how we trigger low momentum jet as the sub-leading jet. And if we select such di-jet sample, average momentum of the leading jets also be higher relatively. That the reason why the peak of the near-side looks slightly higher with increasing A_j. In prospective measurements, we might classify the di-jet events using the momentum asymmetry to control pass length, the results should be the references for the future measurements.

4.2 Jet-Particle Correlations in Pb-Pb collision

Let us begin to show the results of the jet-particle correlations in Pb-Pb collisions. The analysis detail of the jet-particle correlations in Pb-Pb collisions is in Sec.3.9. In this section, we provide the results to know as much about the picture of jet modification in Pb-Pb collisions due to interaction between partons from hard scattering and constituents partons of hot/dense matter. In this measurements, we focus on the leading jet momentum dependence, the centrality dependence and the angular dependence with respect to the event plane. For the measurements we shed light on the knowledge of pass length dependence of the jet modification. As we have explained in Sec.3.2 and Sec.3.3, in the experiment, we control collision geometry by the centrality and the event plane. Therefore we can assume the pass length of the parton by the collision geometry and the jet axis with respect to the event plane. In the latter section we discuss particle re-distribution due to jet modification comparing the results on Pb-Pb collisions with the results of pp collisions.

4.2.1 Leading Jet Momentum Dependence

As well as the measurements in pp collisions, we check the momentum dependence of the leading jet in the jet-particle correlations in Pb-Pb collisions. Fig.4.5 shows the momentum weighted azimuthal distributions of the associate particles with respect to the leading jet in central collisions(top) and mid-central collisions(bottom). The systematic uncertainties are described in the lower panel of the figures.

In the near-side peak, it is denoted the same trends in the near-side peak in pp collisions as follows. The height of the peak become higher with the leading jet momentum. And the momentum fraction of high momentum particle also increases with the increasing the jet momentum. The shape of the correlation in low-momentum particles looks similar for all the leading jet momentum region. In away-side, the height of peak also increase as well. The fact confirm the away-side peak is not made by only the background particles fluctuation, even if the shape of away-side do not looks like jet. If all the sub-leading jet come from the background particles fluctuations, the away-side peak should not increase with increasing the leading jet momentum. These picture in away-side consistent the picture of measurements by CMS. However it is still unknown, how to be thermalized high momentum particles to low momentum particles in jets, because we still don't know the effects of thermal bulks fluctuation and flow effects in the measurements.

The summary of the section is following,
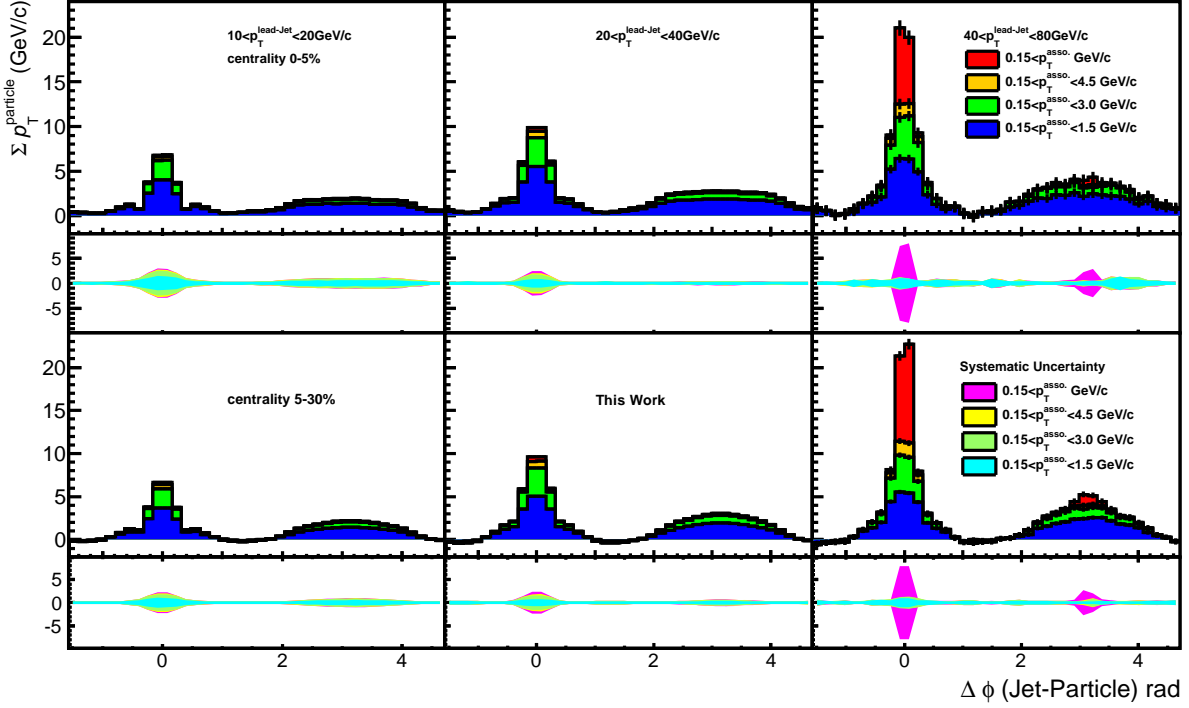
Figure 4.5: Jet-particle azimuthal correlations after background subtraction in the central collisions(top) and the mid-central collisions(bottom) for each the leading jet momentum

- The height in the near-side and away-side peak is higher with the increasing momentum of the leading jet,

- The fraction of the high momentum particles is increasing with the momentum of the leading jet.

4.2.2 Centrality Dependence

Let's see the $\Delta\phi$ distributions which are shown in Fig.3.25 again. The left four figures in Fig.4.6 are the same figures in Fig.3.25 and the right most figure shows the distribution in the same momentum range of the leading jet in pp collisions at the same collision energy. The systematic uncertainties are described in lower small panel.

As we see, the near-side peak and the away-side peak are getting sharper from the left to the right. And the fraction of the high momentum particles in the near-side and the away-side are also increasing compared with the left figure. That means, jet modification is stronger in the central collisions. And the average pass length of partons should be longer in the central, because system size is larger in the central collisions compared with the peripheral. The fact indicates, jet modification is stronger with the pass length of partons in the QGP. The yield in

the peripheral which is the 2nd figure from right looks similar to those of pp collisions. This is because the peripheral collisions are considered to almost be super position of multiple NN collisions. The shape of the mid-peripheral(at center) looks different compared with the shape of the peripheral(2nd right) and the left three figures looks similar compared with next figure of the three. This may imply a possibility that jet modification effects may saturate in rather short pass length.
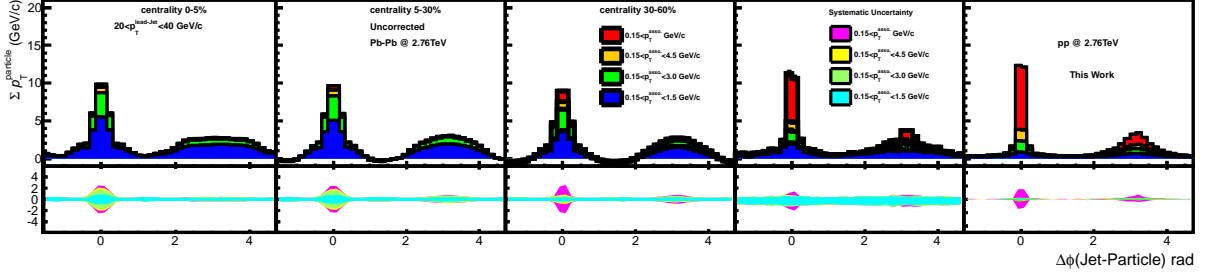
Figure 4.6: The momentum weighted $\Delta\phi$ distribution of the associate particles with respect to the leading jet axis in Pb-Pb collisions at $\sqrt{s} = 2.76$ TeV. The distributions are shown for centrality bin of 0-5%(left), 5-30%(2nd left), 30-60%(center), 60-90%(2nd right). And the most right figure shows the distribution in pp collisions as a reference

Fig.4.7 shows the peak height and the width of the near-side of $\Delta\phi$ distributions of the jet-particle correlation as a function of the momentum range of the associate particles. To determine the height and the width we fit gaussian function to the near-side peak. The widths of the near-side peak as a function of associate p_T^{asso} for each centrality are shown in the top two figures. The bottom figures shows the height of the near-side peak as a function of p_T^{asso} for each centrality. We divide the momentum range of the leading jet into two bins, the lower momentum bin is $10 < p_T^{\text{lead}} < 20$ GeV/c, and the higher momentum bins is $20 < p_T^{\text{lead}} < 40$ GeV/c.

As seen Fig.4.7, the width of the near-side peak is getting narrow with the momentum of the associate particles in all the centrality. In the peripheral collisions, the width of the near-side is sharper than the width of the other centrality. And there are not much momentum dependence of the leading jet. The trend is also seen in pp collisions (Fig.3.21). In Fig.4.7, we can see the centrality dependence of the peak height. In peripheral collisions, the peak height is getting higher with the momentum of the associate particles p_T^{asso}. The height of the near-side in the peripheral has the same trend of pp collisions(Fig.3.21). This confirm the leading jet in the peripheral collisions has similar behavior to the leading jet in pp collisions. In contrast, in the central collisions, clearly different behavior is seen from pp collisions. The peak height is decreasing with the decreasing p_T^{asso} both momentum ranges of the leading jet. And the height of the low momentum range of the associate particles in the central collisions is higher than the height in the peripheral collisions. In contrast, the height in central collisions is lower than the height in the peripheral collisions in the high momentum region of the associate particles. It is

considered that the fraction of the high momentum particles is suppressed and the fraction of the low momentum particles is enhanced by jet modification effects.
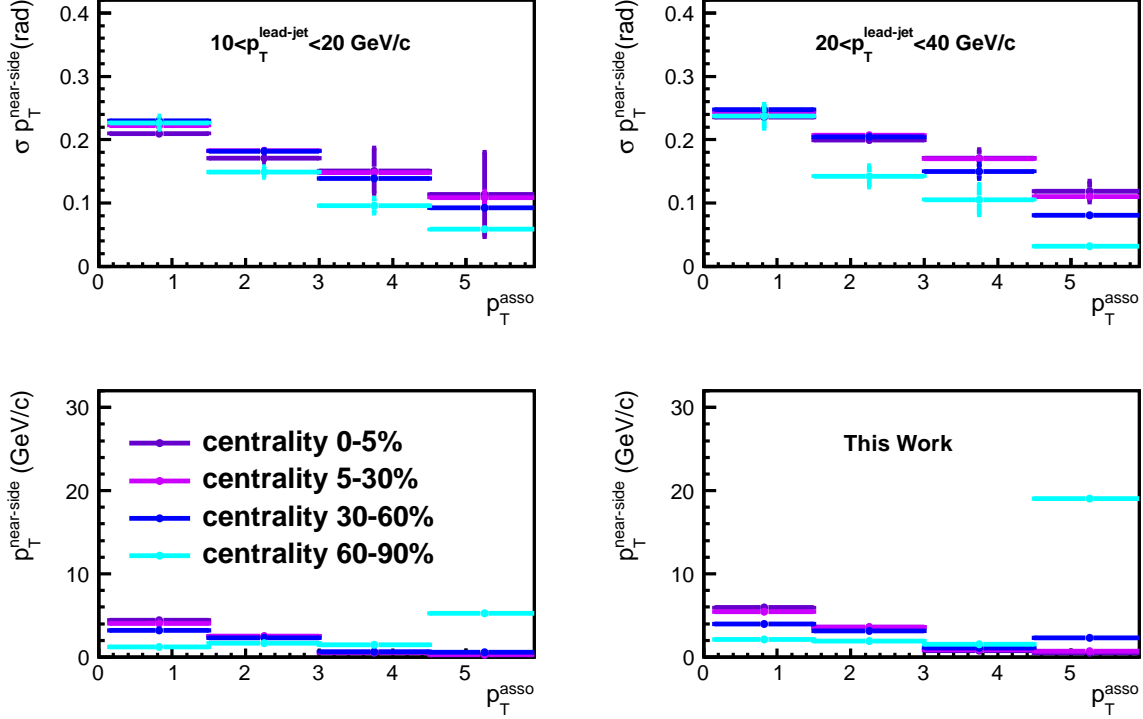
Figure 4.7: Top : the width of the near-side peak as a function of momentum range of the associate particles p_T^{asso} for each centrality, divided into two momentum ranges of the leading jet. Bottom : the height of the near-side peak as a function of p_T^{asso} for each centrality. The width and the height are estimated by fitting gaussian function

4.2.3 Dependence of Azimuthal Angle with respect to the Event Plane

Jet-particle azimuthal correlation is useful tool to understand bias of flow in jet reconstruction and the pass length dependence of jet modification in the QGP. In heavy ion collisions, there are anisotropy in the particle distribution with respect to the event plane as seen Sec.1.4.3. If we trigger the jets that the axis point to the event plane, the reconstructed jet momentum is pushed up by the flow, in contrast, we choose jets which point to the out-of plane we have jet sample which non-pushed momentum up by the flow.

We estimate the backgrounds which come from the uniform background, the elliptic flow and the triangular flow individually (see Sec.3.6). Therefore we can see the flow effects on jet shape for each term.

We provide two type of the yields for the each jet axis class with respect to the event plane on
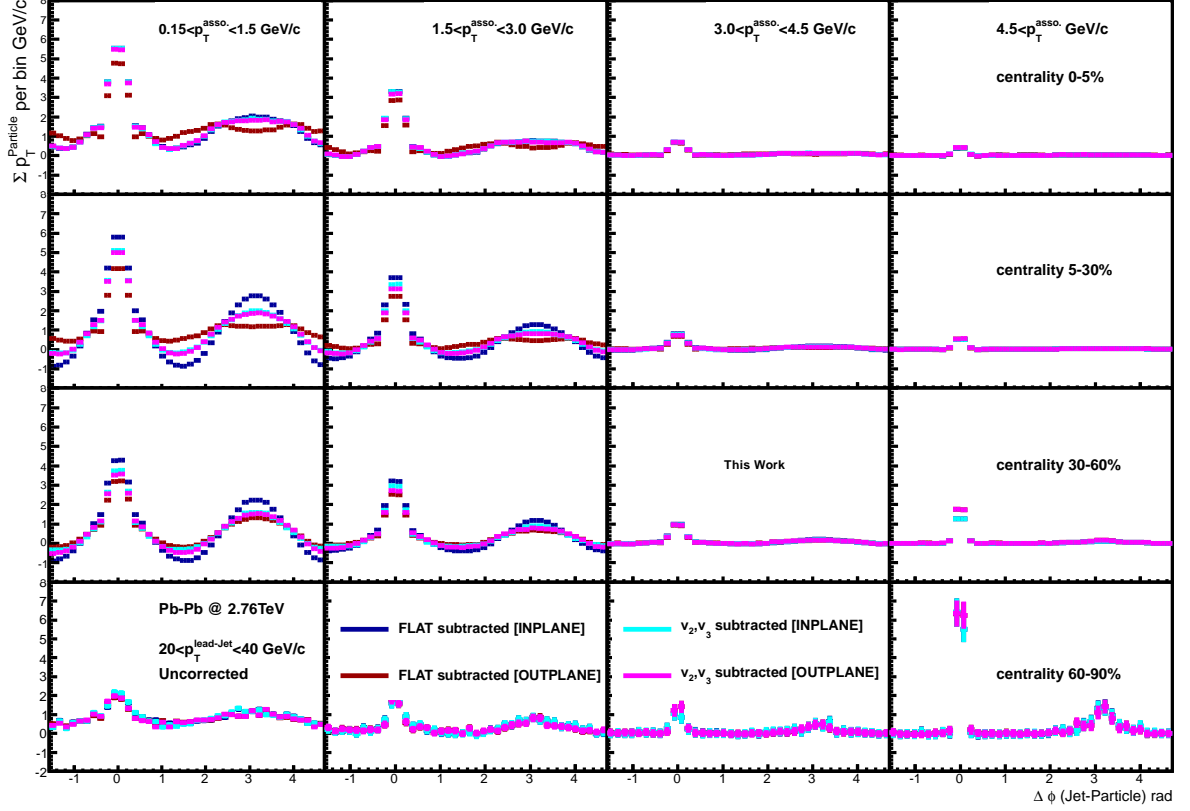
Figure 4.8: jet-particles azimuthal correlation in the momentum range of leading jet $20 < p_T^{\text{lead}-\text{jet}} < 40$ GeV/c for each centrality and for each associate momentum range. In this figure, it is estimated back ground effects of elliptic flow and triangular flow comparing yield with only flat background subtraction and full back ground including elliptic flow and triangular flow.

Fig.4.8; the first one is the $\Delta\phi$ distribution with only flat background subtraction, the 2nd one is the $\Delta\phi$ distribution with full background subtraction including the elliptic flow term and the triangular flow term. As seen the flat only subtracted yield for the in-plane and for the out-plane, the results still has flow effects from 2nd order and higher orders. On the other hands when we see the yield which subtracted the background effects including the 2nd order and the 3rd order, that all background effects should be subtracted, therefore the flow effects in $\Delta\phi$ distribution is minimized but the pass length dependence of jet modification should be still there.

As shown in the most left figures on 2nd from top and 3rd from top, there are drastic difference between the distribution for the in-plane and the out-plane with only flat background subtraction. The heights of peak in the near-side peak and the away-side for the in-plane are higher than the height for the out-plane. In contrast, the distributions for the in-plane and the out-plane with full background subtraction are almost overlapped. This fact indicate that elliptic flow push momentum of jets up which axis point to the event plane, but pushing effects

in the distribution by the anisotropic flow are minimized using the background subtraction method. And the difference of the distribution between for the in-plane and for the out-plane with only flat background subtraction looks stronger in low momentum region of associate particles, in particular, at the mid-central and the mid-peripheral. This is consistent, flow effects in momentum distribution are stronger in the low momentum particle region, and the elliptic flow is stronger at the mid-central and the mid-peripheral.

Summary from the event plane dependence in the $\Delta\phi$ distribution is following,

- The background subtraction method is working to reduce background effects including the anisotropic flow effects in jet measurements,

- Elliptic flow push momentum of jets up which axis point to the event plane,

- The effects of elliptic flow is stronger in the low momentum region of the associate particles, in particular, at the mid-central and the mid-peripheral.

4.3   Discussions

So far, we have seen the jet momentum and the shape of jets using jet-particle correlation in pp and Pb-Pb collisions. In particular, we focus jet momentum dependence, centrality dependence and azimuthal dependence with respect to the event plane. Before starting the discussion, we would like to bring up what we know and the issue we have to know. Here is the list.

- The fraction of the high momentum particles depends on the jet momentum

- Jet modification looks depending on the centrality

- Jet modification effects may saturate in rather short pass length.

- Jet momentum scale in Pb-Pb collision can be different from the scale in pp collisions by jet modification and background particles.

- Momentum weighted azimuthal distributions with respect to the jet axis can also be changed due to jet modification and background particles

4.3.1   Background Effects in Jet-Particle Correlation

In this measurements, we subtract background momentum from the associate particle distributions. However the fluctuation effects from backgrounds of huge particle density are still unknown. Therefore, in order to extract information of particle re-distribution by jet modification, we have to estimate the fluctuation effects in Pb-Pb collisions. But we can not divide the effects from jet modification effects in jet-particle correlation in Pb-Pb collisions. To estimate the effects, we try to reconstruct jets which is generated by PYTHIA in huge number of particles and see modification in the $\Delta\phi$ distributions of the associate particles.

Fig.4.9 shows $\Delta\phi$ distributions which are reconstructed embedded PYTHIA di-jet in data of Pb-Pb collisions. Details of the method are described in Sec.3.9. The most right figure on the top shows the embedded PYTHIA events, and the left four figures shows the yield of reconstructed
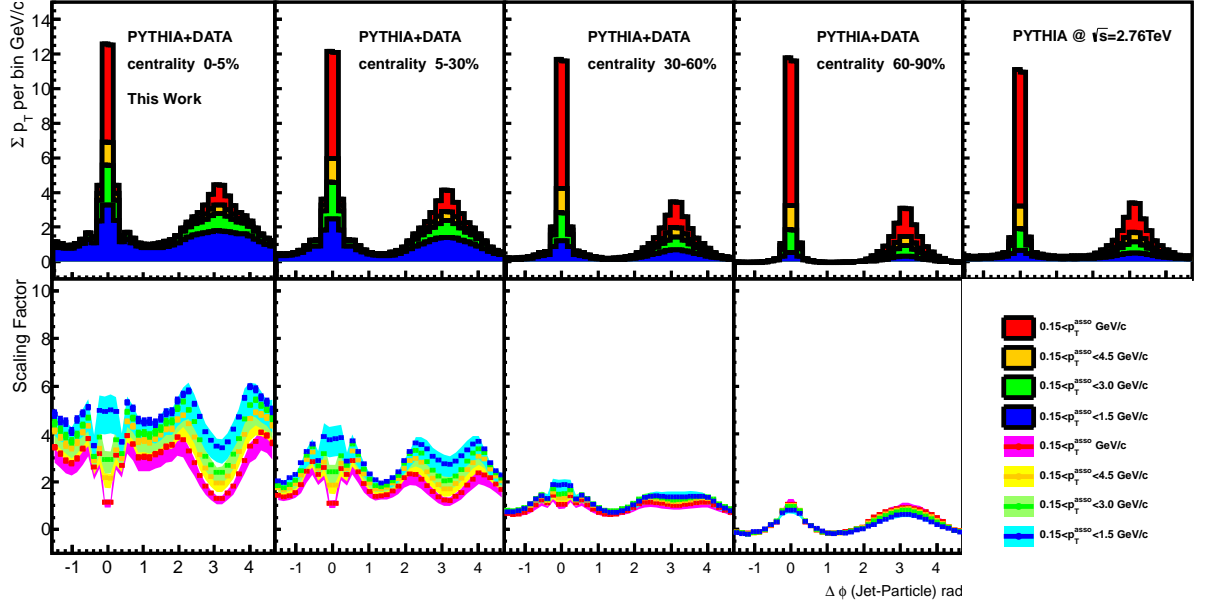
Figure 4.9: Jet-particle correlation of PYTHIA di-jet which embedded to data and scaling factors to modify the yield in pp collisions to include the background flow effects into the distribution. Top : Jet-particle correlation of PYTHIA di-jet for each centrality and of embedded PYTHIA di-jet. Bottom : Scaling factors to include background flow effects into jet-particle correlation in pp collisions.

PYTHIA jet in Pb-Pb collisions for each centrality. In the left figures, the background momentum in jets (see Fig.3.14) and the modification of the distribution due to background particles are included. If we divide the left four figures by the most right figure, we can get the scaling factors by background effects as seen in bottom figures of Fig.4.9. Then now, we get scaling factors to apply background particle effects the results of pp collisions. If we apply the scaling factors, we get the yield when we embed jets in pp into huge background of Pb-Pb environment.

The left four figures in Fig.4.10 shows the modified distributions of $\Delta\phi$ distribution in pp collisions by scaling factors which are shown in bottom figures of Fig.4.9. And the most right figure in Fig.4.10 shows the $\Delta\phi$ distributions before applied scaling factors. It is included effects of the huge background particle into the $\Delta\phi$ in pp collisions including the combinatorial jets effects applying the scaling factors.

The fraction of the low momentum particles is enhanced in the central. And width of jet in the near-side and the away-side are wider in the central. And the modification effects looks stronger in the central compared with the peripheral. In addition, the shape of the away-side in the central collisions in Fig.4.10 is similar to the shape of the away-side in central collisions in Fig.4.6. That indicate, we can assume background effects correctly, and the shape modification
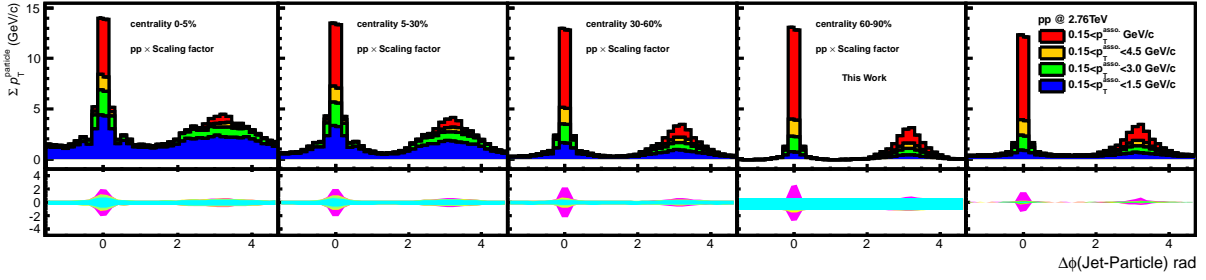
Figure 4.10: jet particle correlation modified by scaling factor which is shown in bottom figures of Fig.4.9 for each centrality.

of the away-side in the central is determined by the fluctuation of background particles. Then we finished to prepare to compare the $\Delta\phi$ distributions of Pb-Pb and pp collisions to extract jet modification effects.

4.3.2   Systematic Uncertainties for PYTHIA di-jet embedded events

We have to consider systematic uncertainties for the embedded di-jet sample. It is considered as systematic uncertainties for embedded PYTHIA as following.

- Momentum resolution of track reconstruction $\pm 5\%$

- Reconstruction efficiency in global tracking -5%

- Contaminations $\pm 1\%$ with respect to the yield

- Momentum scale in jet reconstruction $\pm 10\%$

- Flat back ground density for associate particles $\pm 1\mathrm{GeV/c}$ (+1, -2 GeV/c for peripheral in $20 < p_T^{\mathrm{lead}} < 40$ GeV/c)

- Anisotropic back ground density $\pm 5\%$ for 2nd and 3rd order

Almost same uncertainties in Pb-Pb collisions are considered for embedded PYTHIA. However, we knows tracking efficiency in Pb-Pb collisions is 5% wroth with respect to the efficiency in pp collisions. In this measurements, we embedded PYTHIA di-jets which are reconstructed in low tracking multiplicity environment by GEANT. So we apply the uncertainties for only the embedded jets sample.

4.3.3   Particle Re-distribution

To extract information of the particle re-distribution effects by jet modification. We compare the yield of momentum weighted $\Delta\phi$ distributions in Pb-Pb collisions and pp collisions which are scaled for the background fluctuation effects. The difference of the yields can be calculated as following (see Appendix.A),

$$Y^{Pb-Pb} - Y^{pp} = \frac{d(\sum p_T^{\mathrm{asso}}(\Delta\phi))}{dn^{\mathrm{dijet}}}\Big|_{p_T^{\min}<p_T^{\mathrm{lead}}<p_T^{\max}}^{\mathrm{Pb-Pb}} - \frac{d(\sum p_T^{\mathrm{asso}}(\Delta\phi))}{dn^{\mathrm{dijet}}}\Big|_{p_T^{\min}<p_T^{\mathrm{lead}}<p_T^{\max}}^{\mathrm{pp\times SF}}$$

$$\sim \quad \frac{d(Eff^{Pb-Pb}\times(\sum p_T^{\mathrm{hard}}(\Delta\phi)))}{dn^{\mathrm{dijet}}}\Big|_{p_T^{\min}<p_T^{\mathrm{lead}}<p_T^{\max}}^{\mathrm{Pb-Pb}} - \frac{d(Eff^{pp}\times(\sum p_T^{\mathrm{hard}}(\Delta\phi)))}{dn^{\mathrm{dijet}}}\Big|_{p_T^{\min}<p_T^{\mathrm{lead}}<p_T^{\max}}^{\mathrm{pp\times SF}}. \quad (4.1)$$

If we calculate the difference for each momentum region of associate particles, we can see shift of the fraction of the particles in Pb-Pb collisions. The shift indicate particle re-distribution due to jet modification by parton interaction in hot/dense matter.
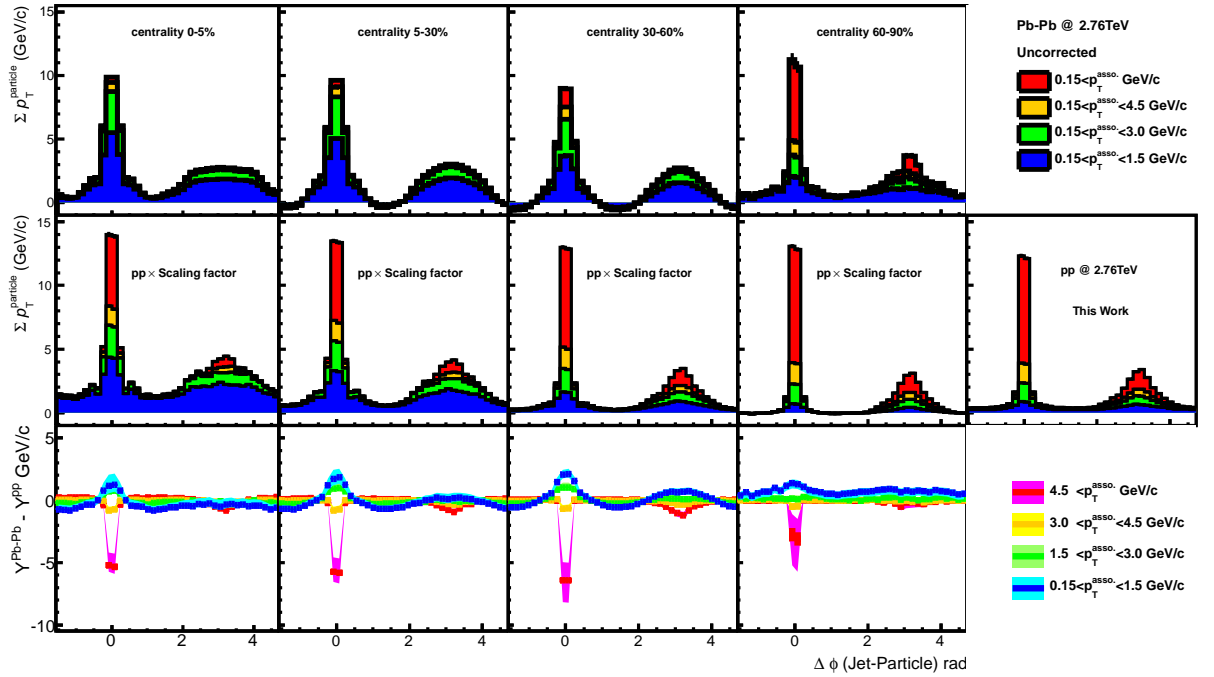
Figure 4.11: Top : Jet-particle correlations in Pb-Pb collisions for each centrality. Center : jet-particle correlations in pp collisions which are modified to include background flow effects and background jets effects into the yield of pp collisions. Bottom : Difference of the distribution of Pb-Pb collisions and pp collisions. The distribution provide jet modification effects in momentum range of the reconstructed jet $20 < p_T^{\mathrm{lead}} < 40$ GeV/c

The top four figures of Fig.4.11 provide the $\Delta\phi$ distributions with respect to leading jet axis shown in the momentum range of the reconstructed jet $20 < p_T^{\mathrm{lead}} < 40$ GeV/c in Fig.4.6($Y^{\mathrm{Pb-Pb}}$). And the left four figures in the middle are the yields of pp collisions applied the scaling factors(Y^{pp}), and the original distributions are the most right in the middle. The fraction of high momentum particles in the peak in the near-side and the away-side on the top figures looks suppressed compared with the fraction in the peaks on the middle figures for all centrality. If we have a look the away-side shape in central(most left figure) the shape looks not peak in the top figures but

we can see similar shape in the middle figures. That indicate, the embedding method works well to estimate the fluctuation of background particles in the $\Delta\phi$ distribution and the away-side jets are made by the fluctuation of background particles.

If we compare the top figures and the middle figures in the same centrality range, we can see jet modification effects in the near-side and the away-side. The bottom figures shows the differences of the top and the middle figures. The differences provide the $\Delta\phi$ distributions of the re-distributed particles due to jet modification. In the middle figures, background effects which come from the background flow and the background jet are included in the $\Delta\phi$ distributions and the reconstructed jet momentum. So the effects of backgrounds in the bottom figures are minimized when we subtract the distributions in the middle(Y^{pp}) from the top(Y^{Pb-Pb}). Then we can see clearly which momentum in the azimuthal angle with respect to jet axis are decreased and which momentum in the angle are increased by jet modification.

According to the bottom figures in Fig.4.11, the difference of the yields of Pb-Pb and pp in the high momentum particle makes valley and in the other momentum bin of the associate particle makes peak at $\Delta\phi = 0$ and $= \pi$ for all the centrality. And it looks balanced of the decreased momentum in the high momentum region of the associate particles and increased momentum in the low momentum region. Then we can see the width in the low momentum of particles looks wider compared with the width of distribution in the high momentum of particles. And the low momentum particles looks re-distributed into large spread angle compared with cone radius.

Through the measurements, we get the signal of the suppression of the high momentum particle production and the enhancement of the low momentum particle production. And the total momentum of the suppressed particle production and the enhanced particle production is almost balanced. That indicate, the decreased momentum of the high momentum particle production is re-distributed to produce particles in the low momentum range. And the spread angle of the re-distributed particles is larger than the azimuthal range of the missed high momentum particles. The trend that the production of the high momentum particles are suppressed is consistent with the results of modification in the two particle correlation which are shown Fig.1.11. And it also consistent with the results of the missing momentum measured by CMS which are shown in Fig.1.14, that the low momentum particles are re-distributed with the large spread angle. As just explained, the results are qualitatively-consistent with the previous measurements. We see jet modification in the leading jet and the sub-leading jet individually, we confirm the jet modification effects are not only in the away-side but also in the near-side. That issue was unknown, because ALTAS and CMS measured relative missing energy(or momentum) between the leading jets and the sub leading jets.

It is interesting that the modification effects looks almost same in between the central and the mid-peripheral. That indicate it is one of possibilities in the jet modification pictures that the jet modification has pass length dependence but the effects saturate in rather short pass length. To investigate more detail, we have to compare the distributions in the same momentum range of initial parton jet. In this analysis, we compare the distributions in the same momentum range of reconstructed jet which is included jet modification effects. That means, we compare the distribution in the different momentum ranges of initial parton jets which are not effected by the jet modification. That is why, the saturation effects might come from the cocktail of the difference of energy range of initial parton jet and the surface trigger effect due to the jet modification. After carefully observing the centrality dependence, jet modification looks gradually decreasing

from central to mid-peripheral. In this measurements, we regard the particles distributed to almost uniform with respect to the jet axis as the background particles. The effects can be the cause to change scale of the jet momentum and we might subtract the momentum of the re-distributed particles as background. And the effects can be seen in the away-side though the effects looks smaller in the near-side. To investigate, the issue it is needed to measure in same momentum range in initial parton jet.
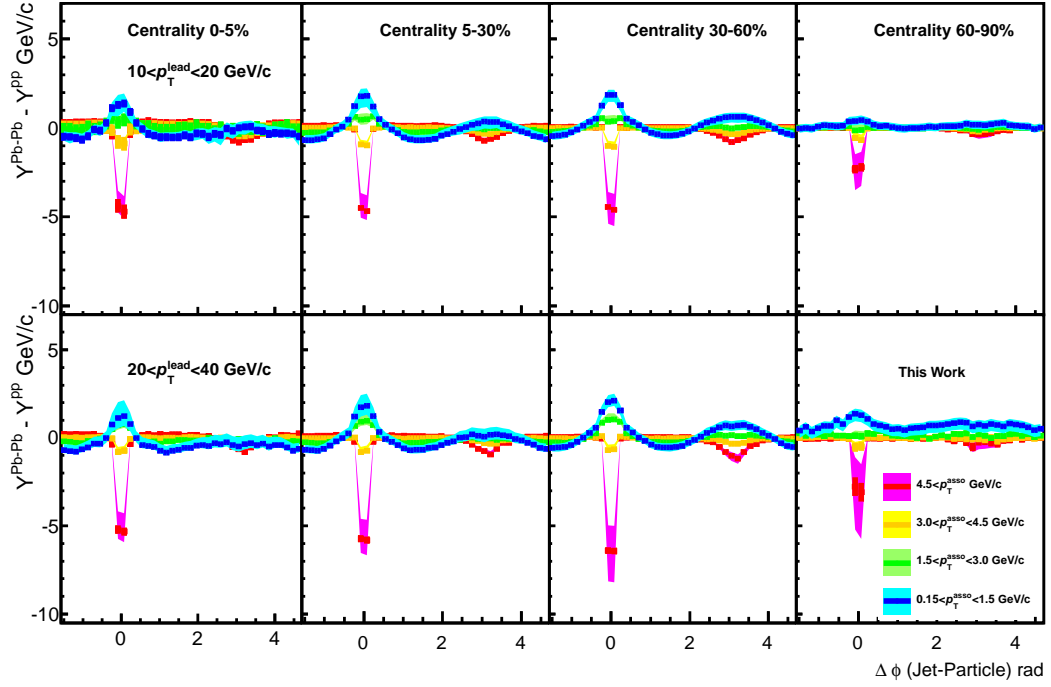
Figure 4.12: $\Delta\phi$ distribution of re-distributed particles in momentum range of reconstructed jet $10 < p_T^{\text{lead}} < 20$ GeV/c in top figures, $20 < p_T^{\text{lead}} < 40$ GeV/c in bottom figures

Fig.4.12 shows pp-distribution subtracted momentum weighted azimuthal distribution for each the leading jet momentum. In the top figures, jets in the momentum range $10 < p_T^{\text{lead}} < 20$GeV/c is chosen as trigger jet. And in bottom figures, the momentum range of the leading jet is $20 < p_T^{\text{lead}} < 40$GeV/c. In the range of the high momentum jets, the similar centrality dependence is observed within the low momentum range of the leading jet. The differences between increased momentum in the low momentum particles and decreased momentum in the high momentum particles, become larger with the increasing leading jet momentum. That suggest us the jet modification effects increase with the increasing jet momentum.

To investigate particle re-distribution by jet modification, we integrate the differences of between the $\Delta\phi$ distributions in Pb-Pb collisions and pp collisions. Fig.4.13 shows the integral values as a function of the associate particle momentum for each centrality divided into the two leading jet momentum range. Top figures shows the value of integral for the near-side the range with respect to the leading jet is $-0.5 < \Delta\phi < 0.5$ rad, and the bottom figures shows
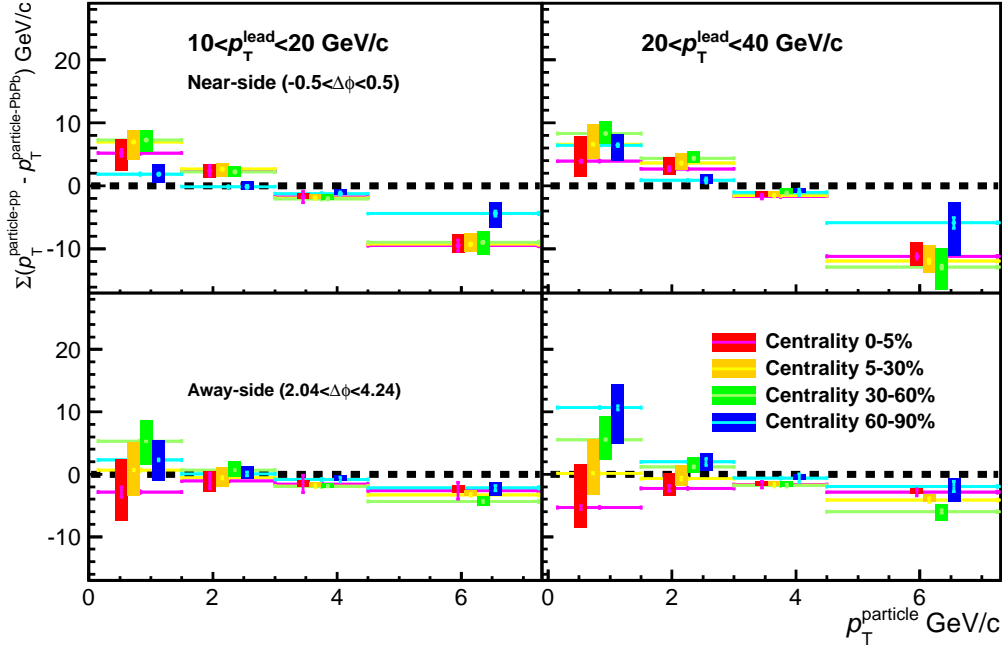
Figure 4.13: Sum of momentum difference between jet-particle azimuthal
correlation of Pb-Pb and pp as a function of associate particles
for each leading jet momentum. Top figure shows it for near-
side peak ($-0.5 < \Delta\phi < 0.5$), and bottom for away-side ($2.04 < \Delta\phi < 4.24$).

for the away-side in the range $2.04 < \Delta\phi < 4.24$. The integral value provide the total modified
momentum in the $\Delta\phi$l range and momentum rage of the associate particle. And the gradient is
correlated to the strength of jet modification.

It looks balanced the decreased momentum in the high momentum range of associate particles
and the increased momentum in the low momentum range. In the near-side, the slope of the
peripheral is smaller than the slope of the other central region. That means, modification effects
are smaller in the peripheral collisions. For other centrality, it is almost same slope in systematic
error. If we compare right figure with left figure on the top. We can see slope is larger with the
momentum of the leading jet. In the away-side peak, we have large systematic uncertainties in
particular in the low momentum particle region. Therefore it's is difficult to discuss the physics
for the away-side. However, if we compare the points for the mid-peripheral in the top figure
with the low figure, slope of the top figure is larger than the bottom. That confirm the total
modification effects depend on momentum of jets. So that we select lower momentum jets with
respect to the leading jet as the sub-leading jet.

4.4   Summary

The first data of pp and Pb-Pb collisions with highest energy in the world are analyzed for
jet measurements. Through the measurements, we conform the analysis method of jet-particle

correlation is useful to investigate jet properties. Then we see jet properties in pp collisions and Pb-Pb collisions using jet-particle azimuthal correlations.

In proton-proton collisions, we see momentum dependence of the leading jet, $M_{ref.}^{lead}$ dependence and A_j dependence in the jet-particle azimuthal correlations. We see that the jet shape is sharper and the peak is higher with jet momentum, jet shape is broader with $M_{ref.}^{lead}$ and the shape is broader and the peak is lower in the away-side with in large A_j.

In Pb-Pb collisions, we check the leading jet momentum dependence, the centrality dependence and the axis dependence with respect to the event plane in the jet-particle correlations. We see that the jet shape is sharper and the peak is higher with jet momentum, the jet shape is sharper and the higher is from the central collisions to the peripheral collisions and we can't see significant difference between the in-plane and the out-plane.

Finally, we extracted information of the particle re-distribution comparing the distribution of Pb-Pb and pp collisions. By through the measurements, we got the knowledge as following.

- We can see particle re-distribution effects in the leading jet and the sub-leading jet individually.

- The momentum fraction of the high momentum particles is suppressed due to jet modification.

- The momentum fraction of the low momentum particles is enhanced due to jet modification.

- The missing momentum of high momentum particles re-distribute into low momentum particles with large spread angle.

- The decreased momentum in high momentum region of the associate particles and increased momentum in low momentum region looks almost balanced.

- Jet modification quantity is increase with the leading jet momentum.

- It is possibility of that jet modification effects saturate in the short pass length.

To investigate more detail of jet modification, it is need to compare the distribution of Pb-Pb collisions and pp collisions in same momentum range of initial parton jet. To do that we have to start to tune up event generators which consider jet modification to get information of jet momentum scale due to jet modification. And this results, are the benchmark to tune up the Monte Carlo, because we measure the modified momentum with their spread angle.

Chapter 5

Conclusion and Future

In the nature around us, quarks and gluons are confined in hadrons due to "confinement of quarks". However, the coupling strength of the QCD between quarks and gluons is to be asymptotically weaker with the increasing their energy. At high temperature the quarks and gluons move freely beyond the boundary of hadrons. Such high energy state is called Quark-Gluon Plasma(QGP). To create such state on the earth, the ultra relativistic heavy ion collision is unique tool.

It has been observed several signatures of the QGP formation at the Relativistic Heavy Ion Collider(RHIC). Suppression of high momentum particles is one of the signatures. High momentum particles are known to be produced in characteristic phenomena, jet , where high momentum particle are produced in cluster. The jet is produced when parton in each projectile is scattered with large momentum, followed by fragmentation into many hadrons.

It is considered that the cause of the suppression of high momentum particle is due to the characteristic energy loss of the parton in the QGP. On the other hands, many low momentum particles are formed at characteristic energy loss and the additional instead large angles from original low momentum particles is often called modification of jet. In theoretical approach, the energy loss and the shape modification of the jet is strongly relate to properties of hot/dense matter particularly gluon density and initial temperature of the QGP. Therefore study of jet modification is a good tool to investigate the properties of the QGP. Experimentally it is very important to measure the energy loss together with the energy re-distribution at large angles.

At the RHIC, it is difficult to collect enough data because of its low rate. The production cross-section of jet is strongly related to the collision energy. The Large Hadron Collider(LHC) starts nuclear-nuclear collisions with highest energy from 2010. LHC provides good opportunity to study the jet physics in heavy ion collisions to investigate parton interaction between jets and the QGP with higher statistics. Former study of the jet physics in heavy ion collisions has been done at the LHC by CMS. They have suggested the existence of re-distributed particles at large angles. In their study, the information of the spread angle is minimum and they can not see detail of jet modification.

In this paper, a new analysis method is proposed in order to see the modified energy(or momentum) with the spread angle. Proposed new method handles the momentum weighted azimuthal distribution of the associate particles with respect to the leading jet and direct comparison of pp and Pb-Pb collisions have been done. In this thesis, the centrality dependence and

the leading jet momentum dependence are shown to extract jet modification effects, which shed light on the knowledge of the pass length dependence of jet modification.

We observe that the low momentum particles are re-distributed at large angles in the away-side of the jet with respect to the leading jet. This feature is consistent with CMS results. Furthermore we see the re-distributed momentum in the near-side. The missing momentum and the re-distributed momentum is found to be almost balanced. We see jet modification is larger with the highest jet momentum, and the effect is also larger in the central compared with peripheral collisions.

This measurement, provide several versatile measurements in the near future. We might classified Pb-Pb event using jet momentum asymmetry A_j and number of particles of constituents particles in jet $M_{ref.}^{lead}$, as we do in the studies for pp collisions. By the measurement, we can control pass length dependence therefor we will see more detail of pass length dependence of jet modification through the measurements. It is also interesting to see the possibility of saturation of jet modification effects. To investigate the issue we have to prepare Monte Carlo events of jets which is considered jet modification effects like QPYTHIA. The jet-particle correlation is useful to tune-up the Monte Carlo events. And we also can extract properties of the QGP comparing data and modified Monte Carlo by jet modification with several parameters. We already establish jet-particle correlation with embedded di-jet events into Pb-Pb events therefor we can compare PYTHIA jet and QPYTHIA jets after the tuning of QPYTHIA in same momentum range of initial parton momentum. We also can measure using the method with the hadron particle identification. We knows the particle production mechanism is different between in the high momentum particles and in the low momentum particles. Heavy particles like proton come from jets via fragmentation. In ALICE experiment, we have ring imaging Cherenkov counters to identified high momentum particles. Therefore we might know several knowledge using the difference like as pion-proton production ratio in jet particle correlation. In this way, we will be new stage of jet modification measurements using jet-particle correlation. And it's will provide the analysis with attribution of ALICE.

Appendix A

AppendixA

Difference of momentum weighted $\Delta\phi$ distribution can be calculated as following.

$$
\frac{d(\sum p_T^{\mathrm{asso}}(\Delta\phi))}{dn^{\mathrm{dijet}}}\bigg|_{p_T^{\min}<p_T^{\mathrm{lead}}<p_T^{\max}}^{\mathrm{Pb-Pb}} - \frac{d(\sum p_T^{\mathrm{asso}}(\Delta\phi))}{dn^{\mathrm{dijet}}}\bigg|_{p_T^{\min}<p_T^{\mathrm{lead}}<p_T^{\max}}^{\mathrm{pp\times SF}}
$$

$$
= \frac{d(Eff^{\mathrm{Pb-Pb}}\times(\sum p_T^{\mathrm{hard}}(\Delta\phi)+\sum p_T^{\mathrm{contami}}(\Delta\phi)+\sum p_T^{\mathrm{BKG^{hard}}}(\Delta\phi)+\sum p_T^{\mathrm{BKG^{soft}}}(\Delta\phi)))}{dn^{\mathrm{dijet}}}\bigg|_{p_T^{\min}<p_T^{\mathrm{lead}}<p_T^{\max}}^{\mathrm{Pb-Pb}}
$$

$$
- \frac{d(Eff^{\mathrm{pp}}\times(\sum p_T^{\mathrm{hard}}(\Delta\phi)+\sum p_T^{\mathrm{contami}}(\Delta\phi))+Eff^{\mathrm{Pb-Pb}}\times(\sum p_T^{\mathrm{BKG^{hard}}}(\Delta\phi)+\sum p_T^{\mathrm{BKG^{soft}}}(\Delta\phi)))}{dn^{\mathrm{dijet}}}\bigg|_{p_T^{\min}<p_T^{\mathrm{lead}}<p_T^{\max}}^{\mathrm{pp\times SF}}
$$

$$
= \frac{d(Eff^{\mathrm{Pb-Pb}}\times(\sum p_T^{\mathrm{hard}}(\Delta\phi)+\sum p_T^{\mathrm{contami}}(\Delta\phi)))}{dn^{\mathrm{dijet}}}\bigg|_{p_T^{\min}<p_T^{\mathrm{lead}}<p_T^{\max}}^{\mathrm{Pb-Pb}}
$$

$$
- \frac{d(Eff^{\mathrm{pp}}\times(\sum p_T^{\mathrm{hard}}(\Delta\phi)+\sum p_T^{\mathrm{contami}}(\Delta\phi)))}{dn^{\mathrm{dijet}}}\bigg|_{p_T^{\min}<p_T^{\mathrm{lead}}<p_T^{\max}}^{\mathrm{pp\times SF}}
$$

$$
= \frac{d(Eff^{\mathrm{Pb-Pb}}\times(\sum p_T^{\mathrm{hard}}(\Delta\phi)))}{dn^{\mathrm{dijet}}}\bigg|_{p_T^{\min}<p_T^{\mathrm{lead}}<p_T^{\max}}^{\mathrm{Pb-Pb}} - \frac{d(Eff^{\mathrm{pp}}\times(\sum p_T^{\mathrm{hard}}(\Delta\phi)))}{dn^{\mathrm{dijet}}}\bigg|_{p_T^{\min}<p_T^{\mathrm{lead}}<p_T^{\max}}^{\mathrm{pp\times SF}}
$$

$$
+ \frac{d(Eff^{\mathrm{Pb-Pb}}\times(\sum p_T^{\mathrm{contami}}(\Delta\phi)))}{dn^{\mathrm{dijet}}}\bigg|_{p_T^{\min}<p_T^{\mathrm{lead}}<p_T^{\max}}^{\mathrm{Pb-Pb}} - \frac{d(Eff^{\mathrm{pp}}\times(\sum p_T^{\mathrm{contami}}(\Delta\phi)))}{dn^{\mathrm{dijet}}}\bigg|_{p_T^{\min}<p_T^{\mathrm{lead}}<p_T^{\max}}^{\mathrm{pp\times SF}}
$$

$$
\sim \frac{d(Eff^{\mathrm{Pb-Pb}}\times(\sum p_T^{\mathrm{hard}}(\Delta\phi)))}{dn^{\mathrm{dijet}}}\bigg|_{p_T^{\min}<p_T^{\mathrm{lead}}<p_T^{\max}}^{\mathrm{Pb-Pb}} - \frac{d(Eff^{\mathrm{pp}}\times(\sum p_T^{\mathrm{hard}}(\Delta\phi)))}{dn^{\mathrm{dijet}}}\bigg|_{p_T^{\min}<p_T^{\mathrm{lead}}<p_T^{\max}}^{\mathrm{pp\times SF}}, \tag{A.1}
$$

where $\sum p_T^{\mathrm{asso}}(\Delta\phi)$ is sum of momentum of associate particles per bin in the momentum range of associate particle, n^{dijet} is number of di-jet in the range of momentum $p_T^{\min}<p_T^{\mathrm{lead}}<p_T^{\max}$. Eff is scaling constant of detector effects like the efficiency.$\sum p_T^{\mathrm{hard}}(\Delta\phi)$ is sum of momentum of associate particles come from hard scattering, $\sum p_T^{\mathrm{contami}}(\Delta\phi)$ is for the contaminations, $\sum p_T^{\mathrm{BKG^{soft}}}$ is for soft background particles, and $\sum p_T^{\mathrm{BKG^{hard}}}$ is for hard background particles. And Pb-Pb shows the distribution is for Pb-Pb events, and pp×SF shows the distribution is for pp events which is scaled to include background fluctuation effects in the distribution.

In this measurements, we embedded PYTHIA di-jet event to Pb-Pb events directly. Therefor estimated background come from soft and hard can be canceled. In the previous study[43] contamination ratio with respect to yield of the reconstructed charged particle are estimated. The ratio of contamination is depending on p_T, 6% at 0.3 GeV/c and about 2% at over than 1 GeV/c in Pb-Pb collisions. According to [43], the contamination is not much depending on

centrality. And the contamination in pp collisions has also similar tendency. In naive we can ignore the difference of contamination between pp collisions and Pb-Pb collisions.

Bibliography

[1] F. Halzen and A.D. Martin*et al*, Quarks and Leptons: An Introductory Course in Modern Particle Physics

[2] Michael Schmelling*et al*, Status of the Strong Coupling Constant, arXiv:hep-ex/9701002 (1997)

[3] V.N. Gribov, L.N. Lipatov*et al*, Deep inelastic electron scattering in perturbation theory, Sov.J.Nucl.Phys. 15:438 (1972)

[4] G. Altarelli and G. Parisi*et al*, Asymptotic Freedom in Parton Language Nucl.Phys. B126:298 (1977)

[5] Y.L. Dokshitzer*et al*, Calculation of the Structure Functions for Deep Inelastic Scattering and e$^+$ e$^-$ Annihilation by Perturbation Theory in Quantum Chromodynamics Sov.Phys. JETP 46:641 (1977)

[6] K. Yagi,T. Hatsuda and Y. Miake *et al*, Quark Gluon Plasma, Cambridge Monographs on Particle Physics, Nuclear Physics and Cosmology

[7] F. Karsch *et al*, Lattice QCD at non-zero chemical potential and the resonance gas model, arXiv:hep-lat/0401031v1 26 Jan 2004

[8] M.L. Miller, K. Reygers, S.J. Sanders, P. Steinberg*et al*, Glauber Modeling in High Energy Nuclear Collisions, arXiv:nucl-ex/0701025 (2007)

[9] L. McLerran *et al*, The Color Glass Condensate and Small x Physics: 4 Lectures., arXiv:hep-ph/0104285 (2001)

[10] N. Werner *et al*, Measurements of Proton Structure Functions, α_s and Parton Distribution Functions at HERA, hep-ex/0305109 (2003)

[11] I. Vitev *et al*, Leading order pQCD hadron production and nuclear modification factors atRHICandtheLHC.2002, hep-ph/0212109 (2002)

[12] I.P. Lokhtin, A.M. Snigirev *et al*, A model of jet quenching in ultrarelativistic heavy ion collisions and high-pt hadron spectra at RHIC hep-ph/0506189 (2005)

[13] I.P. Lokhtin, A.M. Snigirev *et al*, Angular structure of energy losses of hard jet in dense QCD-matter Phys. Lett. B 440 (1998)163

[14] M. Gyulassy, P. Levai, I. Vitev *et al*, Reaction operator approach to nonAbelian energy loss. Nucl. Phys. B594 (2001) 371

[15] R. Baier, Y. L. Dokshitzer, A.H. Mueller, D. Schiff *et al*, Angular dependence of the radiative gluon spectrum Phys. Rev. C 64, 057902 (2001)

[16] PHENIX Collaboration, Common Suppression Pattern of η and π^0 Mesons at High Transverse Momentum in Au+Au Collisions at $\sqrt{s_{NN}} = 200$ GeV, PhysRevLett.96.202301 (2006)

[17] STAR Collaboration, Evidence from d+Au measurements for final-state suppression of high p_T hadrons in Au+Au collisions at RHIC, PhysRevLett.91.072304 (2003)

[18] CMS Collaboration, Observation and studies of jet quenching in PbPb collisions at $\sqrt{s_{NN}} = 2.76$ TeV, Phys. Rev. C 84, 024906 (2011)

[19] CMS Collaboration, Nuclear modification factor of high transverse momentum jets in PbPb collisions at $\sqrt{s_{NN}} = 2.76$TeV, CMS PAS HIN-12-004

[20] ATLAS Collaboration, Observation of a Centrality-Dependent Dijet Asymmetry in Lead-Lead Collisions at $\sqrt{s} = 2.76$ TeVwith the ATLAS Detector at the LHC, Phys. Rev. Lett. 105.252303 (2010)

[21] O.S.Bruning, P.Collie, P.Lebrun, S.Myers, R.Ostojic, J.Poole, P.Proudlock *et al*, LHC Design Report, CERN-2004-003-V-1

[22] ALICE experiment, http://aliceinfo.cern.ch/

[23] ATLAS experiment, http://atlas.ch/

[24] CMS experiment, http://cms.web.cern.ch/

[25] LHCb experiment, http://lhcb.web.cern.ch/lhcb/

[26] L3 experiment, http://l3.web.cern.ch/l3/

[27] ALICE Collaboration, ALICE Technical Designe Report Forward Detectors: FMD, T0 and V0, CERN-LHCC-2004-025

[28] ALICE Collaboration, ALICE Technical Designe Report Zero Degree Calorimeter(ZDC), CERN-LHCC-99-5

[29] ALICE Collaboration, ALICE Technical Designe Report Inner Tracking System(ITS), CERN-LHCC 99-12

[30] ALICE Collaboration, ALICE Technical Design Report Time Projection Chamber(TPC), CERN-LHCC-2000-001

[31] ALICE Collaboration, ALICE Technical Design Report Transition Radiation Detector(TRD), CERN-LHCC-2001-021

[32] ALICE Collaboration, ALICE Technical Design Report Time of Flight System(TOF), CERN-LHCC-2002-016

[33] ALICE Collaboration, ALICE The Electromagnetic Calorimeter Addendum to the Technical Proposal, CERN-LHCC-2006-014

[34] ALICE Collaboration, ALICE Technical Design Report Photon Spectrometer (PHOS), CERN-LHCC-99-4

[35] ALICE Collaboration, ALICE Technical Design Report High Momentum Particle Identification Detector(HMPID), CERN-LHCC-98-19

[36] ALICE Collaboration, ALICE Technical Design Report Photon Multiplicity Detector (PMD), CERN-LHCC-99-32

[37] ALICE Collaboration, ALICE Technical Design Report Dimuon Forward Spectrometer, CERN-LHCC-99-22

[38] M.H. Seymour *et al*, Jet Shapes in Hadron Collisions: Higher Orders, Resummation and Hadronization, hep-ph/9707338 (1997)

[39] M. Cacciari, G. P. Salam and G. Soyez *et al*, The anti-k_T jet clustering algorithm, JHEP 0804 (2008) 063

[40] M. Cacciari, G. P. Salam and G. Soyez *et al*, FastJet user manual, CERN-PH-TH/2011-297

[41] CDF Collaboration, Charged jet evolution and the underlying event in proton-antiproton collisions at 1.8 TeV, Phys. Rev. D 65, 092002 (2002)

[42] CDF Collaboration, Measurement of charged-particle multiplicities in gluon and quark jets in pp collisions at $\sqrt{s}$ = 1.8 TeV. Phys. Rev. Lett. 94,171802 (2005)

[43] ALICE Collaboration, Suppression of Charged Particle Production at Large Transverse Momentum in Central Pb-Pb Collisions at $\sqrt{s_{NN}}$ =2.76 TeV arXiv:1012.1004 [nucl-ex] (2010)